

# Functional Nanomaterials for Energy Applications

Guest Editors: Rupesh S. Devan, Yuan-Ron Ma, Jin-Hyeok Kim,  
Raghu N. Bhattacharya, and Kartik C. Ghosh





---

# **Functional Nanomaterials for Energy Applications**

Journal of Nanomaterials

---

## **Functional Nanomaterials for Energy Applications**

Guest Editors: Rupesh S. Devan, Yuan-Ron Ma,  
Jin-Hyeok Kim, Raghu N. Bhattacharya, and Kartik C. Ghosh



---

Copyright © 2015 Hindawi Publishing Corporation. All rights reserved.

This is a special issue published in "Journal of Nanomaterials." All articles are open access articles distributed under the Creative Commons Attribution License, which permits unrestricted use, distribution, and reproduction in any medium, provided the original work is properly cited.

## Editorial Board

Katerina Aifantis, Greece  
Nageh K. Allam, USA  
Margarida Amaral, Portugal  
Xuedong Bai, China  
Enrico Bergamaschi, Italy  
Theodorian Borca-Tasciuc, USA  
C. Jeffrey Brinker, USA  
Christian Brosseau, France  
Xuebo Cao, China  
Sang-Hee Cho, Republic of Korea  
Shafiq Chowdhury, USA  
Cui ChunXiang, China  
Miguel A. Correa-Duarte, Spain  
Shadi A. Dayeh, USA  
Ali Eftekhari, USA  
Claude Estournes, France  
Alan Fuchs, USA  
Lian Gao, China  
Russell E. Gorga, USA  
Hongchen Chen Gu, China  
Mustafa O. Guler, Turkey  
John Zhanhu Guo, USA  
Smrati Gupta, Germany  
Michael Harris, USA  
Zhongkui Hong, USA  
Michael Z. Hu, USA  
David Hui, USA  
Y.-K. Jeong, Republic of Korea  
Sheng-Rui Jian, Taiwan  
Wanqin Jin, China  
Rakesh K. Joshi, India  
Zhenhui Kang, China

Fathallah Karimzadeh, Iran  
Do Kyung Kim, Republic of Korea  
Kin Tak Lau, Australia  
Burtrand Lee, USA  
Benxia Li, China  
Jun Li, Singapore  
Shijun Liao, China  
Gong Ru Lin, Taiwan  
J.-Y. Liu, USA  
Jun Liu, USA  
Tianxi Liu, China  
Songwei Lu, USA  
Daniel Lu, China  
Jue Lu, USA  
Ed Ma, USA  
Gaurav Mago, USA  
Sanjay R. Mathur, Germany  
Nobuhiro Matsushita, Japan  
A. McCormick, USA  
Vikas Mittal, UAE  
Weihai Ni, Germany  
Sherine Obare, USA  
Edward Andrew Payzant, USA  
Kui-Qing Peng, China  
Anukorn Phuruangrat, Thailand  
Ugur Serincan, Turkey  
Huaiyu Shao, Japan  
Donglu Shi, USA  
Suprakas Sinha Ray, South Africa  
Vladimir Sivakov, Germany  
Marinella Striccoli, Italy  
Bohua Sun, South Africa

Saikat Talapatra, USA  
Nairong Tao, China  
Titipun Thongtem, Thailand  
Somchai Thongtem, Thailand  
Valeri P. Tolstoy, Russia  
Tsung-Yen Tsai, Taiwan  
Takuya Tsuzuki, Australia  
Raquel Verdejo, Spain  
Mat U. Wahit, Malaysia  
Shiren Wang, USA  
Yong Wang, USA  
Cheng Wang, China  
Zhenbo Wang, China  
Jinquan Wei, China  
Ching Ping Wong, USA  
Xingcai Wu, China  
Guodong Xia, Hong Kong  
Zhi Li Xiao, USA  
Ping Xiao, UK  
Shuangxi Xing, China  
Yangchuan Xing, USA  
N. Xu, China  
Doron Yadlovker, Israel  
Ying-Kui Yang, China  
Khaled Youssef, USA  
Kui Yu, Canada  
Haibo Zeng, China  
Tianyou Zhai, Japan  
Renyun Zhang, Sweden  
Yanbao Zhao, China  
Lianxi Zheng, Singapore  
Chunyi Zhi, Japan

## Contents

**Functional Nanomaterials for Energy Applications**, Rupesh S. Devan, Yuan-Ron Ma, Jin-Hyeok Kim, Raghu N. Bhattacharya, and Kartik C. Ghosh  
Volume 2015, Article ID 131965, 2 pages

**Comparative Studies on Thermal Performance of Conic Cut Twist Tape Inserts with SiO<sub>2</sub> and TiO<sub>2</sub> Nanofluids**, Sami D. Salman, Abdul Amir H. Kadhum, Mohd S. Takriff, and Abu Bakar Mohamad  
Volume 2015, Article ID 921394, 14 pages

**A Review on the Fabrication of Electrospun Polymer Electrolyte Membrane for Direct Methanol Fuel Cell**, Hazlina Junoh, Juhana Jaafar, Muhammad Noorul Anam Mohd Norddin, Ahmad Fauzi Ismail, Mohd Hafiz Dzarfan Othman, Mukhlis A. Rahman, Norhaniza Yusof, Wan Norhayati Wan Salleh, and Hamid Ilbeygi  
Volume 2015, Article ID 690965, 16 pages

**Effects of Different Doping Ratio of Cu Doped CdS on QDSCs Performance**, Xiaojun Zhu, Xiaoping Zou, and Hongquan Zhou  
Volume 2015, Article ID 498950, 4 pages

**Characterization of Carbon Nanotube/Graphene on Carbon Cloth as an Electrode for Air-Cathode Microbial Fuel Cells**, Hung-Yin Tsai, Wei-Hsuan Hsu, and Ying-Chen Huang  
Volume 2015, Article ID 686891, 7 pages

**Effects of Niobium-Loading on Sulfur Dioxide Gas-Sensing Characteristics of Hydrothermally Prepared Tungsten Oxide Thick Film**, Viruntachar Kruefu, Anurat Wisitsoraat, and Sukon Phanichphant  
Volume 2015, Article ID 820509, 8 pages

## Editorial

# Functional Nanomaterials for Energy Applications

**Rupesh S. Devan,<sup>1</sup> Yuan-Ron Ma,<sup>2</sup> Jin-Hyeok Kim,<sup>3</sup>  
Raghu N. Bhattacharya,<sup>4</sup> and Kartik C. Ghosh<sup>5</sup>**

<sup>1</sup>Department of Physics, University of Pune, Pune 411007, India

<sup>2</sup>Department of Physics, National Dong Hwa University, Hualien 97401, Taiwan

<sup>3</sup>Department of Materials Science and Engineering, Chonnam National University, Gwangju 500-757, Republic of Korea

<sup>4</sup>National Renewable Energy Laboratory, Golden, CO 80401, USA

<sup>5</sup>Department of Physics, Astronomy and Materials Science Missouri State University, Springfield, MO 65897, USA

Correspondence should be addressed to Rupesh S. Devan; devan\_rs@yahoo.co.in and Yuan-Ron Ma; ronma@mail.ndhu.edu.tw

Received 16 February 2015; Accepted 16 February 2015

Copyright © 2015 Rupesh S. Devan et al. This is an open access article distributed under the Creative Commons Attribution License, which permits unrestricted use, distribution, and reproduction in any medium, provided the original work is properly cited.

To leap forward from the energy crisis issues and improve lifestyle, we all are looking positively toward nanomaterials or nanostructures. Therefore, the exploration of new features of both typical and novel materials at the nanoscale level is playing important role in the development of innovative and improved energy technologies that have the capability of conserve/convert energy at large extend. By tailoring the surface morphology of materials in its nanoforms, the functional properties can be significantly adapted and specifically combined to produce highly potent multifunctional materials for conversion, storage, and consumption of energy in various forms. The papers selected for this special issue represent a good panel for addressing various energy applications including solar cell, fuel cells, nanofluid twistors, and gas sensors. Of course, the selected topic and the papers are not an exhaustive representation of the utilization of functional nanomaterials for energy applications. Nonetheless, they represent the rich and many-facet knowledge, which we have the pleasure of sharing with the readers.

The special issue contains five papers, where brief review on the fabrication of electrospun polymer electrolyte membrane for direct methanol fuel cell is presented. One of the papers brings up the method to utilize carbon nanotube (CNT) and graphene modified carbon-cloth electrode for fabrication of membrane free air-cathode microbial fuel cells (MFC). Another paper accounted the QDSCs performance of CdS with various doping concentration of Cu. Two other papers reported the sulfur dioxide sensing ability of tungsten oxide after niobium loading and one paper mentioned

thermal performance of conic cut twist tape inserts with SiO<sub>2</sub> and TiO<sub>2</sub> nanofluids.

A review article, titled “A Review on the Fabrication of Electrospun Polymer Electrolyte Membrane for Direct Methanol Fuel Cell,” authored by H. Junoh et al., reported the development of electrospun polymer electrolyte membrane for direct methanol fuel cell (DMFC). They reported the details and benefits of electrospun technology. This electrospun technique is capable of sustaining proton conductivity and also suppresses methanol permeability without jeopardizing the fuel cell system. This review paper described in detail the electrospun-sulfonated poly(ether ether ketone) (SPEEK) for fuel cell application, as well as optimizing the degree of sulfonation for spinnable SPEEK solution.

The paper, titled “Characterization of Carbon Nanotube/Graphene on Carbon Cloth as an Electrode for Air-Cathode Microbial Fuel Cells,” authored by H.-Y. Tsai et al., investigated the performance of a single-chamber microbial fuel cell (MFC) that uses carbon nanotube (CNT) and graphene-modified carbon-cloth electrodes. They developed a process for fabricating carbon-based modified electrodes and *Escherichia coli* HB101 in an air-cathode MFC. They, finally, found that the power density of MFCs is to be improved by applying a coat of either graphene or CNT to a carbon-cloth electrode, and the graphene-modified electrode exhibits superior performance.

The paper, titled “Effects of Different Doping Ratio of Cu Doped CdS on QDSCs Performance,” authored by X. Zhu et al., investigated the effects of Cu doping concentration on

the performance of CdS quantum dot sensitized solar cell prepared by successive ionic layer adsorption and reaction (SILAR) method. Their experimental results showed Cu doped CdS quantum dot sensitized solar cells (QDSCs) have higher open circuit voltage, short circuit current density, and photoelectric conversion efficiency than undoped CdS QDSCs. They also found that, in a certain range, the lower the doping ratio of Cu, the better the performance of QDSCs.

The paper, titled "Effects of Niobium-Loading on Sulfur Dioxide Gas-Sensing Characteristics of Hydrothermally Prepared Tungsten Oxide Thick Film," authored by V. Kruefu et al., reported the hydrothermal synthesis of  $\text{WO}_3$  rods which were further loaded with Nb nanoparticles with various weight percent. The loading of Nb nanoparticles along the surface of  $\text{WO}_3$  rods improved sulfur dioxide sensing performance. They reported Nb nanoparticle loading is an effective mean to improve the sensing ability of  $\text{WO}_3$  nanostructures.

The paper, titled "Comparative Studies on Thermal Performance of Conic Cut Twist Tape Inserts with  $\text{SiO}_2$  and  $\text{TiO}_2$  Nanofluids," written by S. D. Salman et al., compared performance of various conic cut twist tapes inserted in  $\text{SiO}_2$  and  $\text{TiO}_2$  nanofluids and found enhancement in heat transfer rate by increasing concentration of nanoparticles in nanofluid. Finally they implemented empirical correlations for their experimental inventions.

## Acknowledgments

We would like to thank the authors for their excellent contributions and patience in assisting us. Finally, the fundamental work of all the reviewers of these papers is also very warmly acknowledged.

*Rupesh S. Devan  
Yuan-Ron Ma  
Jin-Hyeok Kim  
Raghu N. Bhattacharya  
Kartik C. Ghosh*

## Research Article

# Comparative Studies on Thermal Performance of Conic Cut Twist Tape Inserts with SiO<sub>2</sub> and TiO<sub>2</sub> Nanofluids

Sami D. Salman,<sup>1,2</sup> Abdul Amir H. Kadhum,<sup>1</sup> Mohd S. Takriff,<sup>1</sup> and Abu Bakar Mohamad<sup>1</sup>

<sup>1</sup>Department of Chemical and Process Engineering, Faculty of Engineering and Built Environment, Universiti Kebangsaan Malaysia, 43600 Bangi, Selangor, Malaysia

<sup>2</sup>Biochemical Engineering Department, Al-khwarizmi College of Engineering, University of Baghdad, Baghdad 47024, Iraq

Correspondence should be addressed to Sami D. Salman; sami.albayati@gmail.com

Received 20 August 2014; Revised 21 October 2014; Accepted 28 October 2014

Academic Editor: Rupesh S. Devan

Copyright © 2015 Sami D. Salman et al. This is an open access article distributed under the Creative Commons Attribution License, which permits unrestricted use, distribution, and reproduction in any medium, provided the original work is properly cited.

This paper presents a comparison study on thermal performance conic cut twist tape inserts in laminar flow of nanofluids through a constant heat flux tube. Three tape configurations, namely, quadrant cut twisted tape (QCT), parabolic half cut twisted tape (PCT), and triangular cut twisted (VCT) of twist ratio  $\gamma = 2.93$  and cut depth  $d_c = 0.5$  cm were used with 1% and 2% volume concentration of SiO<sub>2</sub>/water and TiO<sub>2</sub>/water nanofluids. Typical twist tape with twist ratio of  $\gamma = 2.93$  was used for comparison. The results show that the heat transfer was enhanced by increasing of Reynolds number and nanoparticles concentration of nanofluid. The results have also revealed that the use of twist tape enhanced the heat transfer coefficient significantly and maximum heat transfer enhancement was achieved by the presence of triangular cut twist tape insert with 2% volume concentration of SiO<sub>2</sub> nanofluid. Over the range investigated, the maximum thermal performance factor of 5.13 is found with the simultaneous use of the SiO<sub>2</sub> nanofluid at 2% volume concentration VCT at Reynolds number of 220. Furthermore, new empirical correlations for Nusselt number, friction factor, and thermal performance factor are developed and reported.

## 1. Introduction

Heat transfer enhancement technique plays substantial role for laminar flow regime, due to the deficiency of heat transfer coefficient in plain tubes. Heat transfer augmentation techniques can be classified as active and passive techniques [1, 2]. Active techniques require external power source, such as electric field, surface vibration, or Jet impingement. Whereas, passive techniques require fluid additives, surface modifications, or swirl/vortex flow devices to enhance heat transfer. The swirl flow devices include coil wire, helical wire coil, and twist tape inserts. So, many published articles related to experimental and numerical investigation on convective heat transfer using twisted tape inserts and water as test fluid have been reported in the literature [3–13]. The limitation of thermophysical properties and low thermal conductivity of water led to innovative new fluid which can enhance the heat transfer. Small amount of nanoparticles was dispersed into base fluid to improve its thermal conductivity.

The resultant fluid of suspended nanoparticles into base fluid was called nanofluid. Nanofluids were first used by Choi and Eastman [14] in 1995 at Argonne National Laboratory, USA. Subsequently, several types of nanoparticles have been employed for nanofluid preparation, including metals such as gold (Au), copper (Cu), and silver (Ag) and also metal oxides such as TiO<sub>2</sub>, Fe<sub>3</sub>O<sub>4</sub>, Al<sub>2</sub>O<sub>3</sub>, and CuO [15–21]. Due to their significantly lower cost, metal oxides are preferred for heat transfer enhancement application compared to metals. The combination between twisted tape inserts with nanofluids was simultaneously utilized to produce heat transfer enhancement greater than either techniques operating individually. Pathipakka and Sivashanmugam [22] proposed CFD simulation for laminar heat transfer characteristics using Al<sub>2</sub>O<sub>3</sub>/water nanofluids in a uniform heat flux tube equipped with helical twist tape inserts. Twist tape of twist ratios 2.93, 3.91, and 4.89 with three different volume concentrations of 0.5%, 1%, and 1.5% Al<sub>2</sub>O<sub>3</sub>/water was simultaneously used for simulation. The maximum heat

transfer enhancement of 31.29% was obtained with the use of helical insert of twist ratio 2.93 together with nanofluid with volume concentration of 1.5% at Reynolds number of 2039. Wongcharee and Eiamsa-ard [23] have investigated heat transfer, friction, and thermal performance characteristics of CuO/water nanofluids in a circular tube fitted with alternate axis and the typical twisted tapes experimentally. Three different volume concentrations of 0.3%, 0.5%, and 0.7% CuO/water with twisted tapes at constant twist ratio  $y/w = 3$  were used for investigation. Their results revealed that maximum thermal performance factor of 5.53 was obtained at Reynolds number of 1990 with the simultaneous use of 0.7% CuO/water nanofluid with alternate axis twisted tape. Suresh et al. [24] have performed a comparative study on the thermal performance of helical screw tape inserts with 0.1% volume concentration  $\text{Al}_2\text{O}_3$ /water and CuO/water nanofluids in laminar flow through a straight circular duct under constant heat flux boundary condition. The helical screw tape inserts with twist ratios  $y = 1.78, 2.44, \text{ and } 3$  were used for investigation. The experimental results show that the helical screw tape inserts offered better thermal performance factor when used with CuO/water nanofluid than with  $\text{Al}_2\text{O}_3$ /water nanofluid. Salman et al. [25] reported numerical study on heat transfer enhancement of CuO/water nanofluid in a constant heat flux tube fitted with classical and one side parabolic-cut twist tape inserts using FLUENT version 6.3.26. Twisted tapes of different twist ratios ( $y = 2.93, 3.91, \text{ and } 4.89$ ) and different cut depths ( $w = 0.5, 1, \text{ and } 1.5 \text{ cm}$ ) were simultaneously used with 2% and 4% volume concentration CuO nanofluid for simulation. Their results elaborated that the parabolic cut twist tape of twist ratio  $y = 2.93$  and cut depth  $w = 0.5$  with 4% CuO nanofluid offers about 10% enhancement for the Nusselt number than that of classical twisted tape at the same conditions. Salman et al. [26] reported an application of a mathematical model of the heat transfer enhancement and friction factor characteristics of water in constant heat-flux tube fitted with one side elliptical cut twisted tape inserts with twist ratios ( $y = 2.93, 3.91, \text{ and } 4.89$ ) and different cut depths ( $w = 0.4, 0.8, \text{ and } 1.4 \text{ cm}$ ) under laminar flow using FLUENT version 6.3.26. The results elaborated that the enhancement of heat transfer rate and the friction factor induced by elliptical cut twisted tape inserts increases with the Reynolds number and decreases with twist ratio. In addition, the results show that the elliptical cut twisted tape with twist ratio  $y = 2.93$  and cut depth  $w = 0.5 \text{ cm}$  offered higher heat transfer rate with significant increases in friction factor. Salman et al. [27] also studied heat transfer of water in a uniformly heated circular tube fitted with one side quadrant cut twisted tape inserts in laminar flow using FLUENT version 6.3.26. Classical and quadrant cut twisted tape with twist ratio ( $y = 2.93, 3.91, \text{ and } 4.89$ ) and different cut depths ( $w = 0.5, 1, \text{ and } 1.5 \text{ cm}$ ) were employed for the simulation. The results show that the quadrant cut twisted tape with twist ratio ( $y = 2.93$ ) and cut depth ( $w = 0.5 \text{ cm}$ ) presents a maximum heat transfer rate with significant increases in friction factor. The attractive characteristics of triangular, elliptic, and quadrant cut twist tape with twist ratio  $y = 2.93$ , mentioned above, have motivated the present research to combine the effects

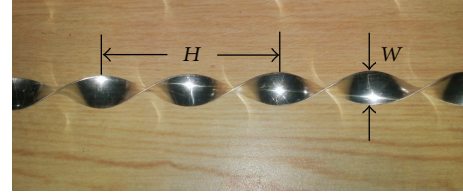


FIGURE 1: Typical twisted tape (TT).

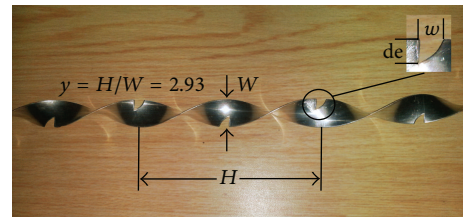


FIGURE 2: Quadrant cut twisted tape (QCT).

of a novel tube insert with the laminar flow of nanofluids. For the present study, an experimental comparison study on the thermal performance of alternative conic cut twist tape inserts with  $\text{SiO}_2$ /water and  $\text{TiO}_2$ /water nanofluids in uniform heat flux tube was implemented. The tests using nanofluid with and without typical twisted tape were also conducted, for comparison.

## 2. Technical Details of Twisted Tape Inserts

The geometrical configuration of typical and conic-cut twist tape inserts is shown in Figures 1, 2, 3, and 4. Aluminium strips of 0.8 mm thickness, 24.5 mm width, and 1800 mm length are uniformly winding over a specified distance of 75 mm to produce the desired twist ratio ( $y = 2.93$ ). The twist ratio “ $y$ ” was defined as the ratio of the length of one full twist ( $360^\circ$ ) to the tape width. The conic cut shapes are drawn for the specified distance on the strips before twisting. Thereafter, cuts are made on twisted tape based on these cut shapes to obtain the desired configurations.

## 3. Nanofluid Properties

The silica and titanium oxide nanoparticles delivered from US Research Nanomaterials Inc. with properties illustrated in Table 1 were used for nanofluids preparation of the nanofluid. The particle size and chemical composition of nanoparticles were checked before nanofluid samples preparation. Field Emission Scanning Electron Microscopy (FESEM) was used for particle size, shape, and agglomeration visualization. The FESEM results show that the nanoparticles are in approximately spherical shape with diameter around 20 nm. Energy-dispersive X-ray spectroscopy (EDX) was used for elemental analysis or chemical characterization. The EDX spectrum of nanoparticles is shown in Figures 5 and 6. Nanofluids with desired volume concentrations of 1% and 2% were prepared by dispersing specified amounts of  $\text{SiO}_2$  and  $\text{TiO}_2$  nanoparticles in deionised water. The samples were agitated

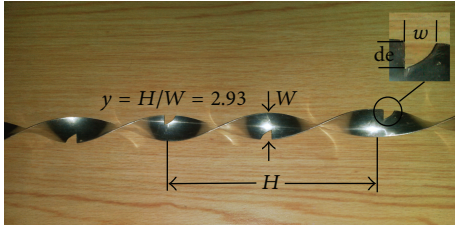


FIGURE 3: Parabolic half cut twisted tape (PCT).

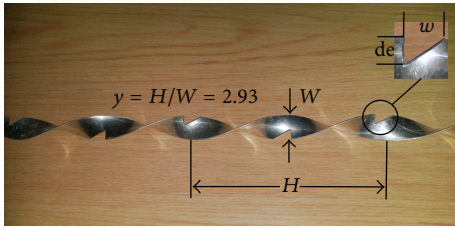


FIGURE 4: Triangular cut twist tape (VCT).

TABLE 1: Properties of nanoparticles at 20°C.

Material	Density (gm/cm <sup>3</sup> )	Specific heat (MJ/m <sup>3</sup> K)	Thermal conductivity (W/m K)	Particle size (nm)
SiO <sub>2</sub>	2.2	745	1.4	15–20
TiO <sub>2</sub>	3.9	650	11.2	15–20

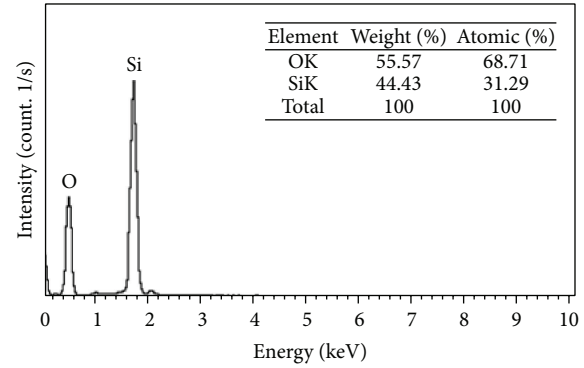
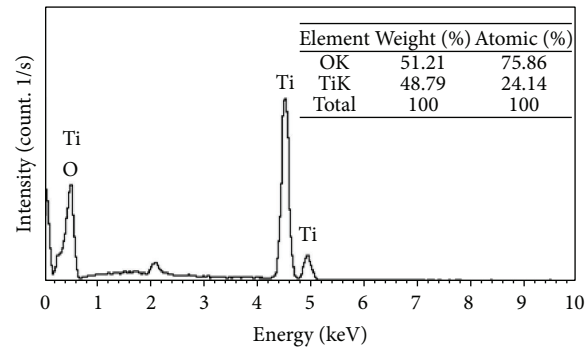
TABLE 2: Thermophysical properties of water and nanofluids at 25°C.

Fluid	Density $\rho$ (gm/cm <sup>3</sup> )	Viscosity $\mu$ (Ns/m <sup>2</sup> )	Specific heat (MJ/m <sup>3</sup> ·K)	Thermal conductivity (W/m·K)
Water	0.9969	0.000963	4.1672	0.6096
Water + 1% SiO <sub>2</sub>	1.0090	0.001068	4.1412	0.6275
Water + 2% SiO <sub>2</sub>	1.0211	0.001197	4.1141	0.6288
Water + 1% TiO <sub>2</sub>	1.0260	0.001073	4.1483	0.6455
Water + 2% TiO <sub>2</sub>	1.0550	0.001188	4.1415	0.6672

for 1 hr and finally transferred to Ultrasonic bath (NEY-280H) for 1 hour in order to break up any potential clusters of nanoparticles and to achieve the required homogeneous suspensions. The thermophysical properties of nanofluids for desired volume concentration  $\phi$  were measured 25°C using portable density meter (Type DA-130N), POLYVISC rotational viscometer, and Hot Disk Transient Plane Source TPS 2500S. Properties of the water and nanofluids are shown in Table 2.

#### 4. Experimental Setup

The experimental set-up as shown in Figure 7 consists of a test section, calming section, chilled water tank with cooling unit, circulation pump, and pipe line system. Both the calming section and test sections are made of straight stainless steel tube

FIGURE 5: EDX spectrum of SiO<sub>2</sub> nanoparticles.FIGURE 6: EDX spectrum of TiO<sub>2</sub> nanoparticles.

with the dimensions 2000 and 1800 mm long, respectively, with 25.4 mm ID and 33.33 mm OD. The calming section is used to eliminate the entrance effect. The outside surface of the test section is brazed with fifteen thermowells made of stainless steel with dimensions of 6.36 mm ID, 1 mm thick, and 120 mm length which are mounted on the test section at axial positions as shown in Figure 8. The test section tube is wound with ceramic beads coated electrical SWG Nichrome heating wire of resistance 18  $\Omega$ . Over the electrical winding, two layers of asbestos rope and glass wool insulations are used to minimize heat loss. The terminals of the Nichrome wire are attached to the Volteq 3 KVA variac variable transformer with input single phase 220 V AC, 50 Hz and output voltage can be adjusted from 0 to 150 V AC. The amount of heat required in test section can be achieved by varying the output voltage. Fifteen calibrated RTD PT 100 type temperature sensors with 0.75% accuracy are placed in the thermowells to measure the outside wall temperatures. Two RTD PT 100 type temperature sensors are inserted near the centre of pipe to measure the bulk temperature of fluid at inlet and outlet of test section. The pressure drop across the test section is measured using DMP3051 digital on-line differential pressure transmitter and the velocity of water and nanofluids is measured by portable TDS-100H ultrasonic flowmeter. The hot fluid after passing through the heated test section flows through chilled water for cooling and the desired temperature is controlled by temperature controller. 30 m head centrifugal pump with bypass valves is used to regulate the flow rate through the

TABLE 3: Technical details of experimental setup and test conditions.

Setup and conditions	Description
(A) Experimental setup	
(a) Inner tube inner diameter ( $d_i$ )	25.40 mm
(b) Outer tube inner diameter ( $d_o$ )	33.35 mm
(c) Test tube length	1800 mm
(d) Material of inner tube	Stainless steel 304L
(f) Insulation material	Asbestos rope and glass wool
(g) Temperature measurements	RTD Pt 100 type ( $\pm 0.75\%$ accuracy)
(h) Flow measurements	TDS-100H ultrasonic flowmeter ( $\pm 0.1\%$ accuracy)
(i) Pressure measurement	DMP3051 differential pressure transmitter ( $\pm 0.2\%$ accuracy)
(k) Heater capacity	3 KW
(B) Typical twisted tape (TT)	
(a) Material	Aluminium
(b) Tape width ( $W$ )	24.5 mm
(c) Tape thickness	0.8 mm
(d) Tape pitch length ( $H$ , $360^\circ$ )	75 mm
(e) Twist ratio ( $y = H/d_i$ )	2.93
(C) Conic cut twisted tape	
(a) Material	Aluminium
(b) Tape width ( $W$ )	24.5 mm
(c) Tape thickness	0.8 mm
(d) Tape pitch length ( $H$ , $360^\circ$ )	75 mm
(e) Twist ratio ( $y = H/d_i$ )	2.93
(f) Quadrant cut twist tape (QCT)	$w = 5$ mm, $d_e = 5$ mm
(g) Parabolic cut twist tape (PCT)	$w = 5.89$ mm, $d_e = 5$ mm
(h) Triangular cut twist tape (VCT)	$w = 7.85$ mm, $d_e = 5$ mm
(D) Test conditions	
(a) Reynolds number, (Re)	200 to 1500
(b) Type of flow in inner tube	Laminar

test section. The details of experimental setup and operating conditions are summarized in Table 3.

## 5. Data Reduction

The measured data were used to calculate the Nusselt number, friction factor, and thermal performance factor in the laminar flow regime for Reynolds number ranging from 200 to 1500.

The heat transfer rate obtained from the hot fluid in the test section tubes can be expressed as

$$Q_{\text{conv}} = mc_p (T_{\text{out}} - T_{\text{in}}). \quad (1)$$

The heat transfer rate in terms of mean convective heat transfer coefficient ( $h$ ) can be expressed as

$$Q_{\text{conv}} = hA (\bar{T}_s - T_b). \quad (2)$$

The heat flux becomes

$$q_s'' = \frac{Q_{\text{conv}}}{A} = h (\bar{T}_s - T_b), \quad (3)$$

where  $T_b$  is a mean bulk flow temperature  $T_b = (T_{\text{out}} + T_{\text{in}})/2$ .

Then, mean inner wall surface temperature ( $\bar{T}_s$ ) of the test section is calculated from 15 stations of surface temperatures located between the inlet and the outlet of the test section, using the following equation:

$$\bar{T}_s = \sum \frac{T_{si}(x)}{15}, \quad (4)$$

where  $T_{si}(x)$  is a local inner wall temperature which can be calculated from steady one dimensional heat conduction equation in cylindrical coordinate [28]

$$\frac{1}{r} \frac{d}{dr} \left( kr \frac{dT}{dr} \right) = 0. \quad (5)$$

The solution of this equation with constant heat flux boundary condition at the wall becomes

$$T_{si}(x) = T_{so}(x) - \frac{Q_{\text{conv}} \ln(D_o/D_i)}{2\pi kL}, \quad (6)$$

where  $T_{so}(x)$  represent the local outer wall temperatures, measured by RTD PT 100 type temperature sensors,  $D_o$ ,  $D_i$  are the outer and inner tube diameters,  $k$  is the thermal conductivity of the test section wall, and  $L$  is the length of the test section.

The average Nusselt number (Nu) can be estimated from the following equation:

$$\text{Nu} = \frac{h_{\text{avg}} D_i}{k_f}. \quad (7)$$

The average heat transfer coefficient can be determined from (7):

$$h_{\text{avg}} = \frac{q_s''}{(\bar{T}_s - T_b)}. \quad (8)$$

The pressure drop ( $\Delta p$ ) measured across the test section was used to calculate friction factor ( $f$ ) using the following equation:

$$f_D = \frac{2\Delta p D_i}{L \rho u^2}. \quad (9)$$

The performance evaluation analysis for laminar flow at the same pumping power is given by the following correlation proposed by Usui et al. [29]:

$$\eta = \frac{(\text{Nu}/\text{Nu}_o)}{(f/f_o)^{0.1666}}, \quad (10)$$

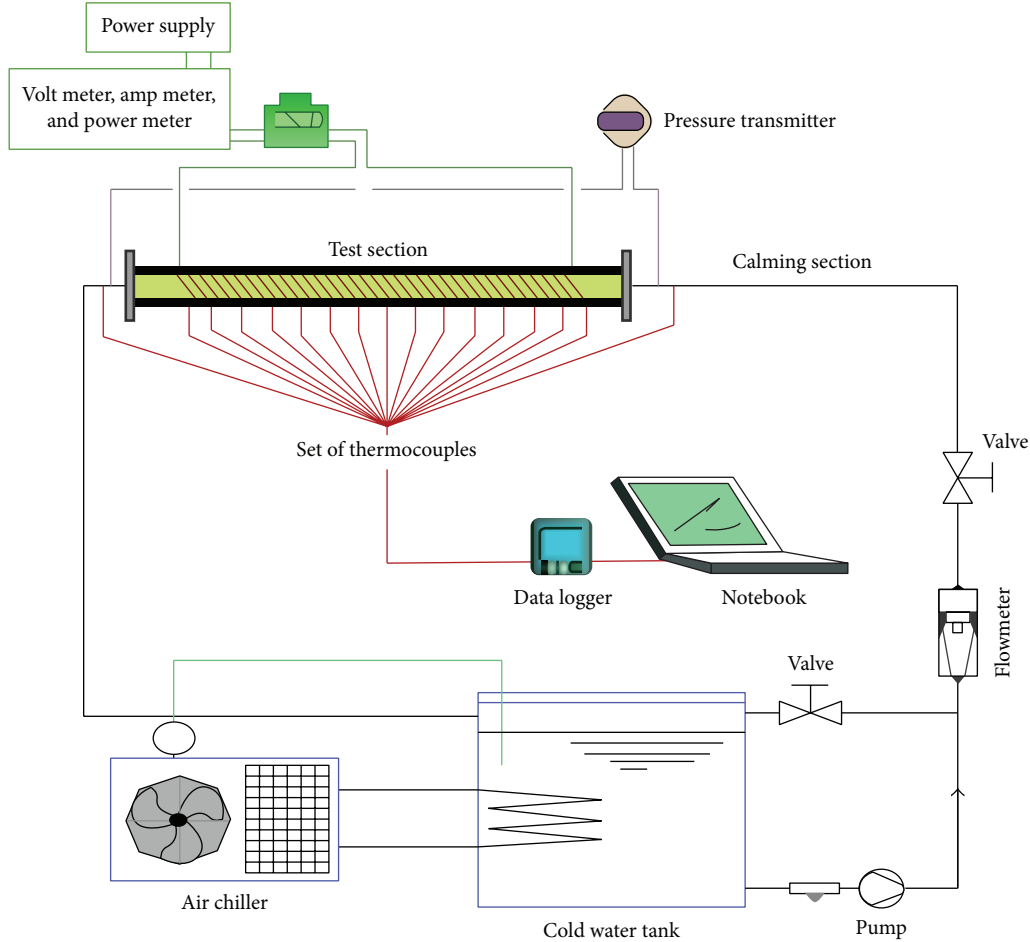


FIGURE 7: Schematic diagram of the experimental setup.



FIGURE 8: Test section with thermocouple locations.

where  $Nu$  and  $f$  are, respectively, the Nusselt number and friction factor of the tube with enhancing factor (nanofluid and/or twisted tape) while  $Nu_o$  and  $f_o$  are, respectively, the Nusselt number and friction factor of the plain tube.

A standard uncertainty analysis was conducted for each measurement using Kline-McClintock method [30]. The maximum uncertainties for Reynolds number, Nusselt number, and friction factor were calculated to be 6.1%, 8.48%, and 2.4%, respectively.

## 6. Results and Discussions

**6.1. Experimental Setup Validation.** To evaluate the reliability of the present experimental setup, the experimental results

of pure water in plain tube without twisted tape under laminar flow conditions were validated with Shah equation [31] and Hagen-Poiseuille equation [28]. The results showed reasonable agreement with the local Nusselt number ( $Nu_x$ ) and friction factor ( $f$ ) as shown in Figures 9 and 10:

$$Nu_x = 1.953x_*^{-1/3} \quad \text{for } x_* \leq 0.03, \quad (11)$$

$$Nu_x = 4.364 + \frac{0.0722}{x_*} \quad \text{for } x_* > 0.03,$$

$$f = \frac{64}{Re}. \quad (12)$$

The results of Nusselt number for plain tube with typical twisted tape ( $\gamma = 2.93$ ) were also validated with Manglik and Bergle equation [3]. As shown in Figure 11, the data obtained were found to be in good agreement with the available correlation. For the proof of the present typical twisted tape, Nusselt number of a tube fitted with the present typical twisted tapes was compared with experimental data of right-left helical twist tape [32] as shown in Figures 12 and 13. Apparently, the typical twist tape offered an additional heat transfer enhancement with less skin friction factor.

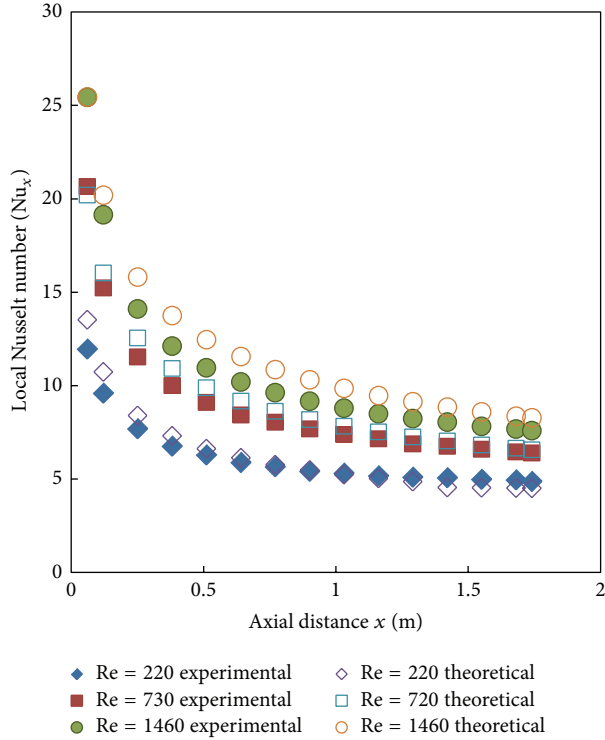


FIGURE 9: Comparison between measured and calculated local Nusselt number ( $Nu_x$ ) using DI-Water.

**6.2. Effect of Nanoparticle Volume Concentration in Plain Tube.** Experiments were performed to study heat transfer enhancements in plain tube with laminar flow of deionized water and  $SiO_2$  and  $TiO_2$  nanofluids of 1% and 2% volume concentration. The obtained results of Nusselt number and friction factor are elaborated in Figures 14 and 15. From Figure 14, it can be seen that the Nusselt number increased with the increase of nanoparticle concentration and Reynolds number. This means that the presence of nanoparticles increases the energy exchange rates in the fluid with penalty on the wall shear stress due to Brownian motion [33]; the increases of Reynolds number increase random movements of the fluid and consequently enhance the thermal dispersion of the flow. Evidently,  $SiO_2$  nanofluid with 2% volume concentration offered highest Nusselt number, followed by  $TiO_2$  and water, respectively. On other hand, Figure 15 shows slightly augmentation in friction factor value with increases of nanoparticles concentration. This means that the presence of nanoparticles volume fraction increases nanofluid viscosity with wall shear stress. The experimental results were used to derive the following correlations of Nusselt number and friction for water ( $\phi = 0$ ),  $SiO_2$  and  $TiO_2$  nanofluids ( $\phi \leq 2\%$ ). The predicted values of these correlations show reasonable agreement with the experimental results as shown in Figures 16 and 17.

For  $SiO_2$  nanofluid,

$$Nu = 0.6116Pr^{0.4}Re^{0.2795}(1 + \phi)^{3.47}, \quad (13)$$

$$f = 63.236Re^{-0.994}(1 + \phi). \quad (14)$$

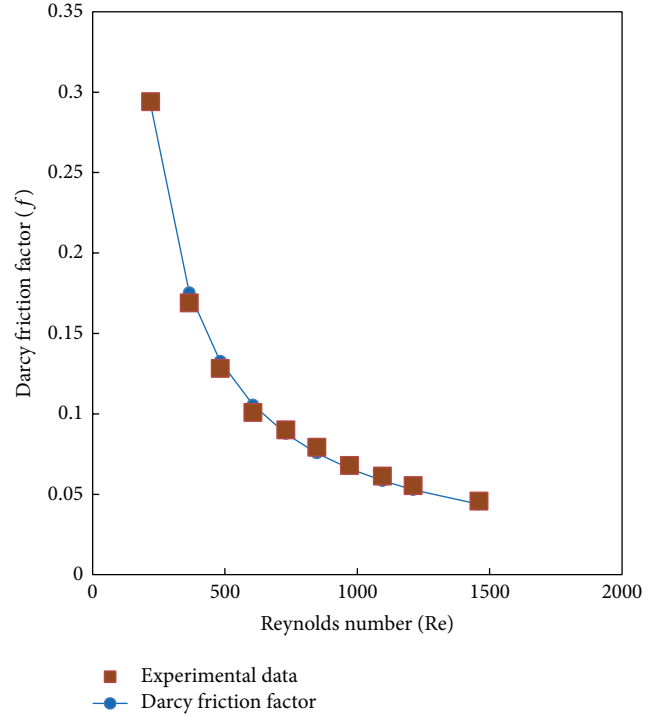


FIGURE 10: Friction factor across the test section using DI-water as the working fluid.

For  $TiO_2$  nanofluid,

$$Nu = 0.6116Pr^{0.4}Re^{0.2795}(1 + \phi)^{1.47}, \quad (15)$$

$$f = 63.236Re^{-0.994}(1 + \phi). \quad (16)$$

**6.3. Effect of Nanoparticle Volume Concentration with Twist Tape.** Variations of Nusselt number and friction factor versus Reynolds number for laminar flow of deionized water,  $SiO_2$  and  $TiO_2$  nanofluids of 1% and 2% volume concentration in tube fitted with typical twist tape ( $\gamma = 2.93$ ) are shown in Figures 18 and 19. Evidently, Figure 18 shows that the combined use of nanofluid with twist tape produces further augment in heat transfer coefficient than either nanofluid or twist tape individually. The simultaneous use of nanofluid with twist tape increases the thermal conductivity and viscosity of working fluid as well as increasing swirl flow path. Thus, greater fluid mixing and higher heat transfer coefficient are produced. Eventually,  $SiO_2$  nanofluid with 2% volume concentration with typical twist tape offered a higher Nusselt number compared with the others. As shown in Figure 19, the friction factor decreases with the increase of Reynolds number for water and different volume fractions of nanoparticles. Based on the experimental results, the following correlations of Nusselt number and friction factor were derived. The correlations are valid for laminar flow ( $Re < 1500$ ),  $\phi \leq 2\%$  volume concentration ( $\phi = 0$  for water) of  $SiO_2$  and  $TiO_2$  nanofluid, and typical twist tape of twist ratio  $\gamma = 2.93$ . The predicted data were in good agreement

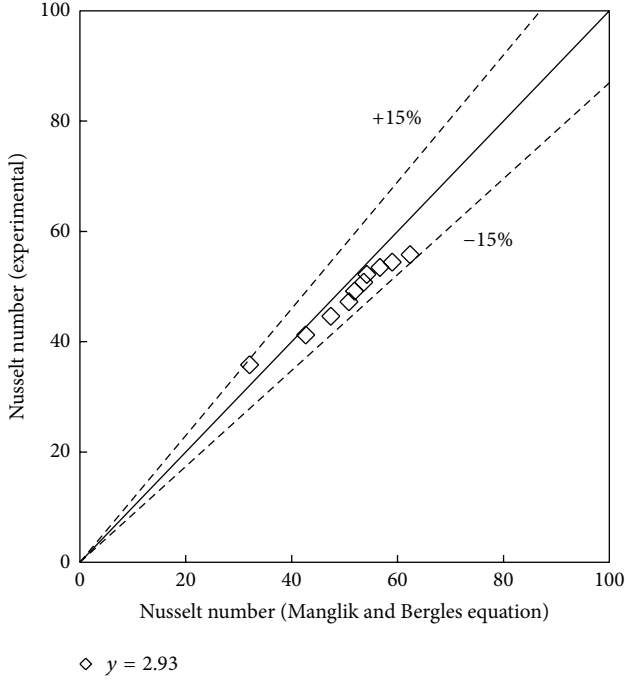


FIGURE 11: Comparison of experimental and predicted Nusselt number of the plain tube fitted with typical twisted tape.

with the experimental data within  $\pm 6\%$  for Nusselt number and  $\pm 8\%$  friction factor as shown in Figures 20 and 21:

$$Nu = 5.236Pr^{0.4}Re^{0.2357}y^{-0.0881}(1 + \phi)^{0.124} \quad (17)$$

$$f = 76.789Re^{-0.686}y^{-0.375}(1 + \phi)^{0.198} \quad (18)$$

**6.4. Effect of Twist Tape Configuration.** The influence of and conic (quadrant, parabolic half, and triangular) cut twisted tape of twist ratio  $y = 2.93$  and cut depth  $d_e = 0.5$  cm with 2% volume concentration of  $SiO_2$  nanofluid on Nusselt number and friction factor are shown in Figures 22 and 23. Apparently from Figure 22, conic cut twist exhibits higher Nusselt number than the typical twisted tape. This can be explained by the fact that conic cut twist tape generates swirl flow with efficient fluid mixing nearby their alternative cuts while the typical twist tape causes swirl flow only. The results also reveal that the triangular cut twisted tape provides a higher Nusselt number compared with the others. This means that the vortices behind the alternative cut edges of triangular cut twist tape give superior efficient fluid mixing resulting in further heat transfer enhancement. From Figure 23, it can be seen that friction factor decreases with the increase of Reynolds number and triangular cut twisted tape (VCT) gives higher friction factor compared with all the other Reynolds numbers. This implies that the influence of alternative cuts along the edge of the triangular cut twisted tape promotes additional wall shear stress due to flow mixing between the fluids at the twist tape and tube wall. In addition, the experimental data of conic cut twisted tapes with water ( $\phi = 0$ ) and nanofluids ( $\phi = 2\%$ ) were used to develop the

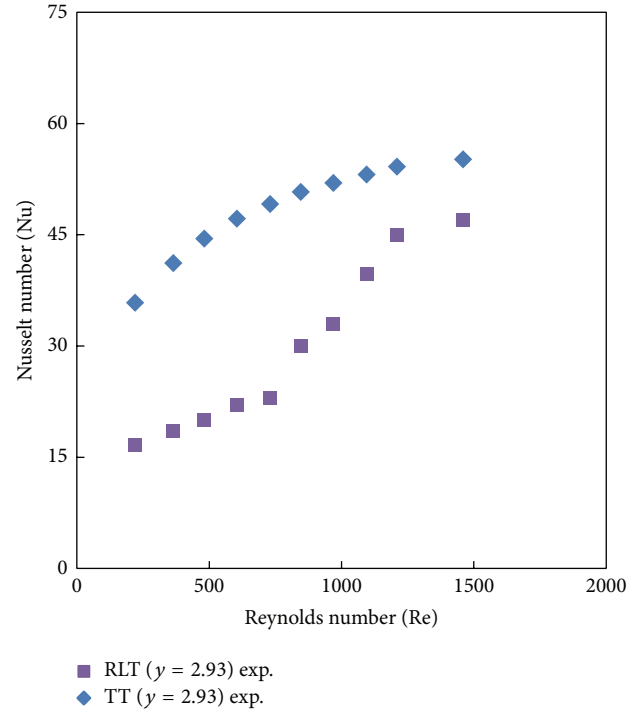


FIGURE 12: Experimental Nusselt number of typical twist tape with RLT inserts.

following correlations for Nusselt number and friction factor with reasonable agreement as shown in Figures 24 and 25.

For triangular cut twisted tape,

$$Nu = 5.387Pr^{0.4}Re^{0.229}\left(1 + \frac{w}{W}\right)^{0.0383}\left(1 + \frac{d_e}{W}\right)^{-0.185} \cdot (1 + \phi)^{0.025}, \quad (19)$$

$$f = 61.84Re^{-0.67}\left(1 + \frac{w}{W}\right)^{0.127}\left(1 + \frac{d_e}{W}\right)^{-0.468} \cdot (1 + \phi)^{0.137}. \quad (20)$$

For parabolic half cut twisted tape,

$$Nu = 5.388Pr^{0.4}Re^{0.229}\left(1 + \frac{w}{W}\right)^{0.0384}\left(1 + \frac{d_e}{W}\right)^{-0.184} \cdot (1 + \phi)^{0.025}, \quad (21)$$

$$f = 68.76Re^{-0.67}71\left(1 + \frac{w}{W}\right)^{0.137}\left(1 + \frac{d_e}{W}\right)^{-0.197} \cdot (1 + \phi)^{0.0134}. \quad (22)$$

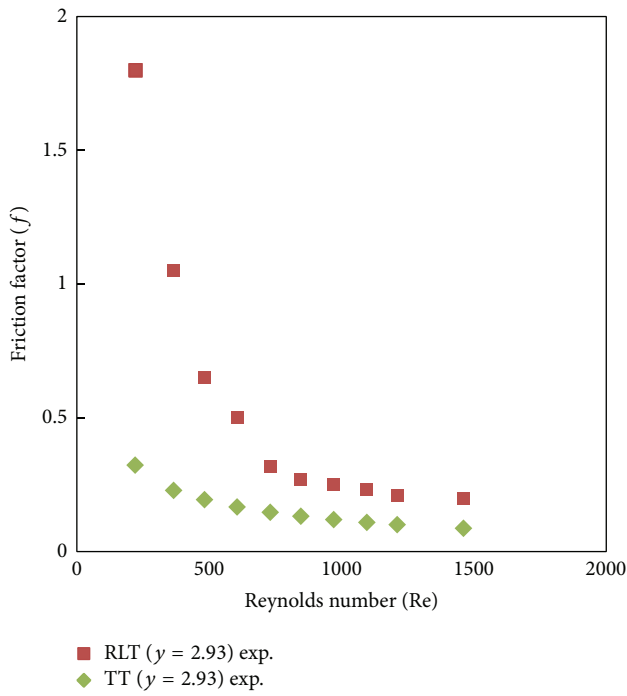


FIGURE 13: Experimental friction factor of typical twist tape with RLT inserts.

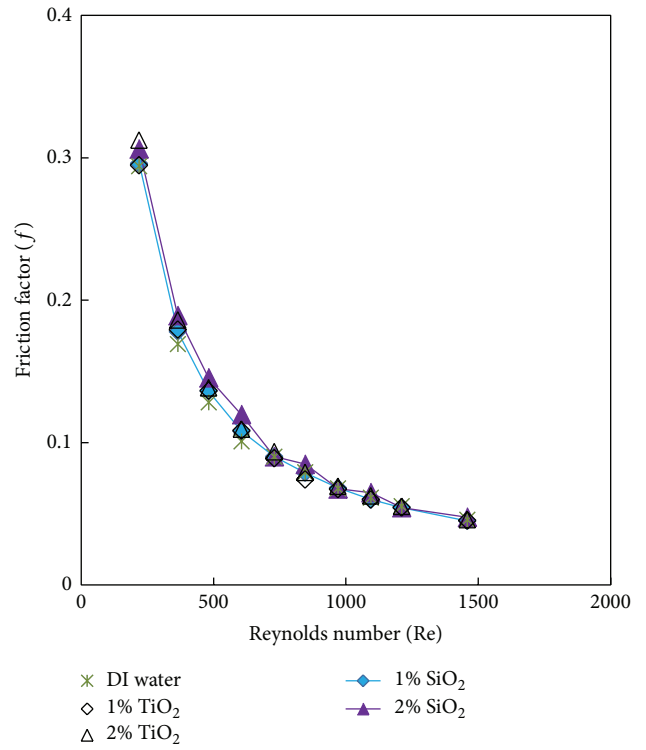


FIGURE 15: Friction factor versus Reynolds number for plain tube with nanofluids.

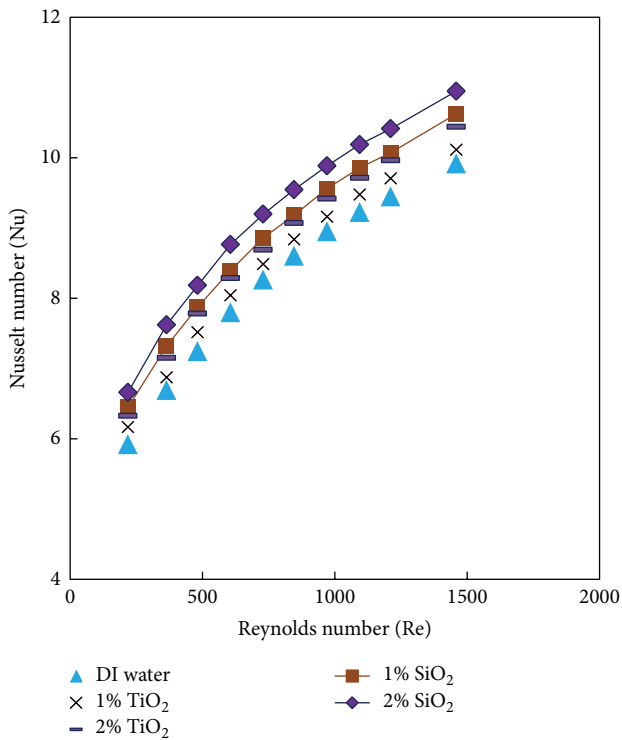


FIGURE 14: Nusselt number versus Reynolds number for plain tube with nanofluids.

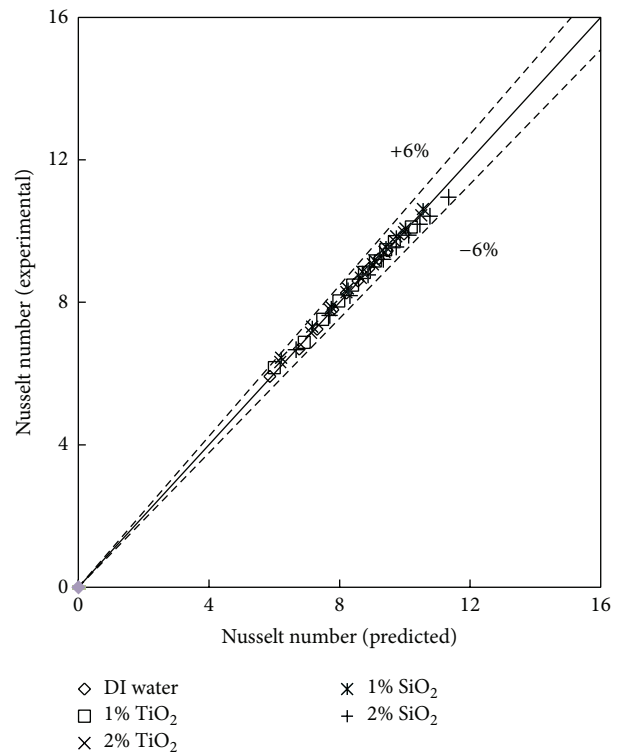


FIGURE 16: Comparison of experimental and predicted Nusselt number for plain tube.

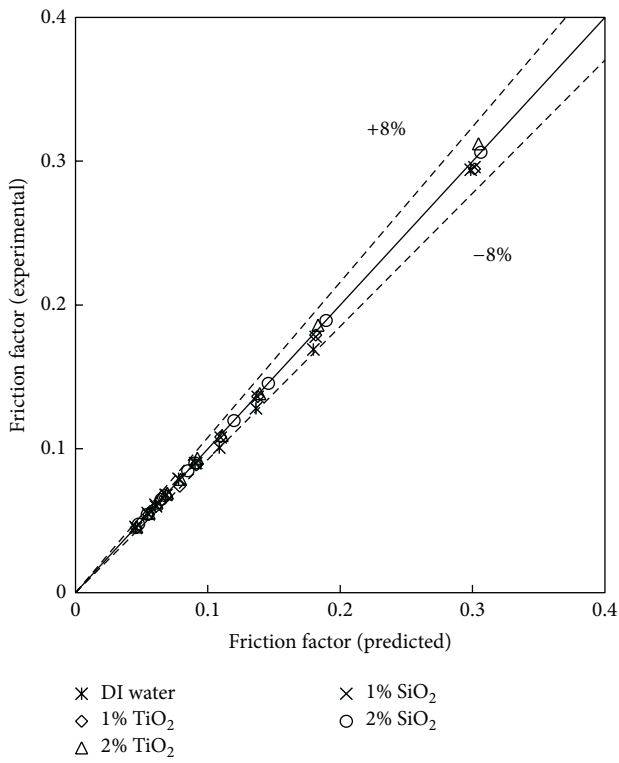


FIGURE 17: Comparison of experimental and predicted friction factor for plain tube.

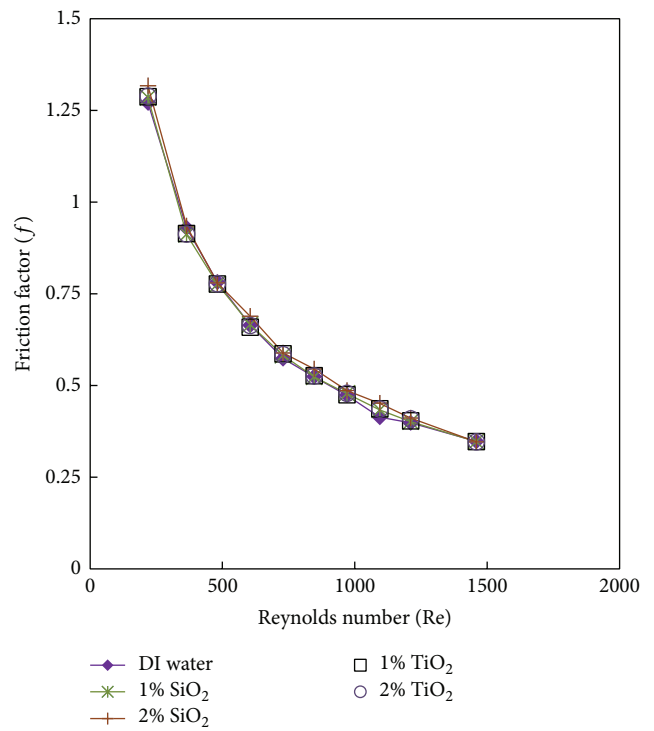


FIGURE 19: Nusselt number versus Reynolds number for nanofluids with typical twist tape ( $\gamma = 2.93$ ).

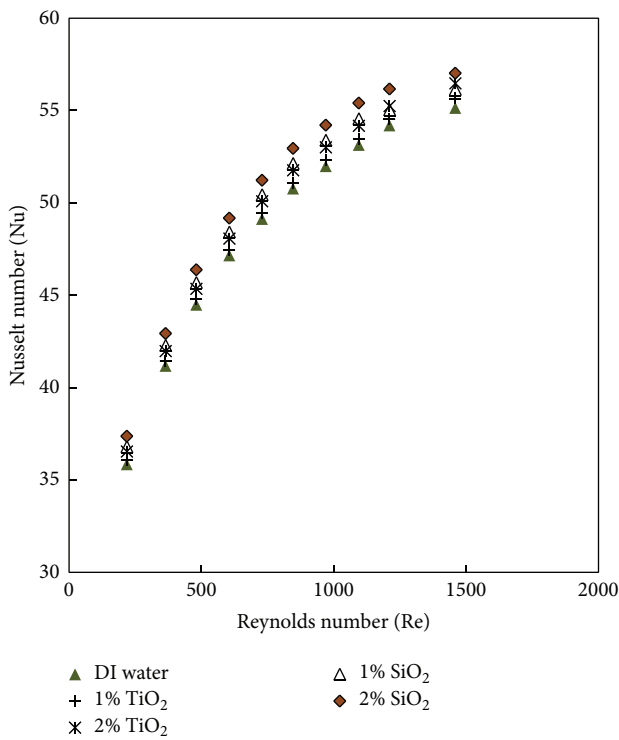


FIGURE 18: Nusselt number versus Reynolds number for nanofluids with typical twist tape ( $\gamma = 2.93$ ).

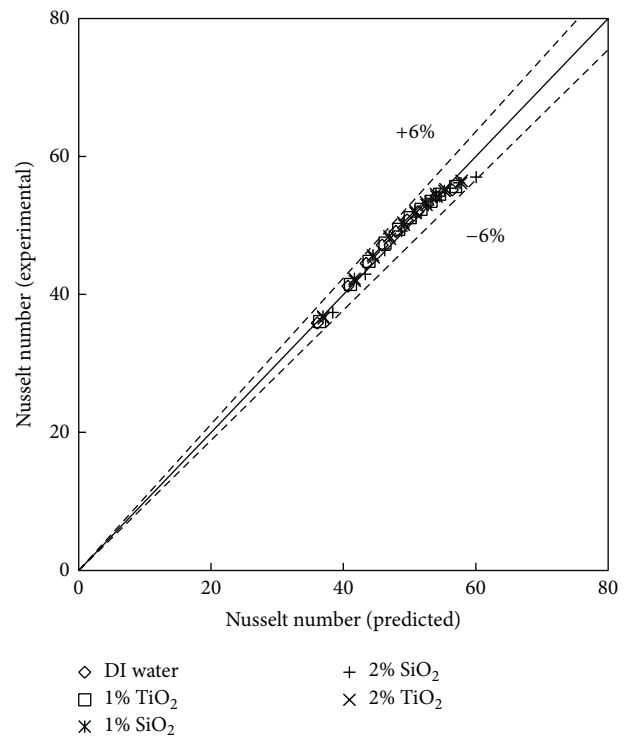


FIGURE 20: Comparison of experimental and predicted Nusselt number with typical twist tape.

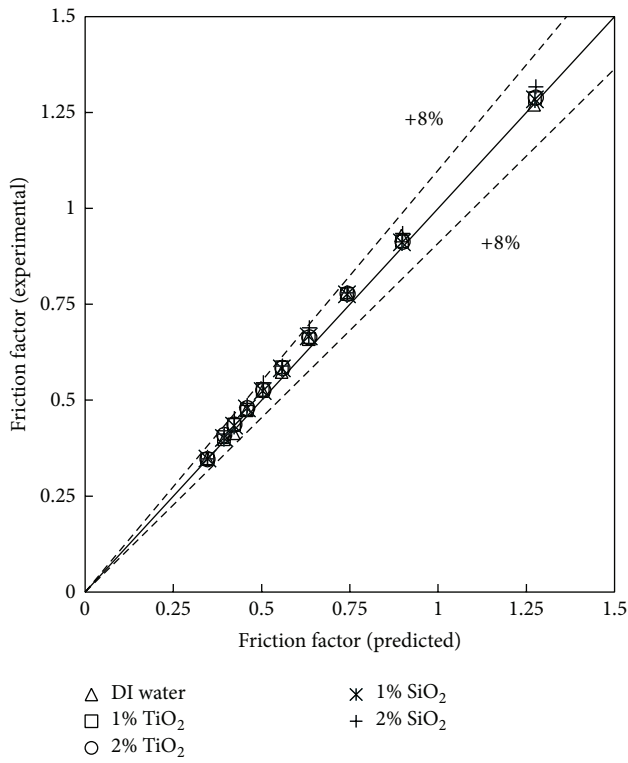


FIGURE 21: Comparison of experimental and predicted friction factor with typical twist tape.

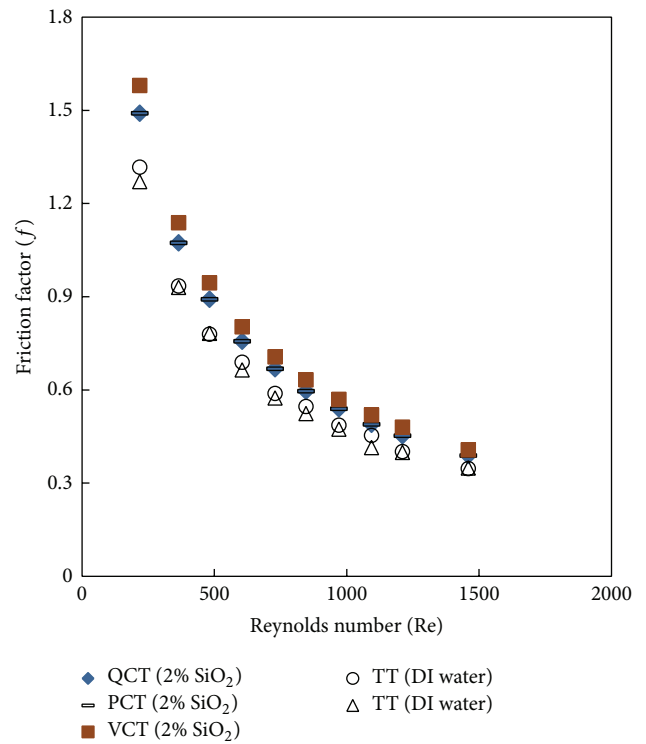


FIGURE 23: Friction factor versus Reynolds number for typical and conic cut twist tapes.

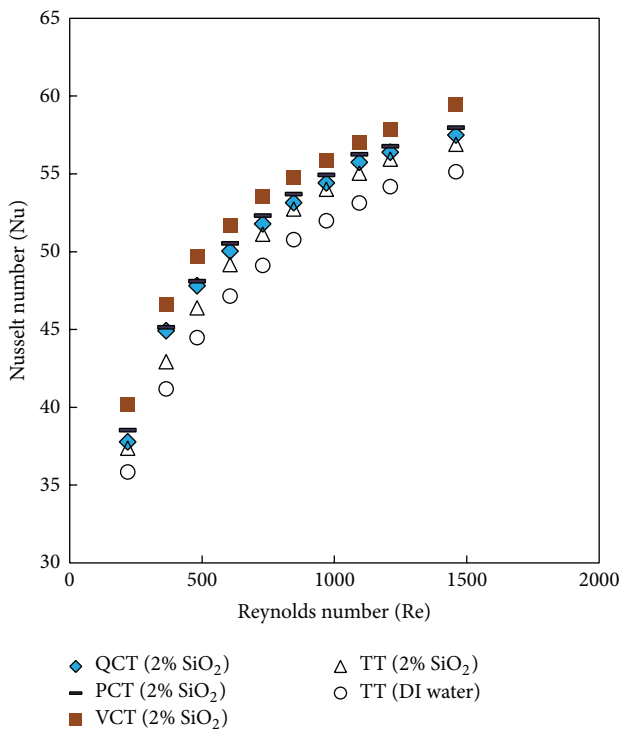


FIGURE 22: Nusselt number versus Reynolds number for typical and conic cut twist tapes.

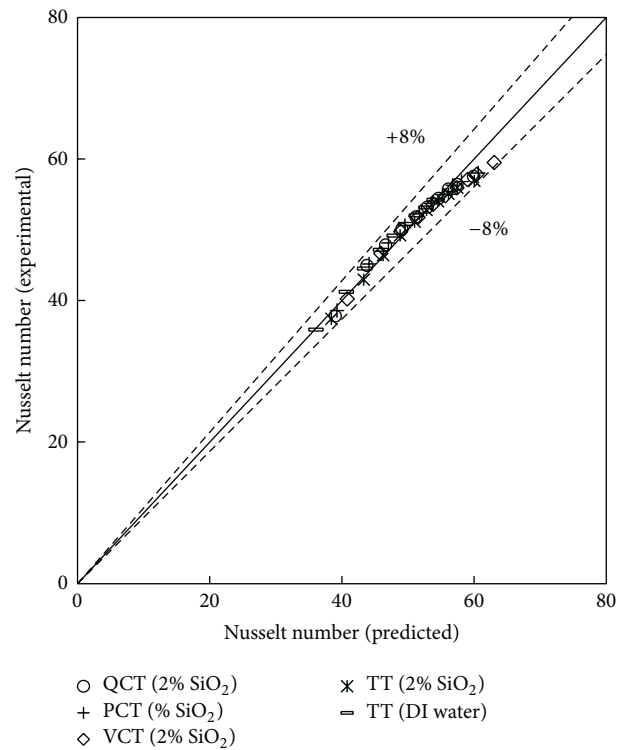


FIGURE 24: Comparison of experimental and predicted Nusselt number for typical and conic cut twist tapes.

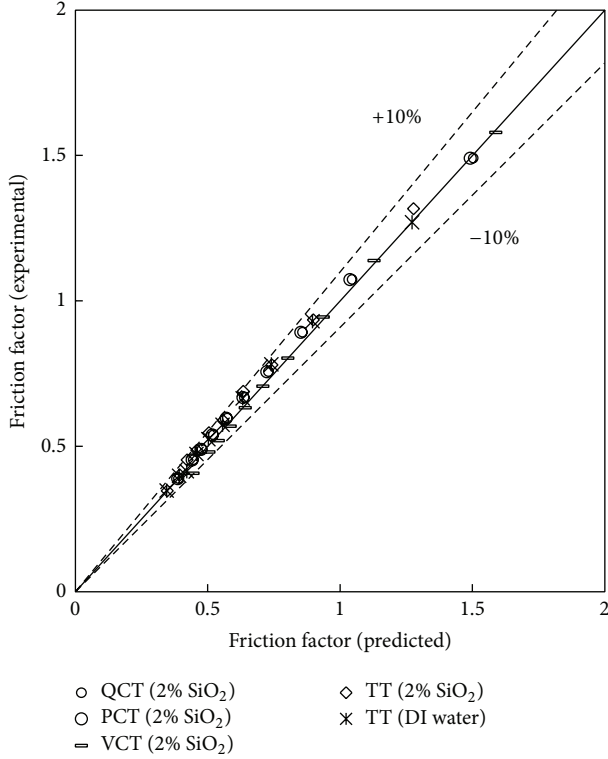


FIGURE 25: Comparison of experimental and predicted friction factor for typical and conic cut twist tapes.

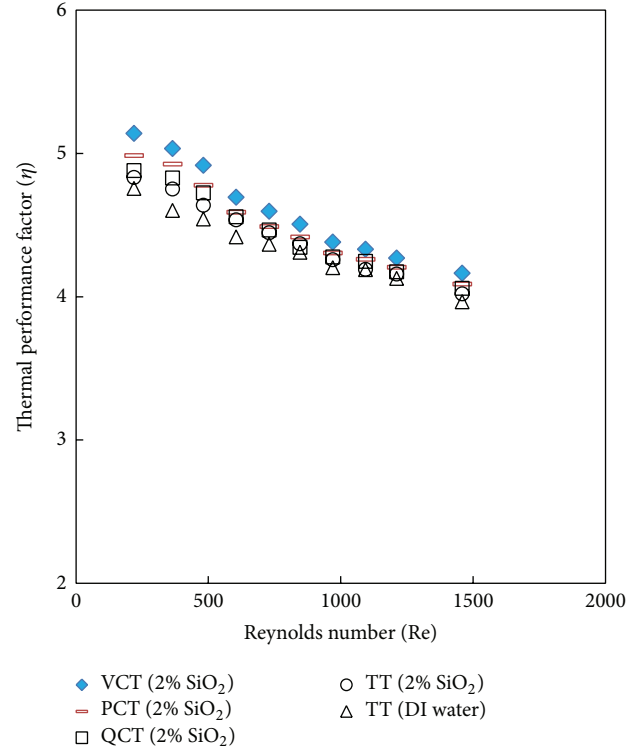


FIGURE 26: Variation of the thermal performance factor of typical and conic cut twist tape.

For quadrant cut twisted tape,

$$Nu = 5.38Pr^{0.4}Re^{0.226} \left(1 + \frac{w}{W}\right)^{0.0387} \left(1 + \frac{d_e}{W}\right)^{-0.187} \cdot (1 + \phi)^{0.027}, \quad (23)$$

$$f = 69.13Re^{-0.71} \left(1 + \frac{w}{W}\right)^{0.127} \left(1 + \frac{d_e}{W}\right)^{-0.16} \cdot (1 + \phi)^{0.31}. \quad (24)$$

**6.5. Thermal Performance of Twist Tapes.** The performance analysis of typical and conic cut twisted tape inserts in laminar flow of SiO<sub>2</sub> nanofluid was accomplished by evaluating thermal performance factor for constant pumping power condition. Thermal performance factor ( $\eta$ ) at constants pumping power is defined as ratio of the convective heat transfer coefficient of the tube with turbulator or enhancing method to that of the plain tube. The following thermal performance factor for laminar proposed by [29] is used for performance analysis:

$$\eta = \frac{(Nu/Nu_o)}{(f/f_o)^{0.1666}}, \quad (25)$$

where Nu,  $f$ , Nu<sub>o</sub>, and  $f_o$  are the Nusselt numbers and friction factors for a duct configuration with and without inserts, respectively.

Figure 26 shows the variation of thermal performance factor with Reynolds number for 2% volume concentration of SiO<sub>2</sub> nanofluid. The values of thermal performance factor at all Reynolds were found to be greater than unity for both typical and conic cut twisted tape inserts. This indicates that twist tape inserts are feasible in terms of energy saving in laminar flow regime. It is evident that the thermal performance factor triangular cut twist tape at constant Reynolds number is higher than other twist tapes. This is due to the stronger turbulence/swirl flow generated by alternative cuts along the edge twist tape. The thermal performance factor was found to be decreasing with increases in Reynolds number. This is because of the increase in pressure loss as the Reynolds number increases.

The experimental results showed that the thermal performance factor is around 5.13–4.16 for VCT, 4.98–4.08 for PCT, 4.88–4.05 for QCT, and 4.83–4.01 for TT when used with 2% SiO<sub>2</sub> nanofluid. While the thermal performance factor to be around 4.75–3.96 for TT with water. Therefore, the VCT insert shows better thermal performance when used with SiO<sub>2</sub> nanofluid than other twist tapes. The experimental results are used to derive the following correlations of thermal performance factor using least square method of regression analysis. These correlations are valid for laminar flow (Re < 1500) of water and 2% volume concentration SiO<sub>2</sub> for typical and conic cut twist tapes. The comparisons between the thermal performance factor values obtained from experimental data and those predicted from the above correlations are

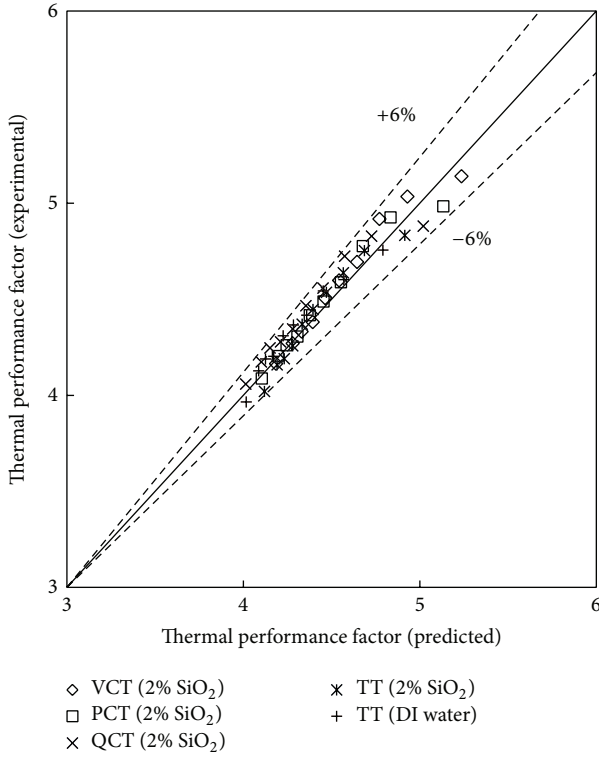


FIGURE 27: Comparison of experimental and predicted thermal performance for typical and conic cut twist tapes.

shown in Figure 27. As shown, the predicted data are in good agreement with the experimental data.

For VCT twisted tape,

$$\eta = 5.173\text{Re}^{-0.118} \left(1 + \frac{w}{W}\right)^{2.483} \left(1 + \frac{d_e}{W}\right)^{-0.247} \cdot (1 + \phi_{\text{SiO}_2})^{0.0183}. \quad (26)$$

For PCT twisted tape,

$$\eta = 5.173\text{Re}^{0.0945} \left(1 + \frac{w}{W}\right)^{3.113} \left(1 + \frac{d_e}{W}\right)^{-0.247} \cdot (1 + \phi_{\text{SiO}_2})^{0.0183}. \quad (27)$$

For QCT twisted tape,

$$\eta = 5.173\text{Re}^{0.118} \left(1 + \frac{w}{W}\right)^{3.49} \left(1 + \frac{d_e}{W}\right)^{-0.247} \cdot (1 + \phi_{\text{SiO}_2})^{0.0183}. \quad (28)$$

For TT twisted tape with SiO nanofluid,

$$\eta = 7.91\text{Re}^{0.093} (1 + \phi_{\text{SiO}_2})^{1.283}. \quad (29)$$

For TT twisted tape with deionized water,

$$\eta = 7.91\text{Re}^{0.093}. \quad (30)$$

## 7. Conclusions

Heat transfer, friction, and thermal performance characteristics of SiO<sub>2</sub> and TiO<sub>2</sub> nanofluids with two concentrations of 1% and 2% by volume in a circular tube fitted with a typical and conic cut twist tape in the laminar regime have been experimentally investigated. The main conclusions from this experimental study are as follows.

- (7.1) SiO<sub>2</sub> and TiO<sub>2</sub> nanofluids of different volume concentration in plain tube give good enhancement in Nusselt number compared to deionized water. The higher enhancement in Nusselt number is obtained by SiO<sub>2</sub> nanofluids with volume concentrations of 2%.
- (7.2) At similar conditions, the insertion of typical twist tape causes very significant convective heat transfer enhancement in the laminar flow; however, further enhancement is observed by the simultaneous use of nanofluid with twisted tape compared to the use of twisted tape or nanofluid alone.
- (7.3) The use of nanofluid with the conic cut twist tape provides a considerably higher Nusselt number than that of nanofluid with the typical twist tape for all Reynolds numbers examined. The triangular cut twist tape offers higher heat transfer rate than the typical twist tape and other conic cut configurations.
- (7.4) Over the range investigated (Re = 220–1500), the maximum thermal performance factor of 5.13 is found with the simultaneous use of the triangular twist tape with SiO<sub>2</sub> nanofluid with 2% volume concentration at Reynolds number of 220.
- (7.5) The empirical correlations for the Nusselt number, friction factor, and the thermal performance factor for typical and conic cut twist tapes are developed and fitted with the experimental data of water and nanofluids.

## Conflict of Interests

The authors declare that there is no conflict of interests regarding the publication of this paper.

## Acknowledgments

The authors would like to thank the National University of Malaysia and the Ministry of Higher Education for the financial support (FRGS/1/2013/TK07/UKM/01/1 and DPP-2013-114) to perform this investigation.

## References

- [1] A. Bejan and A. D. Kraus, *Heat Transfer Handbook*, John Wiley & Sons, 2003.
- [2] I. Singh and N. Diwakar, *International Journal of Applied Research in Mechanical Engineering*, vol. 3, pp. 16–29, 2013.
- [3] R. M. Manglik and A. E. Bergles, “Heat transfer and pressure drop correlations for twisted-tape inserts in isothermal tubes:

- part I—laminar flows,” *Journal of Heat Transfer*, vol. 115, no. 4, pp. 881–889, 1993.
- [4] S. K. Saha and D. Chakraborty, “Heat transfer and pressure drop characteristics of laminar flow through a circular tube fitted with regularly spaced twisted tape elements with multiple twists,” in *Proceedings of the Heat and Mass Transfer Conference*, pp. 313–318, Kanpur, India, 1997.
- [5] S. Al-Fahed, L. M. Chamra, and W. Chakroun, “Pressure drop and heat transfer comparison for both microfin tube and twisted-tape inserts in laminar flow,” *Experimental Thermal and Fluid Science*, vol. 18, no. 4, pp. 323–333, 1998.
- [6] M. S. Lokanath and R. D. Misal, “An experimental study on the performance of plate heat exchanger and an augmented shell and tube heat exchanger for different types of fluids for marine applications,” in *Proceedings of the 5th ISHMT-ASME Heat and Mass Transfer Conference*, pp. 863–868, Tata McGraw-Hill, New Delhi, India, 2002.
- [7] P. Sivashanmugam and S. Suresh, “Experimental studies on heat transfer and friction factor characteristics of laminar flow through a circular tube fitted with helical screw-tape inserts,” *Applied Thermal Engineering*, vol. 26, no. 16, pp. 1990–1997, 2006.
- [8] P. Sivashanmugam and S. Suresh, “Experimental studies on heat transfer and friction factor characteristics of laminar flow through a circular tube fitted with regularly spaced helical screw-tape inserts,” *Experimental Thermal and Fluid Science*, vol. 31, no. 4, pp. 301–308, 2007.
- [9] S. Jaisankar, T. K. Radhakrishnan, and K. N. Sheeba, “Studies on heat transfer and friction factor characteristics of thermosiphon solar water heating system with helical twisted tapes,” *Energy*, vol. 34, no. 9, pp. 1054–1064, 2009.
- [10] A. V. N. Kapatkar, B. D. A. S. Padalkar, and C. S. Kasbe, “Experimental investigation on heat transfer enhancement in laminar flow in circular tube equipped with different inserts,” *AMAE International Journal on Manufacturing and Material Science*, vol. 1, pp. 1–6, 2011.
- [11] J. Guo, A. Fan, X. Zhang, and W. Liu, “A numerical study on heat transfer and friction factor characteristics of laminar flow in a circular tube fitted with center-cleared twisted tape,” *International Journal of Thermal Sciences*, vol. 50, no. 7, pp. 1263–1270, 2011.
- [12] K. Wongcharee and S. Eiamsa-ard, “Friction and heat transfer characteristics of laminar swirl flow through the round tubes inserted with alternate clockwise and counter-clockwise twisted-tapes,” *International Communications in Heat and Mass Transfer*, vol. 38, no. 3, pp. 348–352, 2011.
- [13] E. Z. Ibrahim, “Augmentation of laminar flow and heat transfer in flat tubes by means of helical screw-tape inserts,” *Energy Conversion and Management*, vol. 52, no. 1, pp. 250–257, 2011.
- [14] S. U. S. Choi and J. A. Eastman, “Enhancing thermal conductivity of fluids with nanoparticles,” in *Developments and Applications of Non-Newtonian Flows*, D. A. Siguier and H. P. Wang, Eds., pp. 99–105, American Society of Mechanical Engineers, New York, NY, USA, 1995.
- [15] C. Y. Tsai, H. T. Chien, P. P. Ding, B. Chan, T. Y. Luh, and P. H. Chen, “Effect of structural character of gold nanoparticles in nanofluid on heat pipe thermal performance,” *Materials Letters*, vol. 58, no. 9, pp. 1461–1465, 2004.
- [16] M.-S. Liu, M. C.-C. Lin, C. Y. Tsai, and C.-C. Wang, “Enhancement of thermal conductivity with Cu for nanofluids using chemical reduction method,” *International Journal of Heat and Mass Transfer*, vol. 49, no. 17–18, pp. 3028–3033, 2006.
- [17] E. Tamjid and B. H. Guenther, “Rheology and colloidal structure of silver nanoparticles dispersed in diethylene glycol,” *Powder Technology*, vol. 197, no. 1–2, pp. 49–53, 2010.
- [18] S. M. S. Murshed, K. C. Leong, and C. Yang, “Enhanced thermal conductivity of TiO<sub>2</sub> water based nanofluids,” *International Journal of Thermal Sciences*, vol. 44, no. 4, pp. 367–373, 2005.
- [19] H. Zhu, C. Zhang, S. Liu, Y. Tang, and Y. Yin, “Effects of nanoparticle clustering and alignment on thermal conductivities of Fe<sub>3</sub>O<sub>4</sub> aqueous nanofluids,” *Applied Physics Letters*, vol. 89, Article ID 023123, 2006.
- [20] J. A. Eastman, U. S. Choi, S. Li, L. J. Thompson, and S. Lee, “Enhanced thermal conductivity through the development of nanofluids,” *MRS Proceedings*, vol. 457, 1996.
- [21] M. E. Meibodi, M. Vafaie-Sefti, A. M. Rashidi, A. Amrollahi, M. Tabasi, and H. S. Kalal, “Simple model for thermal conductivity of nanofluids using resistance model approach,” *International Communications in Heat and Mass Transfer*, vol. 37, no. 5, pp. 555–559, 2010.
- [22] G. Pathipakka and P. Sivashanmugam, “Heat transfer behaviour of nanofluids in a uniformly heated circular tube fitted with helical inserts in laminar flow,” *Superlattices and Microstructures*, vol. 47, no. 2, pp. 349–360, 2010.
- [23] K. Wongcharee and S. Eiamsa-ard, “Enhancement of heat transfer using CuO/water nanofluid and twisted tape with alternate axis,” *International Communications in Heat and Mass Transfer*, vol. 38, no. 6, pp. 742–748, 2011.
- [24] S. Suresh, K. P. Venkataraj, and P. Selvakumar, “Comparative study on thermal performance of helical screw tape inserts in laminar flow using Al<sub>2</sub>O<sub>3</sub>/water and CuO/water nanofluids,” *Superlattices and Microstructures*, vol. 49, no. 6, pp. 608–622, 2011.
- [25] S. D. Salman, A. A. H. Kadhum, M. S. Takriff, and A. B. Mohamad, “Heat transfer enhancement of laminar nanofluids flow in a circular tube fitted with parabolic-cut twisted tape inserts,” *The Scientific World Journal*, vol. 2014, Article ID 543231, 7 pages, 2014.
- [26] S. D. Salman, A. A. H. Kadhum, M. S. Takriff, and A. B. Mohamad, “CFD simulation of heat transfer and friction factor augmentation in a circular tube fitted with elliptic-cut twisted tape inserts,” *Mathematical Problems in Engineering*, vol. 2013, Article ID 163839, 7 pages, 2013.
- [27] S. D. Salman, A. A. H. Kadhum, M. S. Takriff, and A. B. Mohamad, “CFD analysis of Heat transfer and friction factor characteristics in a circular tube fitted with Quadrant-cut twisted tape inserts,” *Mathematical Problems in Engineering*, vol. 2013, Article ID 273764, 8 pages, 2013.
- [28] F. P. Incropera, D. P. Dewitt, T. L. Bergman, and A. S. Lavine, *Fundamentals of Heat and Mass Transfer*, John Wiley & Sons, 2007.
- [29] H. Usui, Y. Sano, K. Iwashita, and A. Isozaki, “Enhancement of heat transfer by a combination of internally grooved rough tube and twisted tape,” *International Chemical Engineering*, vol. 26, no. 1, pp. 97–104, 1986.
- [30] J. P. Holman, *Experimental Methods for Engineers*, McGraw-Hill, New York, NY, USA, 2011.
- [31] R. K. Shah and A. L. London, *Laminar Flow Forced Convection in Ducts*, Academic Press, New York, NY, USA, 1978.

- [32] P. K. Nagarajan and P. Sivashanmugam, "CFD simulation of heat transfer augmentation in a circular tube fitted with right-left helical inserts with spacer," *International Journal of Chemical Engineering Research*, vol. 1, pp. 1-11, 2009.
- [33] P. Keblinski, S. R. Phillpot, S. U. S. Choi, and J. A. Eastman, "Mechanisms of heat flow in suspensions of nano-sized particles (nanofluids)," *International Journal of Heat and Mass Transfer*, vol. 45, no. 4, pp. 855-863, 2002.

## Review Article

# A Review on the Fabrication of Electrospun Polymer Electrolyte Membrane for Direct Methanol Fuel Cell

**Hazlina Junoh,<sup>1,2</sup> Juhana Jaafar,<sup>1,2</sup> Muhammad Noorul Anam Mohd Norddin,<sup>1,2</sup> Ahmad Fauzi Ismail,<sup>1,2</sup> Mohd Hafiz Dzarfan Othman,<sup>1,2</sup> Mukhlis A. Rahman,<sup>1,2</sup> Norhaniza Yusof,<sup>1,2</sup> Wan Norhayati Wan Salleh,<sup>1,2</sup> and Hamid Ilbeygi<sup>3</sup>**

<sup>1</sup>Advanced Membrane Technology Research Centre (AMTEC), Universiti Teknologi Malaysia, 81310 Johor Bahru, Johor, Malaysia

<sup>2</sup>Faculty of Petroleum and Renewable Energy Engineering, Universiti Teknologi Malaysia, 81310 Johor Bahru, Johor, Malaysia

<sup>3</sup>Australian Institute for Bioengineering and Nanotechnology (AIBN), The University of Queensland, Building 75, Corner of College and Copper Roads, St Lucia, Brisbane, QLD 4072, Australia

Correspondence should be addressed to Juhana Jaafar; juhana@petroleum.utm.my

Received 16 July 2014; Revised 19 August 2014; Accepted 19 August 2014

Academic Editor: Raghu N. Bhattacharya

Copyright © 2015 Hazlina Junoh et al. This is an open access article distributed under the Creative Commons Attribution License, which permits unrestricted use, distribution, and reproduction in any medium, provided the original work is properly cited.

Proton exchange membrane (PEM) is an electrolyte which behaves as important indicator for fuel cell's performance. Research and development (R&D) on fabrication of desirable PEM have burgeoned year by year, especially for direct methanol fuel cell (DMFC). However, most of the R&Ds only focus on the parent polymer electrolyte rather than polymer inorganic composites. This might be due to the difficulties faced in producing good dispersion of inorganic filler within the polymer matrix, which would consequently reduce the DMFC's performance. Electrospinning is a promising technique to cater for this arising problem owing to its more widespread dispersion of inorganic filler within the polymer matrix, which can reduce the size of the filler up to nanoscale. There has been a huge development on fabricating electrolyte nanocomposite membrane, regardless of the effect of electrospun nanocomposite membrane on the fuel cell's performance. In this present paper, issues regarding the R&D on electrospun sulfonated poly (ether ether ketone) (SPEEK)/inorganic nanocomposite fiber are addressed.

## 1. Introduction

Currently, the electrospun polymer nanofibers have become important in various applications such as biomedical [1–3], environmental protection [4, 5], catalyst and enzyme carriers [6, 7], sensors [3], energy harvest and storage, and many more, due to the property of the one-dimension nanomaterials which have larger surface area and high porosity [8]. A nanofiber can be synthesized via drawing, template, self-assembly, melt blowing, and phase separation [2]. However, these methods are not favorable in industrial practice as producing continuous nanofibers is time consuming compared to the electrospinning method. Within the past few years, the development of a nanocomposite fiber has flourished rapidly and the research and development of the nanocomposite electrospun fiber are starting to grow by adapting the electrospinning method.

Nanocomposite as a layered silicates-polymer is a promising alternative due to the physicochemical, thermal, and mechanical stability of the pure polymer [9]. The manipulation of the advantages offered by layered silicates-polymer nanocomposite membrane has given an insight in developing a new electrolyte for fuel cell system in order to cater for the problem arising via methanol crossover, as well as maintaining or improving the proton conductivity of the fuel cell system, especially on direct methanol fuel cell (DMFC). Compared to the corresponding pure polymer membranes, as well as commercial Nafion membranes, many polymer-inorganic nanocomposite membranes have shown much lower fuel permeability, along with having similar or improved proton conductivity with the nanodispersion of layered silicates throughout the polymer matrix [10]. In general, the smaller the particle sizes of the inorganic fillers are, the larger the conductivity enhancement will be, at

the same time lowering the methanol permeation. Jaafar et al. [11] conducted an experiment on sulfonated poly (ether ether ketone) (SPEEK) with the addition of Cloisite15A nanofiller having a good compatibility, which showed a slight improvement in the barrier properties of SPEEK. Thus, it has been proven that a good dispersion of Cloisite15A nanofillers with smaller particle size can provide the tortuous path for methanol and eventually decrease the permeability of the methanol.

On the other hand, the research and development on the exact connectivity structure properties within the nanocomposite electrolyte polymer are still in the primary stage and understanding of the ionic conductivity phenomenon in polymer nanocomposite electrolyte is still incomplete. Even so, a large surface area of dispersed nanosized particles within the polymer matrix will decrease the degree of crystallinity of the polymer segments, relative to the ionic mobility in nanocomposite polymer electrolyte membrane system [12, 13]. Hence, the random dispersion of particles within the polymer matrix can enhance the mobility of ion and eventually perform effectively in the conductivity of fuel cell [14]. Thus, the combination of nanosized particles and specialty polymer electrolyte brings the focus of the study on nanocomposite polymer electrolyte membrane within laboratory, as well as in industrial aspect.

From the morphological point of view, exfoliated polymer-inorganic nanocomposites have been found to be more promising structures than intercalated or ordinary composites, which have a great potential to exhibit high performance nanocomposites [15]. The potential of electrospinning in preparing a homogeneous dispersion of filler within the polymer matrix was studied by Bian [16]. In the study, he found that the dispersion of nanofiller within polymer matrix could be improved by applying electrospinning method compared to the conventional method. The scanning electron microscopy (SEM) images and energy dispersive X-ray (EDX-mapping) showed a homogeneous distribution of filler within the polymer matrix, as well as the reduction on agglomerations of the fillers. Therefore, electrospinning process can contribute to the development of exfoliated polymer-inorganic nanocomposite structure and improve the dispersion of Cloisite15A particles in the SPEEK matrices.

## 2. Electrolyte Membrane

In DMFC applications, an electrolyte membrane is called a “proton exchange membrane,” which refers to the acid electrolyte and certain polymers that contain free  $H^+$  ions. In other words, this proton exchange membrane only can serve for transferring  $H^+$  within the electrolyte membrane from anode to cathode or vice versa effectively [17]. A good proton exchange membrane should have good intrinsic properties, which will enable them to work effectively in fuel cell applications [18, 19]. These intrinsic properties include the following:

- (1) high proton conductivity to support high currents with minimal resistive losses and zero electronic conductivity;

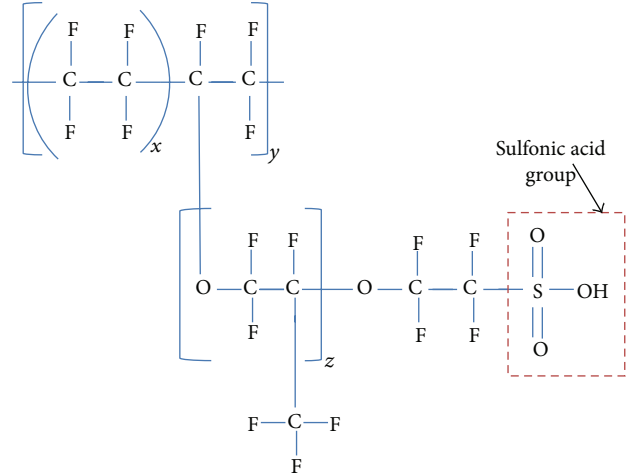


FIGURE 1: Structure of Nafion with sulfonic acid group ( $x = 5-13.5$ ,  $y = 1000$ ,  $z \geq 1$ ).

- (2) tolerable mechanical strength and stability;
- (3) chemical and electrochemical stability under operation conditions;
- (4) extremely low fuel or oxidant bypass to maximize columbic efficiency;
- (5) low water transport through diffusion;
- (6) electroosmosis and capability for fabrication into membrane electrode assemblies.

Conventionally, Nafion serves as an electrolyte in hydrogen-oxygen fuel cell applications, which are mostly used in proton exchange membrane fuel cell (PEMFC) and DMFC, due to the presence of higher conductivity and thermal stability of the Nafion [20]. The presence of sulfonic acid groups at the side chain of the Nafion makes it possible for proton conductivity [21] (Figure 1). Water present in the hydrophilic regions solvates the protons of the sulfuric acid groups and allows the protons to “hop” through the channels [21]. In case of DMFC, the protons will hop from anode to cathode.

However, Nafion faces several challenges which limit its industrial applications. One of the drawbacks is the high production cost, as well as low conductivity at high temperatures, due to fast dehydration and loss of fluorine ion affected by OH radical attack [22]. The most apparent drawback of the Nafion membrane in DMFC applications is methanol crossover and decrease in conductivity at temperature higher than  $100^{\circ}C$  [20]. Li et al. [23] found that the replacement of Nafion 115 membrane with SPEEK gave a significant increase in performance on DMFC application since methanol permeation is generally much lower compared to Nafion 115. However, the proton conductivity was found to remain barely unchanged at the operating temperature of  $80^{\circ}C$ .

The proton exchange membrane (PEM) primarily consists of many proton-conductive functional groups, which only allow a proton to transfer from one group to another [18]. The proton conductivity of the ionomer membrane

TABLE 1: Overview on electrolyte composite membrane for fuel cell application.

Matrix Polymer	Fillers	Proton conductivity	Methanol permeability	Filler's distribution	Type of fuel cell	Ref.
SPEEK	Cloisite 15A/TAP	Lower than Nafion 112	Significantly reduced	Partially exfoliated	DMFC	[11]
SPEEK	MMT/silicotungstic acid	Slight enhancement of proton conductivity	Suppressed	—	DMFC	[22]
PVOH	Cloisite Na <sup>+</sup> /phosphotungstic acid	Slight decrease of ionic conductivity	~88% reduced with respect to neat polymer	Exfoliated	DMFC	[24]
SPEEK	Silica sulfuric acid (SSA)	18.6% higher than pristine SPEEK 8.6% higher than Nafion 117	—	—	PEMFC	[80]
SPEEK	Heteropolyacids (HPA)	Higher than Nafion	—	—	PEMFC	[81]
Nafion	Organoclay, montmorillonite (Cloisite10A)	Remains similar to Nafion 117	Slightly decreases compared to the Nafion 117	Exfoliated	DMFC	[82]
Nafion	Montmorillonite (MMT)	Comparable with unmodified Nafion	Significantly decreases compared to unmodified Nafion	Exfoliated	DMFC	[83]
Nafion	Laponite	Higher than commercial Nafion membrane	—	—	PEMFC	[84]

depends on the presence of water, but due to the high evaporation rate at temperature above 100°C, the membrane undergoes a drastic dehydration and will eventually have its conductivity potential reduced. In order to cater for these behaviors of the membrane especially at high temperature, some approaches have been pursued [20]. New approaches such as modified perfluorinated ionomer membrane, acid-base blends, and new electrolyte composite membrane based on proton conducting materials [20] have been shown as promising solution regarding proton conductivity and methanol barrier properties. The new electrolyte composite membranes consist of polymer and other inorganic fillers such as silica, zirconium phosphate, and heteropolyacid. However, the methanol barrier properties are still lacking due to the size and shape of the fillers [24]. Dispersion degrees of inorganic fillers within the polymer matrix are important since they will determine whether the nanocomposite will form either as an intercalated, exfoliated or flocculated nanocomposite membrane [25]. Some of the modified parent matrix polymers for fuel cell application are summarized in Table 1.

Other than that, a novel application of SPEEK/Cloisite15A on microbial fuel cell (MFC) system has been pursued by Yusof et al. [26]. In their research, they found that the use of SPEEK incorporated with Cloisite15A could enhance the performance of MFC system in terms of water uptake, dissolved oxygen permeability, and morphology, which became more uniform with a lot of small pores, and the surface was smoother compared to the SPEEK membrane. However, the mechanical strength of the composite membrane was not

improved, due to the higher degree of sulfonation (76% DS) which lowered the mechanical strength. The higher degree of sulfonation signifies a high content of SO<sub>3</sub><sup>-</sup> ion, which functions to absorb more protons as well as water in the system, whereas a lower degree of sulfonation (41–60%) could absorb much lesser protons compared to the Nafion membrane [27] which needs to be avoided. Thus, a moderate degree of sulfonation is crucial in order to maintain the mechanical strength of the electrolyte membrane.

Other than Cloisite15A, the incorporation of sulfonated silica nanoparticles within sulfonated polymers membrane can also improve the thermal stability and methanol barrier properties. Su et al. [28] studied the effect of sulfonated silica nanoparticles on the proton conductivity instead of methanol permeability in sulfonated poly (phthalazinone ether ketone) polymer matrix for DMFC. In their study, they found that the interaction between the sulfonated silica nanoparticles and the sulfonated polymer could enhance a continuous proton conductive pathway for better proton conductivity. Furthermore, Gosalawit et al. [29] in their study had found that the increase of sulfonated montmorillonite (S-MMT) loading content within the SPEEK membrane reduced the methanol permeability, whereas the proton conductivity was increased compared to the pristine SPEEK and Nafion 117 membranes for DMFC applications. From the latter study, it can be suggested that the introduction of sulfonated nanoparticles will significantly enhance proton conductivity but not methanol permeability. However, the improvement in proton conductivity has significantly suppressed the methanol permeability problem. Since methanol permeability is a major

concern in DMFC application, the study on the alternative approach in producing a desirable electrolyte membrane has been chosen as the main focus of this study.

### 3. Technique for Nanofiber Formation

Electrospinning is one of the techniques involved in nanofiber formation, which accommodates manipulation of polymers. High voltage electrostatic field is used to charge the surface of the polymer solution droplet and, thus will, induce the ejection of a liquid jet through the needle tip. At this rate, the electrostatic force overcomes the surface tension of the droplet and the formation of the Taylor cone is obtained when the solution exits the tip of the needle, which eventually leads to charged jet (Figure 2(a)) [30–33]. The formation of Taylor cone is proportional to the applied voltage, where the voltage keeps increasing until the equilibrium condition is achieved between the surface tension and the electrostatic force (Figure 2(c)). The electric field controls the route of charged jet and the solidified spun fiber will be collected by the rotating or stationary conductive collector [21, 31–34].

Compared with the conventional methods such as wet spinning, dry spinning, and melt spinning, the electrospinning method can produce a much larger specific surface area and smaller pores size having fiber diameter in the range of 10–1000 nm by adjusting the operating parameters of the electrospinning, whereas the conventional methods can only produce fibers with diameter in the range of  $5 \times 10^3 \sim 500 \times 10^3$  nm [35]. Electrospinning can produce membranes with small diameter in the range of 10–1000 nm with high porosity due to random deposition on the collector [36]. Other than producing nanofiber, electrospinning has other advantages such as low cost, more capability, and high speed, which makes it highly potential in producing nanocomposite fiber [37]. The unique properties such as extremely long, large surface area, complex pore size, and complex alignment on either woven or nonwoven fiber possessed by electrospun nanofibers make it practical in various applications [8, 30, 38] especially in fuel cell system. Other than electrospinning process, drawing, template synthesis, phase separation, and self-assembly are other common methods for developing nanofibers [2]. However, due to the versatility possessed by electrospinning process, it is more favorable to be used in developing highly porous, patterned, and nanofibrous polymeric materials of nanofibers [39].

(i) *Drawing Process.* Drawing process can produce one to one long continuous single nanofiber as the dry spinning process in preparing hollow fiber membranes. However, only a viscoelastic material is used in this process, which can hold together firmly when the pulling process takes place in order to produce a nanofiber [2]. Bajáková et al. [40] in their study had successfully produced individual nanofibers consisting of polyvinyl alcohol (PVA), poly ( $\epsilon$ -caprolactone) (PCL), poly (vinyl butyral) (PVB), polyethylene oxide (PEO), and poly methyl methacrylate (PMMA) by pulling from the polymer droplets using a micropipette, respectively. The finest fibers

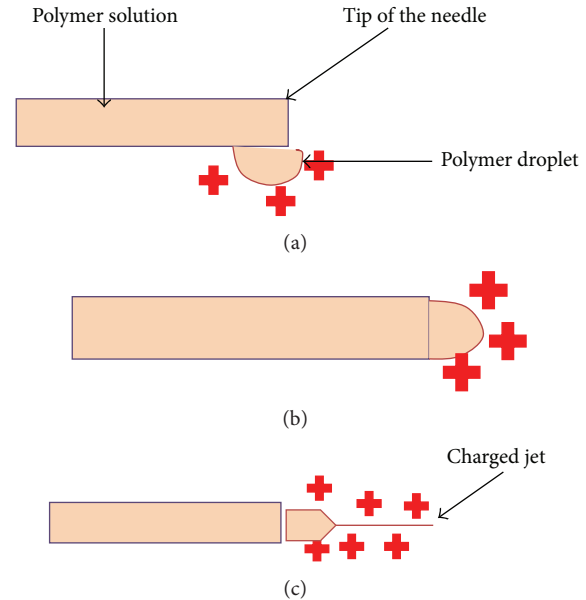


FIGURE 2: Formation of Taylor cone upon the equilibrium of electrostatic field, in which surface tension is achieved as the voltage is increased (Figure 2(c)).

from PVA with diameter of 200 nm were successfully produced.

(ii) *Template Synthesis.* Template synthesis is used to make nanofibers of solid or hollow shape. The most important aspect of this method may depend on the raw material used for fabricating the nanofibers. Unfortunately, a template synthesis can only produce discontinuous nanofibers that are unusually required in developing nanofibers in a big scale [2]. Martin [41] and his colleague had explored a template synthesis method in order to synthesize the desired material within the pores of a nanoporous membrane, in which he and his colleague had prepared tubules and fibrils composed of electronically conductive polymers, metals, semiconductors, carbons, and other materials.

(iii) *Phase Separation.* Phase separation consists of dissolution, gelatin, and lineage (extraction) which eventually gives a nanoscale porous foam formation. This phase separation process takes relatively a longer time to produce nanoporous foam from a solid polymer [2].

(iv) *Self-Assembly.* Self-assembly process is a process which involves an individual component, where preexisting components organize themselves into desired patterns and functions. However, this process also is a time consuming process in developing continuous polymer nanofibers [2].

Among the aforementioned preparation methods for polymer nanofibers, it can be concluded that the electrospinning method is the most versatile processing method compared to drawing, template synthesis, phase separation, and self-assembly methods, owing to the simple and easy production of polymer nanofibers. The electrospinning

TABLE 2: Parameters that influence the formation of fiber morphology and structure.

Solution parameters		Process parameters		Ambient parameter
Parameter (unit)	Range	Parameter (unit)	Range	
Concentration (wt.%)	1–40	Voltage (kV)	5–100	Humidity
Viscosity (cP)	20–300000	Electric field strength (kV/cm)	0.2–10	Pressure
Surface tension (mN/m)	20–75	Needle to collector distance (cm)	1–100	Temperature
Dielectric constant	15–90	Feed rate (ml/h)	0.01–5	
		Orifice diameter (mm)	0.1–3	

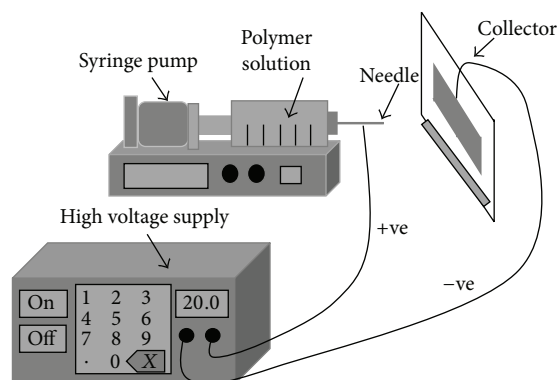


FIGURE 3: Basic setup of electrospinning consisting of needle connected to the infusion pump (constant flow rate for solution at the needle tip), high power supply (kV), and collector (either moving or stationary).

process can be advanced for mass production of long continuous nanofibers from various types of polymers, as well as metals and ceramics [42]. Furthermore, the electrospinning method can offer electrospun nanofibers with higher network ion exchange capability, which is crucial for proton transport process in fuel cell system, especially in DMFC.

#### 4. Electrospinning Process and Setup

Electrospinning is a simple and versatile method for generating an ultrafine fiber from rich variety materials which include polymer, composite, and ceramic. The electrospinning setup consists of three major components which are high voltage power supply, syringe with metal needle, and a conductive collector. The parameters that influence the morphology and structure of the produced electrospun fiber are listed in Table 2. However, these parameters generally depend upon the environmental condition in the respective state or country.

Electrospinning seems to be a very sophisticated but in fact a simple processing method of producing nanofiber. According to Liu et al. [43] the electrospinning process can be divided into several techniques such as vibration electrospinning, magneto-electrospinning, siro-electrospinning, and bubble electrospinning. Figure 3 shows the basic setup for electrospinning. As the charge liquid jet travels from the syringe tip to the collector, the mode of current flow changes from ohmic to convective flow as the charge migrates to

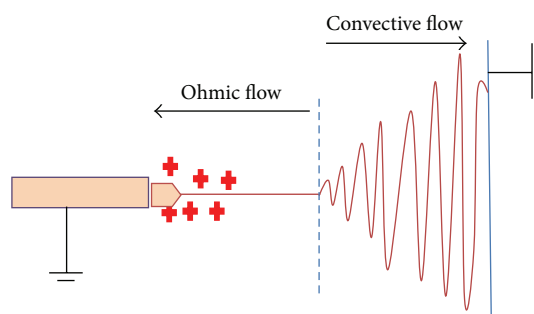


FIGURE 4: Mode of current flow for jet to travel from tip of the needle to collector.

the surface of the fiber (Figure 4). The ohmic flow is governed by a slow acceleration since the geometry of the Taylor cone [44] is controlled by the ratio of the surface tension to electrostatic repulsion. After overcoming the ohmic flow, the jet will travel at a rapid acceleration, which includes the zone of transition from liquid to dry solid. Eventually, the jet will penetrate the collector [21, 31–34, 45–48].

**4.1. Operating Parameters for Electrospinning.** As stated earlier, the electrospinning process is affected by three main parameters, which are solution parameters, process parameters, and ambient parameters. These operating parameters play a big role in determining the desired quality of the electrospun fiber produced [33, 49]. A fiber with diameter within 10–1000 nm in scale and a smooth surface morphology is the most preferred in many applications. According to Baji et al. [44], the solution properties are difficult to alter since the relation between one parameter will drag the other parameters and they are very difficult to isolate as one controllable parameter. Table 3 shows all three major parameters which can affect the morphology and diameter of the electrospun fiber.

Li and Wang [50] discussed the effects of working parameters that govern the electrospinning process, in which they found that these parameters could affect the fiber morphologies and diameters. Thompson et al. [51], in their study on the effects of the parameters on nanofiber diameter, found that the jet radius could affect the production of the electrospun fiber. In their study, parameters such as distance of needle to the collector, solution viscosity, diameter of the needle, charge density, and relaxation time greatly affected the fiber formation compared to other parameters. For instance,

TABLE 3: Parameters affecting morphology and diameter of the electrospun nanofiber [33].

Categories	Processing parameters
Solution properties	Type, confirmation, dipole moment, dielectric constant, crystallinity, glass transition temperature, molecular weight, molecular weight distribution of polymer, vapor pressure, polarity, surface tension of the solvent, viscosity/concentration, elasticity, and electrical conductivity of solution
Controlled variables	Solution feeding rate, electric field strength, distance between the tip of the needle and the collector, needle diameter, shape and length, composition, geometry, and motion of the collector
Ambient parameter	Temperature, humidity, and air velocity

TABLE 4: Electrospinning parameters and their effects on fiber morphology and fiber diameter.

Parameter	Remarks	Reference
Applied voltage	Deposition pattern of fibers changes from random orientation into a straight arrangement. Fiber bead density increases with increasing instability due to the increase of the applied voltage. Increasing applied voltage, thinning the fiber, reducing average diameter of the fiber, and causing multiple jets. Higher applied voltage broadens the distributions of the diameters of fiber.	[85–88]
Distance between tip and the collector	Jet diameter decreases with increasing distance. At short distance, the fibers are not completely stabilized and eventually the cross-sections of spun fiber become flatter and some fibers stick together becoming bundle fiber. At long distance, the fibers exhibit a straight; cylindrical morphology indicates the fiber mostly dried when reaching the collector.	[85, 87]
Concentration	Below critical concentration, the fiber jet will break down due to generation of mixture of fibers and droplets jet. Above the critical concentration, a stable jet is difficult to form. Bimodal distribution of fiber diameters is possible to form from higher concentration solutions. Decreasing concentration will reduce the diameter of electrospun fiber; further decrease will form beaded fibers.	[85, 86, 88]
Viscosity	Too diluted solution is difficult to form a stable jet; the jet will break whereas too viscous solution will make it difficult to form fiber due to the solution drying at the tip. Higher viscosity produces fiber without beads.	[85, 89]
Surface tension of solution	Reduced surface tension will produce fibers without beads. Reduced surface tension will form a larger diameter of the fibers. (Depending on polymer and solvent.)	[89]
Net charge density	Adding NaCl or salts will increase the net charge density and reduce diameter of the fiber.	[88, 89]
Feeding rate	At higher feeding rate, this will exceed the delivery rate of solution with applied voltage and eventually result in tiny drops of jet on the collector. At low feeding rate, the solution is ejected faster and the shift of the mass balance will result in sustained but unstable jet which eventually forms fiber with beads.	[87]
Molecular weight	Molecular weight affects the manipulated concentration in order to electrospin fine fibers. Low molecular weight can easily form nonuniform fibers with bead. High molecular weight will be able to produce uniform fibers without bead.	[88]

the first electrospinning method by Formhals faced some technical disadvantages since it was difficult to completely dry the fibers after electrospinning due to the short distance between the spinning and collection zones, which resulted in a less aggregated web structure [52]. However, after 5 years, Formhals [53] had polished his first work by altering the distance between the nozzle and the collecting device to give more drying time for the electrospun fibers [54] with longer distance.

As concerned, a support material is crucial for fuel cell system, especially on electrospun fiber, in order to maintain its mechanical strength in concurrence with increasing

the performance of the fuel cell system. For instance, Choi et al. [55] conducted an experiment on an electrospun PVDF membrane, impregnated with various amounts of Nafion (0.3–0.5 g), and found that 0.4 g of Nafion is the optimum amount that exhibited higher proton conductivity and lower methanol permeability in DMFC application, compared to unmodified Nafion 115 which had lesser thickness with area of 5 cm × 5 cm. Table 4 shows a review on electrospinning parameters and their effects toward fiber morphology and fiber diameter.

For instance, Pelipenko et al. [54] claimed that the humidity was found to be the most important parameter

TABLE 5: Desired properties for some desired applications of electrospun nanofiber.

Application	Tissue engineering	Filter media	Fuel cell
Material	Poly (D,L-lactide-co-glycolide) (PLGA)	Polyacrylonitrile (PAN)	Sulfonated poly (arylene ether sulfone) (SPAES)
Morphology	Nonwoven, highly porous	Solution with low mass fraction produces beads on fiber and high mass fraction produces smooth and uniform fiber	Clear nanofiber with uniform dense Norland Optical Adhesive (NOA) 63 polymer filled completely the interfiber void of nanofiber
Average diameter (nm)	500–800	270–400	40–160 (at first stage) can increase to 0.73–165 (after compaction/embedded)
Mechanical strength	Higher along with decrease in diameter of fiber	NA	Increased for embedded nanofibers
Controlled parameter	Voltage of 18 kV, 20 mL glass syringe, 18 G needle, 20 cm needle to collector distance, copper collecting plate	5 cm needle to collector distance, humidity controlled chamber in pure N <sub>2</sub> , 25% relative humidity, voltage of 3–10 kV, 400 μm inner diameter capillary	NA rotating drum (horizontally)
Reference	[90]	[91]	[74]

that influenced the electrospinning process. They found that the relative humidity (RH) can affect the diameter of the electrospun nanofibers. Lower RH values can cause a rapid evaporation of the solvent, resulting in thicker nanofiber. Higher RH values can cause slow evaporation of the solvent, resulting in thinner nanofibers.

Other than that, the formation of layer by layer electrospun mat composite fiber can assist the formation of nanofiber mats with a comparable proton conductivity and suppression in methanol permeability of the DMFC system. Previously, Liu et al. [56] conducted an experiment regarding the layer by layer composite electrospun fiber by incorporating sulfonated poly phenylene oxide and poly diallyl dimethyl ammonium chloride (sPPO/PDAC). In their study, they found that, at thickness of  $\sim 25 \mu\text{m}$ , the electrospun fiber mats gave high methanol barrier properties in parallel with higher open circuit voltage of the DMFC system. In addition, the contribution of Nylon electrospun mats had indeed increased the mechanical strength of the layer by layer electrospun fiber sPPO/PDAC membrane.

Controllable hierarchical features such as nonwoven, aligned, or patterned fibres, nanoribbons, nanorods, random 3D structures, submicron spring, and twisted fibers with controlled diameter can also be prepared by modifying the solution and processing parameters and setup geometries [31]. Basically, the production of desirable nanofibers can be affected by many factors, including their application purpose primarily. For biomedical purpose, especially in tissue engineering scaffold, a few requirements had been drawn by Fang et al. [8] in their review in order to produce an electrospun fiber with a great performance. Table 5 lists some of the applications of the electrospun fiber and their desired properties, respectively. The application of electrospun nanofiber had been studied intensively by Huang et al. [2] in their paper. Different polymers with different characteristics were used in the electrospinning process. The polymers, however, have similar characteristics for respective applications.

## 4.2. Collector Geometries of Electrospinning

**4.2.1. Collector Type.** The formation of nanofibers can be classified into woven and nonwoven nanofibers. The type of collector used plays a big role in differentiating those types or nanofiber alignments. The methods utilized in developing aligned woven nanofibers consist of the use of oriented collector, as well as static double grounded collector [30, 44].

*(i) Oriented Collector.* An oriented collector can be divided into two parts, which are rotating drum collector (Figure 5(a)) and rotating disk collector (Figure 5(b)). The rotating drum collector is used for collecting the aligned arrays nanofibers, whereas the rotating disk is used to collect uniaxially aligned nanofibers. The alignment fibers produced via rotating drum correspond to the rotational speed applied on the drum [44]. This type of electrospinning method is more complicated since the speed of the rotation needs to be well controlled to produce nanofibers with fine alignment.

The rotating disk collector can also be used for collecting continuous nanofibers, since nanofiber is highly attracted to the large electrical field applied at the edge of the disk [30]. According to Baji et al. [44], the use of this method can produce aligned nanofibers, even though only a small amount of fiber is produced due to the small area of the disk edge. In addition, Theron et al. [57] used the disk as a collector in producing polyethylene oxide (PEO) nanofibers. They found that the diameter of the electrospun nanofibers was 200 nm in average and the distance between the fibers varied from 1000 nm to 2000 nm due to the occurrence of repelling during reaching the collector. This eventually influenced the morphology of the formed nanofibers. The obtained morphology of the resultant fibers is as shown in Figures 5(a) and 5(b) [44].

*(ii) Double Ground Collector.* This setup is developed by introducing two parallel plates in the electrospinning system

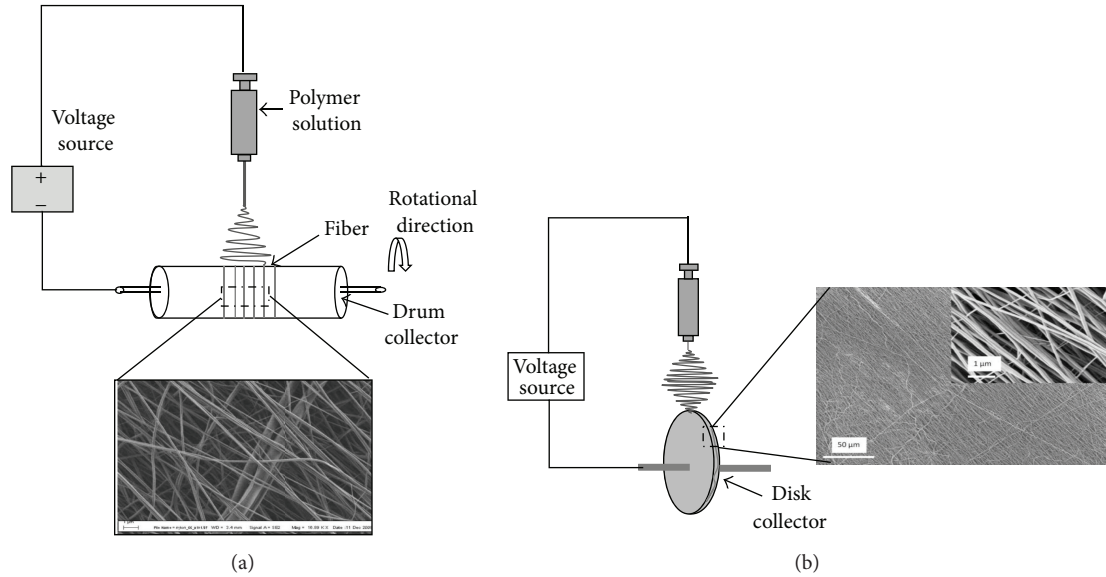


FIGURE 5: Oriented collector of electrospinning (a) rotating drum collector and (b) rotating disk collector [44]. Copyright © 2014 Elsevier B.V.

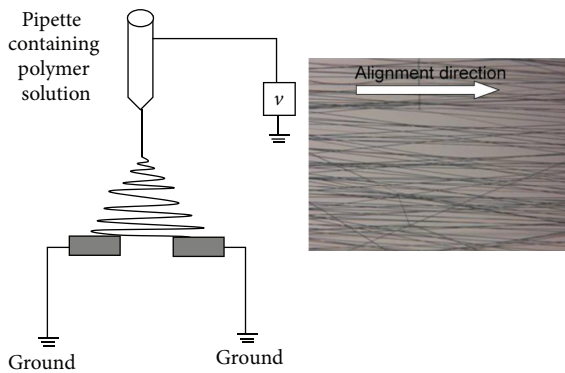


FIGURE 6: Double ground collector [44]. Copyright © 2014 Elsevier B.V.

as a collecting device for woven nanofibers. The fibers exiting the syringe tip tend to “straighten” themselves in the region between the two plates, where a formation of good alignment nanofibers can be obtained, as shown in Figure 6 [30, 44]. Pan et al. [58] in their study on Nafion/poly (vinyl pyrrolidone) (PVP) nanowires (NPNWs) had used the collector, composed of two conductive substrates (silicon) separated by a void gap. They found that the transportation of proton to reach the cathode in NPNWs was easier and high proton conductivity in proportion with reduction in diameter was obtained due to the increase in degree of “texture” resulting from preferential orientation. They revealed that the proton conductivity could be enhanced by altering the diameter of the NPNWs to less than 2300 nm.

Nevertheless, for a randomly oriented nanofiber (nonwoven) used as stationary collector, the collector can be divided into two types, which are vertical flat ground (Figure 7(a)) and horizontal flat ground (Figure 7(b)) collectors. These

types of setup consist of nonpreferable location for the nanofibers to deposited itself. However, these types of setup will make the nanofibers oriented by it and spread randomly on the collector.

The electric field/voltage supply will force the jet solution to twirl around before arriving at the top of the collector, in which, at this point, the gravitational force is negligible for the polymer solution. Rodoplu and Mutlu, [59] claimed that either in vertical or in horizontal direction of the needle, this configuration will still affect the formation of the Taylor cone and the droplet, since at this point the gravity still plays the role. They also claimed that, in vertical direction of the syringe instead of horizontal direction, this configuration will affect the shape of the droplet formation (Taylor cone formation) at the needle tip, which depends on the flat surface of the tip of needle. Kumar [60] conducted an experiment in order to study the effect of the collector type on the electrospun PVA. Four different types of collector were used, such as plane plate collector, drum rotator collector, grid collector, and edge collector. From the experiment, he found that the edge type collector showed a promising result on aligned fibers with good morphological characteristic and no bead was obtained compared with the other types of collector. Thus, this study proved that the collector types give a significant effect on fiber morphology of the electrospun fiber.

**4.2.2. Collector Composition/Substrates.** As the collector is in metal form, the composition or substrates on the collector for fiber collection can be in various forms such as glass, plastic, metal, or silicon wafer. However, the difference between these collector compositions will affect the structure of the electrospun fiber. For instance, Kim et al. [61] proved that the different types of composition used on the collector affected the structure of the poly (L-lactide) (PLLA) and poly

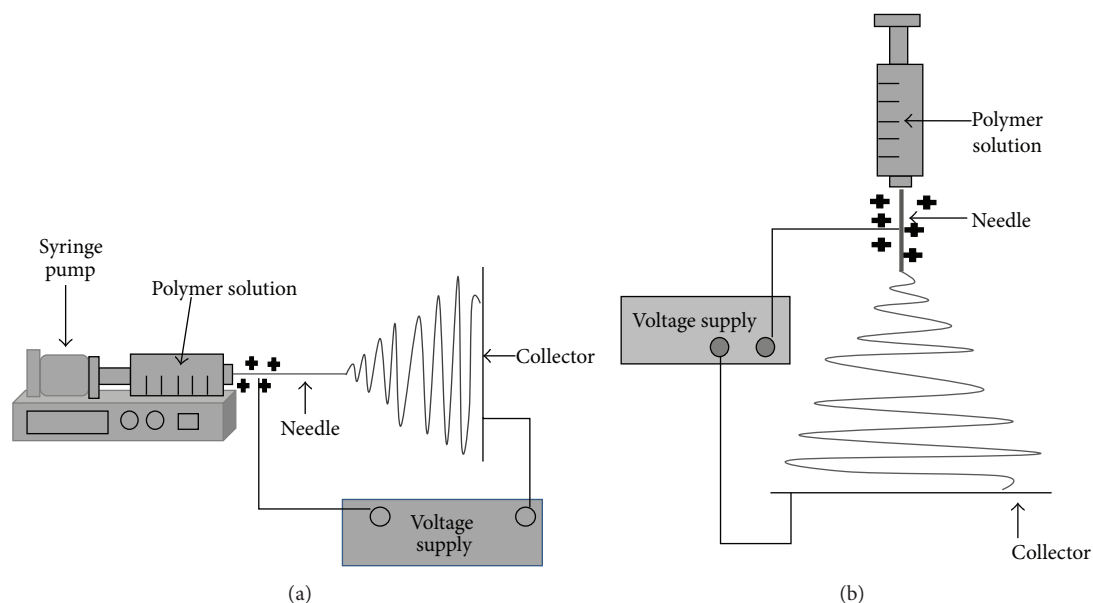


FIGURE 7: Stationary collector of electrospinning (a) horizontal flat ground collector and (b) vertical flat ground collector.

TABLE 6: Effects of collector composition on structure of electrospun fiber [61].

Collector	PLLA	PLA50GA50
Metal	Smooth fiber	Smooth fiber
Water reservoir	—	Shrinkage of nanofibers of hydrophobic polymer
Methanol	Swelling	Large beads formed

(lactide-*co*-glycolide) (PLA50GA50) fibers. In the study, they dissolved the PLA50GA50 in dimethyl formamide (DMF) in order to form the 35 wt. % of the polymer solution, and 6 wt. % of the PLLA solution was prepared by dissolving the PLLA in methylene chloride (MC) and DMF with solvent ratio of 65 : 35. Table 6 shows the structure of electrospun fiber at the collector composition.

Meanwhile, Liu and Hsieh [62] proved that the structure of electrospun cellulose acetate collected via different collector compositions such as copper mesh, aluminum foil, water, and paper will differ due to the influence of the conductivity of the collector itself. Conductive collector will help to dissipate the carried charge by the fibers, whereas the nonconductive collectors cannot help to dissipate the charge carried by the fiber. Eventually, this will result in more porous structure of fibers due to the repelling of fibers against one another. According to the Oxford Dictionary and Thesaurus, a conductive material is defined as the material which has the ability to conduct heat or electricity within itself. Tang et al. [63] used small nail as a collector in their study in order to produce a zigzag or helical structured nanofibers. They proposed that by reducing the area of the collector, the electric field can be concentrated at the nail, eventually producing helical nanofibers (Figure 8).

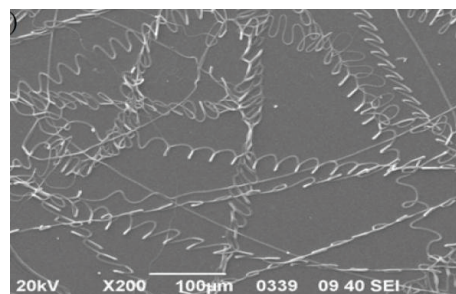


FIGURE 8: SEM image of the curled PVP microfiber electrospun at 40 kV working voltage, at working distance of 10 cm [63]. Copyright<sup>®</sup> Chinese Physical Society.



FIGURE 9: Nanofiber mat of EVOH on human hand [65]. Copyright<sup>®</sup> Elsevier B.V.

In addition, Pham et al. [64] in their review had discussed poly (ethylene-*co*-vinyl alcohol), which was spun directly onto a human hand. They also studied the effect of the collector composition on the structure of the electrospun fiber. The spun fiber on human hand was also experimented by Kenawy et al. [65], in which after 30 minutes, they found

TABLE 7: Standard collector dimension set by NaBond Technologies Co., Limited.

Type of collector	Parameter	Specification
Rotating drum	Speed	150–6000 rpm
	Dimension	$D = 76$ mm, 20 mm, 6 mm; $L = 235$ mm
	Disc collector	$D = 140$ mm, sharp edge or flat edge
Plate	Size	A4, B5, A5
	Dimension	$L = 720$ mm, $W = 540$ mm, $H = 890$ mm

that a thick mat of EVOH was formed, coating a hand, as shown in Figure 9. This human hand is categorized as dielectric materials since it can support electrostatic field, even though this type of materials is a poor electric conductor [65]. The same interpretation goes to plastic petri dish. Thus, a wide range of the fiber formation, with regard to the structure of the fiber, can be obtained using different types of collector composition. Lin and Wang [66] conducted an experiment for producing PVA nanofiber having different thickness,  $\sim 17 \mu\text{m}$ ,  $\sim 29 \mu\text{m}$ , and  $\sim 41 \mu\text{m}$ , by using copper collection roll as a collector. In their study, the impregnated poly (vinyl alcohol) (PVA) nanofiber within the Nafion solution could indeed decrease the thickness of the pristine Nafion thin film up to  $\sim 50 \mu\text{m}$ . Furthermore, the decrease in thickness of the nanocomposite membrane shows an increase in the proton conductivity due to the short pathway from anode to cathode without jeopardizing the methanol barrier properties for DMFC applications.

**4.2.3. Dimension of the Collector.** The dimension of the collector used in electrospinning process generally depends on the function of the nanofiber itself and the type of collector used. Beachley and Wen [67] performed a study on the effect of the size of two parallel plates on the electrospun fiber diameter and length. In the study, they used three different sizes of collector which were  $(30.5 \times 7.5 \times 0.7)$  cm,  $(15 \times 4 \times 0.35)$  cm, and  $(7.5 \times 2 \times 0.15)$  cm, and they found that, as the plate size increased, the fiber diameter also increased, as well as the fiber length. A standard dimension for the rotating drum collector and plate collector can be found from NaBond Technologies Co., Limited. The specification is tabulated in Table 7.

In reality, the collector dimension can be neglected since the formation of the desirable morphology and diameter of fibers rely more on the type of collector. This can be seen from a number of research works, which gave a great attention to the type of collector in order to obtain the desirable fibers. For instance, Buttafoco et al. [68] had used plate collector with ground aluminum foil with  $6 \text{ cm} \times 6 \text{ cm}$  in dimension and rotating collector made of silicon tube with dimension of  $3.1 \text{ mm}$  outer diameter and  $6 \text{ cm}$  in length used in order to produce an electrospun collagen and elastin for tissue engineering applications. The nonwoven and partially

oriented fibers were observed for plate and rotating collector, respectively.

**4.3. Configurations of Nozzle in Electrospinning.** In ejection and needle configuration, there are three main types of nozzle configuration such as single [69], side-by-side [70] and coaxial [59] (Table 8), which have become popular in producing different types of nanofibers, such as nanohollow fiber/core-shell fiber, and nanofiber.

## 5. Application of Electrospun Nanofibers

The unique properties of electrospun nanofibers have made it regain much attention in multiple applications. These unique properties are (1) extremely long length; (2) larger surface area to volume ratio; (3) complex pore size; and (4) alignment on the molecular level (either woven or nonwoven). These characteristics of electrospun nanofiber make it practical in various applications, as shown in Table 9.

## 6. Potential of Electrospun Polymer/Inorganic Nanocomposite Membrane

Even though Nafion exhibits excellent performance as proton exchange membrane, it is still difficult to be prepared as nanofiber structure. Electrospinning process is inapt for Nafion since it is not soluble in most common solvents. Furthermore, this insolubility often results in the formation of micelles, which causes the decrease in chain entanglement and incapability to electrospin fiber without any addition of high molecular weight carrier [21]. Rajesh [71], in his study, had successfully electrospun SPEEK nanofiber with 61% degree of sulfonation, in which he found that the conductivity of electrospun SPEEK membrane was higher compared to cast film SPEEK membrane. These performances were attributed to the increase in surface charge concentration and increase in water uptake, as well as the formation of ion-conducting channels in the membrane matrix.

Chakrabarty et al. [72] prepared electrospun SPEEK (ESPEEK) for electro-dialytic separation application, where they found that the ESPEEK was suitable for electro-dialytic separation of  $\text{Na}^+$  and  $\text{Ca}^{2+}/\text{Mg}^{2+}$ . This happened due to the formation of nanofibrous pore which restricted the migration of bivalent cation across the ESPEEK membrane. Lee et al. [73] produced dense membranes of  $\text{SiO}_2/\text{SPEEK}$  incorporated with Nafion solution for PEMFC application, where they found that the membranes showed excellent proton conductivity compared to the cast Nafion and SPEEK. Meanwhile, Choi et al. [74] studied electrospun nanofiber as a network ion-exchange membrane in fuel cell application. In their study, they found that the combination of sulfonated poly (arylene ether sulfone) (sPAES) electrospun fiber mats with Norland Optical Adhesive (NOA) 63 polymer solution gave an excellent proton conductivity compared to the pristine Nafion.

Figure 10 shows the schematic diagram of composite nanofiber network of an ion exchange membrane. This composite nanofiber network was built by four-step procedure

TABLE 8: Configuration types of electrospinning.

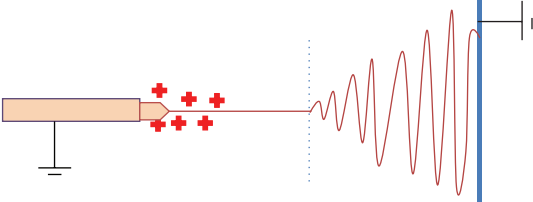
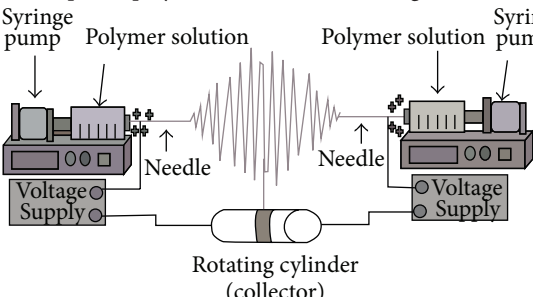
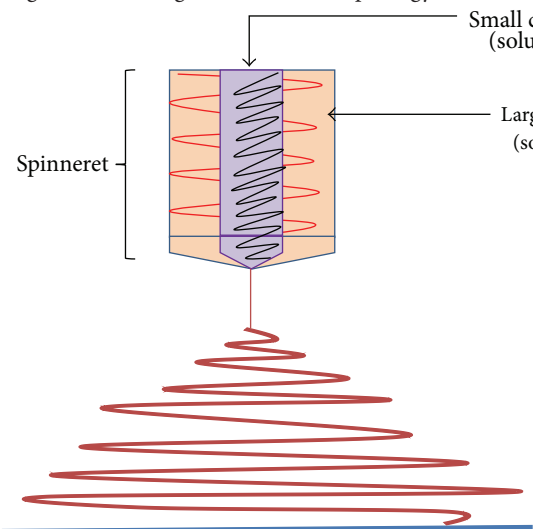
Nozzle configuration	Description
Single	<p>The most common configuration and simplest charged polymer solution will flow through a single capillary. This type of configuration has been used to electrospin single polymer solutions as well as blended polymers [92]</p> 
Side by side	<p>Two separate polymer solutions flow through two different capillaries (set side-by-side) [93]</p> 
Coaxial	<p>This configuration allows simultaneous coaxial electrospinning of two different polymer solutions, where the smaller capillary is placed inside a larger capillary. Small fiber can essentially be encapsulated into a larger fiber, leading to core-shell morphology [94]</p> 

TABLE 9: Function of electrospun nanofibers in various fields of application [8, 30, 31, 38].

Sector	Function of electrospun nanofibers
Biomedical	Tissue engineering scaffolds; wound healing; neural prostheses; artificial heart valve; drug delivery; release control
Environmental protection	Filtration; metal ion adsorption and recovery
Catalyst and enzyme carriers	Catalyst; enzymes
Sensors	
Energy harvest and storage	Solar cells; fuel cells; lithium ions batteries; super capacitors; hydrogen storage; photovoltaics
Others	Gas turbine filter; engine filter; personal protective mask; gas separation

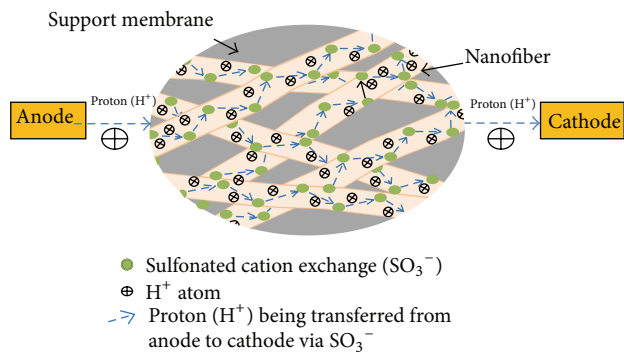


FIGURE 10: Proton transport from anode to cathode within nanofiber network.

as explained by Choi et al. [74]. The figure clearly shows the transportation of proton from anode to cathode by the Grotthuss mechanism or proton hopping. The movement of proton involves a sequence of steps which contribute to the formation and breakage of hydrogen bonding. In Figure 10, the proton hops from one SO<sub>3</sub><sup>-</sup> to another which leads to an effective proton conduction within composite nanofiber network. The presence of inert polymer as a support membrane to fill up the intervoid space between the nanofibers is crucial in order to ensure the stability and mechanical strength for composite nanofiber mat at different operation temperatures and pressure.

Montmorillonite (MMT) and hectorites are the most preferred clays for utilization in industrial applications due to their high cation exchange capacity, high surface area, high surface reactivity, and high barrier properties, compared to other types of clay [75]. Cloisite15A is a type of MMT, known as organoclay, since it is modified from MMT. It is very important as an additive in polymer nanocomposite due to its capability to enhance the compatibility with organic polymers [11]. Neppalli et al. [76] stated that the clay can exhibit a characteristic as a nucleating agent, as well as an obstacle to the polymer mobility. This, however, depends on the clay quantity and the dispersion state of the clay within the polymer matrix.

Impregnation of Cloisite15A into SPEEK membrane had been studied by Jaafar et al. [11]. Unfortunately, the dispersion of the Cloisite15A inside the polymer matrix was not completely exfoliated and the resulting dense membrane was barely enough for proton conductivity performance compared to the pristine Nafion 112 membrane. A solution towards performing good distribution and dispersion of Cloisite15A at nanometer size within the polymer matrix is still needed. Therefore, the introduction of electrospinning technique is believed to be able to help in producing electrospun Cloisite15A having smaller size and consequently avoiding agglomeration.

As has been concerned earlier, compared to the corresponding pure polymer membranes, many polymer-inorganic nanocomposite membranes showed much lower fuel permeability along with similar or improved proton conductivities due to the nanodispersion of layered silicates

throughout polymer matrix. The combination of the flexibility and process ability from the base materials and selectivity and thermal stability of the inorganic fillers was significantly assisted by the good distribution of the inorganic materials. The introduction of fillers within the polymer matrix was found promising in increasing the tortuous effect and winding diffusion pathway for methanol to transfer through the nanocomposite membrane and eventually can reduce the methanol crossover. The complete exfoliation morphology of filler within polymer could further allow more cations to be mobile and available for conduction and simultaneously increase proton conductivity [10]. Based on the findings, it can be concluded that the morphological structure of a polymer-inorganic composite whether it is normal composite, intercalated, or exfoliated will significantly contribute to the performance of the PEM by means of proton conductivity and methanol permeability.

Other than that, the electrospinning process can favor the elongation of the chains and the ordering of the polymer. Wang et al. [77] had proven that the electrospinning process can favor the elongation of the chains and the ordering of the polymer instead of the function of the clay itself. Besides clay impregnation within SPEEK polymer matrix, Li et al. [78] had conducted an experiment regarding the incorporation of silver ion within the polymer matrix via electrospinning process. However, the use of silver ion within the SPEEK polymer was found to be not preferable for DMFC applications. Thus, it can be said that the contribution of electrospinning on many polymers and inorganic clay in processing an excellent membrane indeed gives a high performance of membrane not only in fuel cell, but also in many other applications as well.

## 7. Proton Electrolyte Membrane Electrospun Nanofibers for Fuel Cell Application

A desired proton electrolyte membrane for fuel cell application should comply with its intrinsic properties, especially on proton conductivity and fuel/gas crossover barrier properties. To adhere to these properties, the electrospinning parameters need to be controlled in order to produce excellent electrolyte electrospun nanofibers membrane. Basically, electrospinning parameters depend on the type of polymer used. However, an electrospun nanofiber membrane alone might face a low mechanical strength due to its small diameter and its potentials for defects to occur, which makes the electrospun nanofiber easily break [79]. Thus, a support material is needed in order to maintain the mechanical strength of the electrospun nanofibers, in parallel with the durability of the electrospun nanofibers membrane to withstand elevated temperature and pressure. Table 10 lists some of the previous researches on electrospinning parameters, which were involved in fabricating the electrospun nanofibers for fuel cell application.

Generally, the effects of electrospun fiber on proton conductivity and methanol permeability are mainly due to the formation of ionic alignment during electrospinning,

TABLE 10: Summary of electrospinning parameters on electrospun nanofibers membrane in fuel cell application.

Polymer	Support material	Type of fuel cell	Electrospinning parameters	Remark	Ref.
Polyvinyl alcohol, PVA	Nafion	Direct methanol Fuel cell (DMFC)	Distance from needle to collector: 20 cm Solution flow rate: 1.2 mL/h Voltage potential: 20 kV I.D. needle: 0.8 mm Collector: copper collection roll	More straight and less tortuous effect on Nafion/PVA nanofiber which leads to increase in proton conductivity of the membrane and reduction in membrane crossover with a thickness of $\sim 50 \mu\text{m}$	[66]
SiO <sub>2</sub> /sulfonated poly (ether ether ketone), SPEEK	Nafion	Proton exchange membrane fuel cell (PEMFC)	Distance from needle to collector: 10 cm Voltage potential: 15 kV I.D. needle: 0.15 mm Humidity: below 15% RH	Thickness of SiO <sub>2</sub> /SPEEK nanofiber membrane 45 $\mu\text{m}$ incorporation with Nafion produces high proton conductivity compared to cast Nafion and SPEEK. The maximum power density of SiO <sub>2</sub> /SPEEK incorporation with Nafion is 170 mW/cm <sup>3</sup> double than cast Nafion	[73]
Polyvinyl alcohol, PVA	Nafion	Direct methanol fuel cell (DMFC)	Distance from needle to collector: 25 cm Solution flow rate: 0.5 ml/h Voltage potential: 16 kV	Succeeds in producing PVA nanofiber having diameter of 200–300 nm Contribution of Nafion as support material has indeed increased the mechanical and thermal properties of the composite membrane with thickness of composite membrane at 46–47 $\mu\text{m}$ PVA nanofibers have indeed increased the barrier properties on methanol crossover	[95]
Sulfonated poly (ether sulfone) (SPES)	Nafion	Direct methanol fuel cell (DMFC)	Distance from needle to collector: 15 cm Voltage potential: 19 kV Collector: rotating cylindrical stainless steel	Proton conductivity of the bilayer SPES/Nafion barely changes compared to the Nafion 117/112 The methanol crossover is reduced due to the SPES nanofibers within Nafion matrices	[96]

TABLE 11: Summary of the effect of electrospinning parameters on the performance of fuel cell in terms of proton conductivity and methanol permeability.

Parameter increase	Fiber structure	Proton conductivity	Methanol permeability	Remark on methanol permeability
Voltage applied	Decrease in fiber diameter, thinner fiber	Increases	Decreases	With contribution of filler within the parent polymer matrices
Needle to collector distance	Decrease in fiber diameter	Increases	Decreases	With contribution of filler within the parent polymer matrices
Viscosity of dope solution	Fiber without beads, smooth fiber	Increases	Decreases	With contribution of filler within the parent polymer matrices

as well as the formation of tortuous pathway for methanol to penetrate into the membrane matrices. Furthermore, the contribution of filler within the polymer matrix will improve the barrier properties for methanol crossover. As a conclusion, a small diameter of electrospun fiber with an excellent proton conductivity and higher resistance on fuel/gas permeability can be obtained through the optimization of different parameters of the electrospinning equipment. Table 11 presents some of the effects of electrospinning parameters, such as needle to collector distance, viscosity of the solution, solution flow rate and voltage applied on

the fiber morphology, proton conductivity, and methanol permeability.

## 8. Conclusion and Outlook

The development of electrospun polymer electrolyte membrane for direct methanol fuel cell (DMFC) has gained a lot of attention from researchers due to its capability in sustaining proton conductivity, as well as capability to suppress methanol permeability without jeopardizing the fuel cell system. A significant amount of work has been done for

preparing electrospun sulfonated poly (ether ether ketone) (SPEEK) for fuel cell application, as well as optimizing the degree of sulfonation for spinnable SPEEK solution. However, several existing challenges in electrospinning process still need to be overcome prior to formation of smooth electrospun fiber, such as solution parameters, controlled parameters, and ambient parameters. Despite all the challenges, the electrospinning method for preparing an electrospun SPEEK/Cloisite15A is undeniably potential in enhancing methanol permeability barrier properties, as well as proton conductivity for DMFC.

## Conflict of Interests

The authors declare that there is no conflict of interests regarding the publication of this paper.

## Acknowledgments

The author Hazlina Junoh would like to express gratitude to the Ministry of Science, Technology and Innovation (MOSTI), Malaysia, for the grant with vote number of R.J130000.7842.4S057 for the financial support and also to the Research Management Centre (RMC), UTM, for supporting related research management activities.

## References

- [1] A. Martins, J. V. Araújo, R. L. Reis, and N. M. Neves, "Electrospun nanostructured scaffolds for tissue engineering applications," *Nanomedicine*, vol. 2, no. 6, pp. 929–942, 2007.
- [2] Z.-M. Huang, Y.-Z. Zhang, M. Kotaki, and S. Ramakrishna, "A review on polymer nanofibers by electrospinning and their applications in nanocomposites," *Composites Science and Technology*, vol. 63, no. 15, pp. 2223–2253, 2003.
- [3] R. Dersch, M. Steinhart, U. Boudriot, A. Greiner, and J. H. Wendorff, "Nanoprocessing of polymers: applications in medicine, sensors, catalysis, photonics," *Polymers for Advanced Technologies*, vol. 16, no. 2-3, pp. 276–282, 2005.
- [4] H. T. Chiu, J. M. Lin, T. H. Cheng, and S. Y. Chou, "Fabrication of electrospun polyacrylonitrile ion-exchange membranes for application in lysozym," *Express Polymer Letters*, vol. 5, no. 4, pp. 308–317, 2011.
- [5] S. Kaur, D. Rana, T. Matsuura, S. Sundarrajan, and S. Ramakrishna, "Preparation and characterization of surface modified electrospun membranes for higher filtration flux," *Journal of Membrane Science*, vol. 390-391, pp. 235–242, 2012.
- [6] Z.-G. Wang, L.-S. Wan, Z.-M. Liu, X.-J. Huang, and Z.-K. Xu, "Enzyme immobilization on electrospun polymer nanofibers: an overview," *Journal of Molecular Catalysis B: Enzymatic*, vol. 56, no. 4, pp. 189–195, 2009.
- [7] H. Jia, G. Zhu, B. Vugrinovich, W. Kataphinan, D. H. Reneker, and P. Wang, "Enzyme-carrying polymeric nanofibers prepared via electrospinning for use as unique biocatalysts," *Biotechnology Progress*, vol. 18, no. 5, pp. 1027–1032, 2002.
- [8] J. Fang, X. Wang, and T. Lin, "Functional applications of electrospun nanofibers," in *Nanofibers-Production, Properties and Functional Applications*, pp. 287–326, InTech, 2011.
- [9] Y. I. Tien and K. H. Wei, "Hydrogen bonding and mechanical properties in segmented montmorillonite/polyurethane nanocomposites of different hard segment ratios," *Polymer*, vol. 42, no. 7, pp. 3213–3221, 2001.
- [10] M. Wang and S. Dong, "Enhanced electrochemical properties of nanocomposite polymer electrolyte based on copolymer with exfoliated clays," *Journal of Power Sources*, vol. 170, no. 2, pp. 425–432, 2007.
- [11] J. Jaafar, A. F. Ismail, and T. Matsuura, "Preparation and barrier properties of SPEEK/Cloisite 15A/TAP nanocomposite membrane for DMFC application," *Journal of Membrane Science*, vol. 345, no. 1-2, pp. 119–127, 2009.
- [12] F. Croce, G. B. Appetecchi, L. Persi, and B. Scrosati, "Nanocomposite polymer electrolytes for lithium batteries," *Nature*, vol. 394, no. 6692, pp. 456–458, 1998.
- [13] D. Golodnitsky, G. Ardel, and E. Peled, "Ion-transport phenomena in concentrated PEO-based composite polymer electrolytes," *Solid State Ionics*, vol. 147, no. 1-2, pp. 141–155, 2002.
- [14] A. Kumar and M. Deka, *Advances in Nanocomposites-Synthesis, Characterization and Industrial Applications*, InTech, Vienna, Austria, 2010.
- [15] M. M. Hasani-Sadrabadi, E. Dashtimoghadam, K. Sarikhani, F. S. Majedi, and G. Khanbabaee, "Electrochemical investigation of sulfonated poly (ether ether ketone)/clay nanocomposite membranes for moderate temperature fuel cell applications," *Journal of Power Sources*, vol. 195, pp. 2450–2456, 2010.
- [16] S. Bian, *A Study of the Material Properties of Silicone Nanocomposites Developed by Electrospinning*, University of Waterloo, Waterloo, Canada, 2013.
- [17] S. Mekhilef, R. Saidur, and A. Safari, "Comparative study of different fuel cell technologies," *Renewable and Sustainable Energy Reviews*, vol. 16, no. 1, pp. 981–989, 2012.
- [18] L. Zhang, S.-R. Chae, Z. Hendren, J.-S. Park, and M. R. Wiesner, "Recent advances in proton exchange membranes for fuel cell applications," *Chemical Engineering Journal*, vol. 204-205, pp. 87–97, 2012.
- [19] G. G. Kumar and K. S. Nahm, "Polymer nanocomposites-fuel cell applications," in *Advances in Nanocomposite-Synthesis, Characterization and Industrial Applications*, pp. 639–660, InTech Europe, Vienna, Austria, 2011.
- [20] S. M. J. Zaidi, "Preparation and characterization of composite membranes using blends of SPEEK/PBI with boron phosphate," *Electrochimica Acta*, vol. 50, no. 24, pp. 4771–4777, 2005.
- [21] M. W. Cason, "Electrospun nafion nanofibers for proton exchange membranes," *Literature Seminar*, 2010.
- [22] S. S. Mohtar, A. F. Ismail, and T. Matsuura, "Preparation and characterization of SPEEK/MMT-STA composite membrane for DMFC application," *Journal of Membrane Science*, vol. 371, no. 1-2, pp. 10–19, 2011.
- [23] L. Li, J. Zhang, and Y. Wang, "Sulfonated poly(ether ether ketone) membranes for direct methanol fuel cell," *Journal of Membrane Science*, vol. 226, no. 1-2, pp. 159–167, 2003.
- [24] J.-M. Thomassin, C. Pagnouille, G. Caldarella, A. Germain, and R. Jérôme, "Contribution of nanoclays to the barrier properties of a model proton exchange membrane for fuel cell application," *Journal of Membrane Science*, vol. 270, no. 1-2, pp. 50–56, 2006.
- [25] D. W. Litchfield and D. G. Baird, "The rheology of high aspect ratio nano-particle filled liquids," *Rheology Reviews*, pp. 1–60, 2006.
- [26] A. H. M. Yusof, M. A. M. Amin, A. F. Ismail, M. N. Anam, and N. A. N. Mahmud, "Fabrication and effect of sulfonated poly (ether ether ketone) with Cloisite15A nanoclays for microbial fuel cell application," *International Journal of Sustainable Construction Engineering & Technology*, vol. 4, no. 1, pp. 63–74, 2013.

- [27] R. Jiang, H. R. Kunz, and J. M. Fenton, "Investigation of membrane property and fuel cell behavior with sulfonated poly(ether ether ketone) electrolyte: temperature and relative humidity effects," *Journal of Power Sources*, vol. 150, no. 1-2, pp. 120–128, 2005.
- [28] Y.-H. Su, Y.-L. Liu, Y.-M. Sun et al., "Proton exchange membranes modified with sulfonated silica nanoparticles for direct methanol fuel cells," *Journal of Membrane Science*, vol. 296, no. 1-2, pp. 21–28, 2007.
- [29] R. Gosalawit, S. Chirachanchai, S. Shishatskiy, and S. P. Nunes, "Sulfonated montmorillonite/sulfonated poly(ether ether ketone) (SMMT/SPEEK) nanocomposite membrane for direct methanol fuel cells (DMFCs)," *Journal of Membrane Science*, vol. 323, no. 2, pp. 337–346, 2008.
- [30] B. P. Sautther, *Continuous Polymer Nanofibers Using Electrospinning*, NSF-REU Summer Program, Chicago, Ill, USA, 2005.
- [31] S. Cavaliere, S. Subianto, I. Savych, D. J. Jones, and J. Rozière, "Electrospinning: designed architectures for energy conversion and storage devices," *Energy and Environmental Science*, vol. 4, no. 12, pp. 4761–4785, 2011.
- [32] C. Feng, K. C. Khulbe, and T. Matsuura, "Recent progress in the preparation, characterization, and applications of nanofibers and nanofiber membranes via electrospinning/interfacial polymerization," *Journal of Applied Polymer Science*, vol. 115, no. 2, pp. 756–776, 2010.
- [33] P. Lu and B. Ding, "Applications of electrospun fibers," *Recent Patents on Nanotechnology*, vol. 2, no. 3, pp. 169–182, 2008.
- [34] I. S. Chronakis, "Novel nanocomposites and nanoceramics based on polymer nanofibers using electrospinning process—a review," *Journal of Materials Processing Technology*, vol. 167, no. 2-3, pp. 283–293, 2005.
- [35] A. Frenot and I. S. Chronakis, "Polymer nanofibers assembled by electrospinning," *Current Opinion in Colloid and Interface Science*, vol. 8, no. 1-2, pp. 64–75, 2003.
- [36] X. Xiong, Q. Li, X.-C. Zhang, L. Wang, Z.-X. Guo, and J. Yu, "Poly(vinylidene fluoride)/silica nanocomposite membranes by electrospinning," *Journal of Applied Polymer Science*, vol. 129, no. 3, pp. 1089–1095, 2013.
- [37] D. Zhang, A. B. Karki, D. Rutman et al., "Electrospun polyacrylonitrile nanocomposite fibers reinforced with  $\text{Fe}_3\text{O}_4$  nanoparticles: fabrication and property analysis," *Polymer*, vol. 50, no. 17, pp. 4189–4198, 2009.
- [38] V. Thavasi, G. Singh, and S. Ramakrishna, "Electrospun nanofibers in energy and environmental applications," *Energy and Environmental Science*, vol. 1, no. 2, pp. 205–221, 2008.
- [39] A. Zucchelli, D. Fabiani, C. Gualandi, and M. L. Focarete, "An innovative and versatile approach to design highly porous, patterned, nanofibrous polymeric materials," *Journal of Materials Science*, vol. 44, no. 18, pp. 4969–4975, 2009.
- [40] J. Bajáková, J. Chaloupek, D. Lukáš, and M. Lacarin, "Drawing—the production of individual nanofibers by experimental method," in *Proceedings of the 3rd International Conference on Nanotechnology-Smart Materials (NANOCON '11)*, Bern, Switzerland, 2011.
- [41] C. R. Martin, "Membrane-based synthesis of nanomaterials," *Chemistry of Materials*, vol. 8, no. 8, pp. 1739–1746, 1996.
- [42] A. Greiner and J. H. Wendorff, "Electrospinning: a fascinating method for the preparation of ultrathin fibers," *Angewandte Chemie International Edition*, vol. 46, no. 30, pp. 5670–5703, 2007.
- [43] Y. Liu, J.-H. He, J.-Y. Yu, and H.-M. Zeng, "Controlling numbers and sizes of beads in electrospun nanofibers," *Polymer International*, vol. 57, no. 4, pp. 632–636, 2008.
- [44] A. Baji, Y.-W. Mai, S.-C. Wong, M. Abtahi, and P. Chen, "Electrospinning of polymer nanofibers: effects on oriented morphology, structures and tensile properties," *Composites Science and Technology*, vol. 70, no. 5, pp. 703–718, 2010.
- [45] M. Bogwitzki, W. Czado, T. Frese et al., "Nanostructured fibers via electrospinning," *Advanced Materials*, vol. 13, pp. 70–72, 2001.
- [46] P. Uttayarat, A. Perets, M. Li et al., "Micropatterning of three-dimensional electrospun polyurethane vascular grafts," *Acta Biomaterialia*, vol. 6, no. 11, pp. 4229–4237, 2010.
- [47] D. Li and Y. Xia, "Electrospinning of nanofibers: reinventing the wheel?" *Advanced Materials*, vol. 16, no. 14, pp. 1151–1170, 2004.
- [48] M. AbdElmoula, *Optical, Electrical and Catalytic Properties of Titania Nanotubes*, Northeastern University, Boston, Mass, USA, 2011.
- [49] M. Maleki, M. Latifi, and M. Amani-Tehran, "Optimizing electrospinning parameters for finest diameter of nano fibers," *World Academy of Science, Engineering and Technology*, vol. 64, pp. 389–392, 2010.
- [50] Z. Li and C. Wang, *One Dimensional Nanostructures Electrospinning Technique and Unique Nanofibers*, Springer, New York, NY, USA, 2013.
- [51] C. J. Thompson, G. G. Chase, A. L. Yarin, and D. H. Reneker, "Effects of parameters on nanofiber diameter determined from electrospinning model," *Polymer*, vol. 48, no. 23, pp. 6913–6922, 2007.
- [52] T. Subbiah, G. S. Bhat, R. W. Tock, S. Parameswaran, and S. S. Ramkumar, "Electrospinning of nanofibers," *Journal of Applied Polymer Science*, vol. 96, no. 2, pp. 557–569, 2005.
- [53] A. Formhals, "Method and apparatus for spinning," United States Patent Office, 2,160,962, 1939.
- [54] J. Pelipenko, J. Kristl, B. Janković, S. Baumgartner, and P. Kocbek, "The impact of relative humidity during electrospinning on the morphology and mechanical properties of nanofibers," *International Journal of Pharmaceutics*, vol. 456, no. 1, pp. 125–134, 2013.
- [55] S. W. Choi, Y.-Z. Fu, Y. R. Ahn, S. M. Jo, and A. Manthiram, "Nafion-impregnated electrospun polyvinylidene fluoride composite membranes for direct methanol fuel cells," *Journal of Power Sources*, vol. 180, no. 1, pp. 167–171, 2008.
- [56] D. S. Liu, M. M. Mannarino, G. C. Rutledge, and P. T. Hammond, "Mechanical and transport properties of layer-by-layer electrospun composite proton exchange membranes for fuel cell applications," *ACS Applied Materials & Interfaces*, vol. 5, pp. 8155–8164, 2013.
- [57] A. Theron, E. Zussman, and A. L. Yarin, "Electrostatic field-assisted alignment of electrospun nanofibres," *Nanotechnology*, vol. 12, no. 3, pp. 384–390, 2001.
- [58] C. Pan, H. Wu, C. Wang et al., "Nanowire-based high-performance "Micro Fuel Cells": one-nanowire, one fuel cell," *Advanced Materials*, vol. 20, no. 9, pp. 1644–1648, 2008.
- [59] D. Rodoplu and M. Mutlu, "Effects of electrospinning setup and process parameters on nanofiber morphology intended for the modification of quartz crystal microbalance surfaces," *Journal of Engineered Fibers and Fabrics*, vol. 7, no. 2, pp. 118–123, 2012.
- [60] P. Kumar, *Effect of Collector on Electrospinning to Fabricate Aligned Nanofiber*, National Institute of Technology, Rourkela, India, 2012.
- [61] H. S. Kim, K. Kim, H. J. Jin, and I.-J. Chin, "Morphological characterization of electrospun nano-fibrous membranes of biodegradable poly(L-lactide) and poly(lactide-co-glycolide)," *Macromolecular Symposia*, vol. 224, pp. 145–154, 2005.

- [62] H. Liu and Y.-L. Hsieh, "Ultrafine fibrous cellulose membranes from electrospinning of cellulose acetate," *Journal of Polymer Science B: Polymer Physics*, vol. 40, no. 18, pp. 2119–2129, 2002.
- [63] C.-C. Tang, J.-C. Chen, Y.-Z. Long, H.-X. Yin, B. Sun, and H.-D. Zhang, "Preparation of curled microfibers by electrospinning with tip collector," *Chinese Physics Letters*, vol. 28, no. 5, Article ID 056801, 2011.
- [64] Q. P. Pham, U. Sharma, and A. G. Mikos, "Electrospinning of polymeric nanofibers for tissue engineering applications: a review," *Tissue Engineering*, vol. 12, no. 5, pp. 1197–1211, 2006.
- [65] E.-R. Kenawy, J. M. Layman, J. R. Watkins et al., "Electrospinning of poly(ethylene-co-vinyl alcohol) fibers," *Biomaterials*, vol. 24, no. 6, pp. 907–913, 2003.
- [66] H.-L. Lin and S.-H. Wang, "Nafion/poly(vinyl alcohol) nanofiber composite and Nafion/poly(vinyl alcohol) blend membranes for direct methanol fuel cells," *Journal of Membrane Science*, vol. 452, pp. 253–262, 2014.
- [67] V. Beachley and X. Wen, "Effect of electrospinning parameters on the nanofiber diameter and length," *Materials Science and Engineering C*, vol. 29, no. 3, pp. 663–668, 2009.
- [68] L. Buttafoco, N. G. Kolkman, P. Engbers-Buijtenhuijs et al., "Electrospinning of collagen and elastin for tissue engineering applications," *Biomaterials*, vol. 27, no. 5, pp. 724–734, 2006.
- [69] N. Zhu and X. Chen, *Advances in Biomaterials Science and Biomedical Applications*, InTech, Hampshire, UK, 2013.
- [70] F. Li, Y. Zhao, and Y. Song, *Nano Channel and Capsule by Coaxial Electrospinning Nanofiber*, InTech, 2010.
- [71] K. P. Rajesh, *Studies on Ion Conducting Properties of Electrospun Polymer Fibers*, Indian Institute of Technology Madras, Chennai, India, 2011.
- [72] T. Chakrabarty, M. Kumar, K. P. Rajesh, V. K. Shahi, and T. S. Natarajan, "Nano-fibrous sulfonated poly(ether ether ketone) membrane for selective electro-transport of ions," *Separation and Purification Technology*, vol. 75, no. 2, pp. 174–182, 2010.
- [73] C. Lee, S. M. Jo, J. Choi et al., "SiO<sub>2</sub>/sulfonated poly ether ether ketone (SPEEK) composite nanofiber mat supported proton exchange membranes for fuel cells," *Journal of Materials Science*, vol. 48, no. 10, pp. 3665–3671, 2013.
- [74] J. Choi, K. M. Lee, R. Wycisk, P. N. Pintauro, and P. T. Mather, "Nanofiber network ion-exchange membranes," *Macromolecules*, vol. 41, no. 13, pp. 4569–4572, 2008.
- [75] J. Jaafar, A. F. Ismail, T. Matsuura, and K. Nagai, "Performance of SPEEK based polymer-nanoclay inorganic membrane for DMFC," *Journal of Membrane Science*, vol. 382, no. 1-2, pp. 202–211, 2011.
- [76] R. Neppalli, S. Wanjale, M. Birajdar, and V. Causin, "The effect of clay and of electrospinning on the polymorphism, structure and morphology of poly(vinylidene fluoride)," *European Polymer Journal*, vol. 49, no. 1, pp. 90–99, 2013.
- [77] Y. Wang, M. Li, J. Rong et al., "Enhanced orientation of PEO polymer chains induced by nanoclays in electrospun PEO/clay composite nanofibers," *Colloid and Polymer Science*, vol. 291, no. 6, pp. 1541–1546, 2013.
- [78] X. Li, X. Hao, and H. Na, "Preparation of nanosilver particles into sulfonated poly(ether ether ketone) (S-PEEK) nanostructures by electrospinning," *Materials Letters*, vol. 61, no. 2, pp. 421–426, 2007.
- [79] S. Zhnag, *Mechanical and Physical Properties of Electrospun Nanofibers*, North Carolina State University, 2009.
- [80] L. Du, X. Yan, G. He, X. Wu, Z. Hu, and Y. Wang, "SPEEK proton exchange membranes modified with silica sulfuric acid nanoparticles," *International Journal of Hydrogen Energy*, vol. 37, no. 16, pp. 11853–11861, 2012.
- [81] S. M. J. Zaidi, S. D. Mikhailenko, G. P. Robertson, M. D. Guiver, and S. Kaliaguine, "Proton conducting composite membranes from polyether ether ketone and heteropolyacids for fuel cell applications," *Journal of Membrane Science*, vol. 173, no. 1, pp. 17–34, 2000.
- [82] M.-K. Song, S.-B. Park, Y.-T. Kim, and H.-W. Rhee, "Nanocomposite polymer membrane based on cation exchange polymer and nano-dispersed clay sheets," *Molecular Crystals and Liquid Crystals*, vol. 407, no. 15–23, pp. 411–419, 2003.
- [83] M.-K. Song, S.-B. Park, Y.-T. Kim, K.-H. Kim, S.-K. Min, and H.-W. Rhee, "Characterization of polymer-layered silicate nanocomposite membranes for direct methanol fuel cells," *Electrochimica Acta*, vol. 50, no. 2-3, pp. 639–643, 2004.
- [84] P. Bébin, M. Caravanier, and H. Galiano, "Nafion/clay-SO<sub>3</sub>H membrane for proton exchange membrane fuel cell application," *Journal of Membrane Science*, vol. 278, no. 1-2, pp. 35–42, 2006.
- [85] J. Doshi and D. H. Reneker, "Electrospinning process and applications of electrospun fibers," *Journal of Electrostatics*, vol. 35, no. 2-3, pp. 151–160, 1995.
- [86] J. M. Deitzel, J. Kleinmeyer, D. Harris, and N. C. Beck Tan, "The effect of processing variables on the morphology of electrospun nanofibers and textiles," *Polymer*, vol. 42, no. 1, pp. 261–272, 2001.
- [87] R. Jalili, S. A. Hosseini, and M. Morshed, "The effects of operating parameters on the morphology of electrospun polyacrylonitrile nanofibres," *Iranian Polymer Journal*, vol. 14, no. 12, pp. 1074–1081, 2005.
- [88] S.-H. Tan, R. Inai, M. Kotaki, and S. Ramakrishna, "Systematic parameter study for ultra-fine fiber fabrication via electrospinning process," *Polymer*, vol. 46, no. 16, pp. 6128–6134, 2005.
- [89] H. Fong, I. Chun, and D. H. Reneker, "Beaded nanofibers formed during electrospinning," *Polymer*, vol. 40, no. 16, pp. 4585–4592, 1999.
- [90] W.-J. Li, C. T. Laurencin, E. J. Caterson, R. S. Tuan, and F. K. Ko, "Electrospun nanofibrous structure: a novel scaffold for tissue engineering," *Journal of Biomedical Materials Research*, vol. 60, no. 4, pp. 613–621, 2002.
- [91] K. M. Yun, C. J. Hogan Jr., Y. Matsubayashi, M. Kawabe, F. Iskandar, and K. Okuyama, "Nanoparticle filtration by electrospun polymer fibers," *Chemical Engineering Science*, vol. 62, no. 17, pp. 4751–4759, 2007.
- [92] F. Abdel-Hady, A. Alzahrany, and M. Hamed, "Experimental validation of upward electrospinning process," *ISRN Nanotechnology*, vol. 2011, Article ID 851317, 14 pages, 2011.
- [93] F. Xu, L. Li, and X. Cui, "Fabrication of aligned side-by-side TiO<sub>2</sub>/SnO<sub>2</sub> nanofibers via dual-opposite-spinneret electrospinning," *Journal of Nanomaterials*, vol. 2012, Article ID 575926, 5 pages, 2012.
- [94] T. J. Sill and H. A. von Recum, "Electrospinning: applications in drug delivery and tissue engineering," *Biomaterials*, vol. 29, no. 13, pp. 1989–2006, 2008.
- [95] S. Mollá and V. Compañ, "Polyvinyl alcohol nanofiber reinforced Nafion membranes for fuel cell applications," *Journal of Membrane Science*, vol. 372, no. 1-2, pp. 191–200, 2011.
- [96] I. Shabani, M. M. Hasani-Sadrabadi, V. Haddadi-Asl, and M. Soleimani, "Nanofiber-based polyelectrolytes as novel membranes for fuel cell applications," *Journal of Membrane Science*, vol. 368, no. 1-2, pp. 233–240, 2011.

## Research Article

# Effects of Different Doping Ratio of Cu Doped CdS on QDSCs Performance

Xiaojun Zhu, Xiaoping Zou, and Hongquan Zhou

*Beijing Key Laboratory for Sensor, Ministry-of-Education Key Laboratory for Modern Measurement and Control Technology and School of Applied Sciences, Beijing Information Science and Technology University, Jianxiangqiao Campus, Beijing 100101, China*

Correspondence should be addressed to Xiaoping Zou; xpzou2005@gmail.com

Received 13 June 2014; Accepted 16 October 2014

Academic Editor: Jin H. Kim

Copyright © 2015 Xiaojun Zhu et al. This is an open access article distributed under the Creative Commons Attribution License, which permits unrestricted use, distribution, and reproduction in any medium, provided the original work is properly cited.

We use the successive ionic layer adsorption and reaction (SILAR) method for the preparation of quantum dot sensitized solar cells, to improve the performance of solar cells by doping quantum dots. We tested the UV-Vis absorption spectrum of undoped CdS QDSCs and Cu doped CdS QDSCs with different doping ratios. The doping ratios of copper were 1:100, 1:500, and 1:1000, respectively. The experimental results show that, under the same SILAR cycle number, Cu doped CdS quantum dot sensitized solar cells have higher open circuit voltage, short circuit current density photoelectric conversion efficiency than undoped CdS quantum dots sensitized solar cells. Refinement of Cu doping ratio are 1:10, 1:100, 1:200, 1:500, and 1:1000. When the proportion of Cu and CdS is 1:10, all the parameters of the QDSCs reach the minimum value, and, with the decrease of the proportion, the short circuit current density, open circuit voltage, and the photoelectric conversion efficiency are all increased. When proportion is 1:500, all parameters reach the maximum values. While with further reduction of the doping ratio of Cu, the parameters of QDSCs have a decline tendency. The results showed that, in a certain range, the lower the doping ratio of Cu, the better the performance of quantum dot sensitized solar cell.

## 1. Introduction

Due to rapid growth in the world economy, energy problems have considerable attention in the past several decades [1]. To provide energy alternatives, researchers have been developing renewable energies including solar, nuclear, wind, and biopower [2]. Among these alternatives, solar-to-electric energy conversion systems have always been a fascinating and challenging frontier for science and application [1–3].

Quantum dot sensitized solar cells (QDSCs) are gaining attention as they show promise toward the development of next generation solar cells [4–8]. The design of QDSCs which is similar to that of dye sensitized solar cell (DSSC) includes deposition of narrow bandgap semiconductor nanocrystal such as CdSe on mesoscopic TiO<sub>2</sub> films [9]. Although the photocurrent achieved from QDSCs is comparable to that of DSSCs, the observed power conversion efficiency remains quite low because of the low open circuit potential as well as low fill factor [10]. We use the successive ionic layer adsorption and reaction (SILAR) method for the preparation

of quantum dot sensitized solar cell to improve the performance of solar cells by doping quantum dots. We tested the UV-Vis absorption spectrum of undoped CdS QDSCs and Cu doped CdS QDSCs with different doping ratios. The doping ratios of copper were 1:100, 1:500, and 1:1000. The experimental results show that, under the same SILAR cycle number, Cu doped CdS quantum dot sensitized solar cells have higher open circuit voltage, short circuit current density, and photoelectric conversion efficiency than undoped CdS quantum dots sensitized solar cells.

With the aid of research, we describe a method for improving CdS QDSCs efficiency. The results showed that, in a certain range, the lower the doping ratio of Cu is, the better the performance of quantum dot sensitized solar cell is.

## 2. Experimental Detail

**2.1. Material and Preparation.** Chemicals were purchased and used as received. We need 0.1M Cd(NO<sub>3</sub>)<sub>2</sub> ethanol solution and CuCl<sub>2</sub> and 0.1M Na<sub>2</sub>S methanol solution.

TABLE 1: ICP-OES test data of Cu doped CdS quantum dots.

Sample	Cd ( $\mu\text{g}$ )	Cu ( $\mu\text{g}$ )	Cd ( $10^{-6}$ mol)	Cu ( $10^{-6}$ mol)	The molar ratio of copper
Cu-CdS	512	8.043	4.555	0.127	2.788%

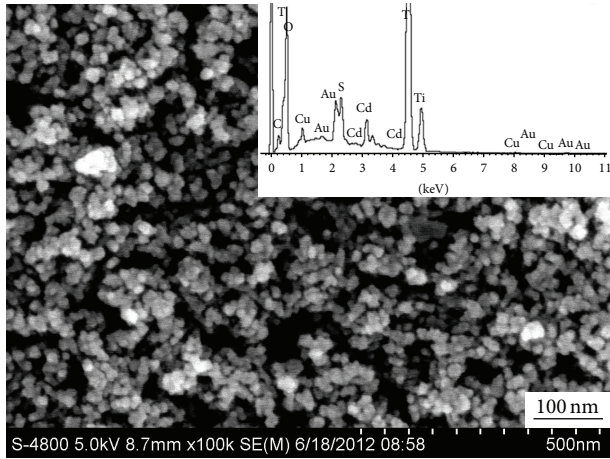


FIGURE 1: The SEM image of Cu doped CdS quantum dots photoanode; illustration is the EDS spectrum.

The mixed solution includes doping substances and the main precursor; the SILAR method was used to deposit the doped quantum dots.

**2.2. Measurements.** We added  $\text{CuCl}_2$  into 0.1 M  $\text{Cd}(\text{NO}_3)_2$  ethanol solution as the cation precursor solution, and used 0.1 M  $\text{Na}_2\text{S}$  methanol solution as the anion precursor solution. Then we prepared the Cu doped CdS quantum dots by SILAR method. Doping ratio mentioned in this paper refers to the molar ratio of impurity atoms and Cd atoms in solution preparation, such that the doping ratio of Cu to Cd is 1:100 which refers to the  $\text{CuCl}_2$  material  $\text{Cu}(\text{NO}_3)_2$  molar ratio of 1:100, and the deposition method is consistent with specific deposition method for CdS quantum dots.

### 3. Results and Discussion

Figure 1 shows the copper-doped-CdS photoanode SEM image, and the upper right corner of the image block is the corresponding EDS patterns of samples, the copper doping ratio for 1:100, SILAR, for 4 times. From the chart component analysis, we can clearly see that copper has been successfully doped into the CdS quantum dot optical anode. But because the CdS quantum dot size is very small, we cannot see the size of CdS in this graph. As for the morphology of CdS quantum dots, it can be seen in Figure 1, and we will not go into here.

In order to more accurately determine the copper that has been doped into the CdS quantum dots, we conducted inductively coupled plasma atomic emission spectrometry (ICP-OES) test, and the proportion of copper doped here is 1:500, as shown in Table 1.

In Table 1, the first part is the performance parameters of Cd and Cu, and the second part is the molar parameters

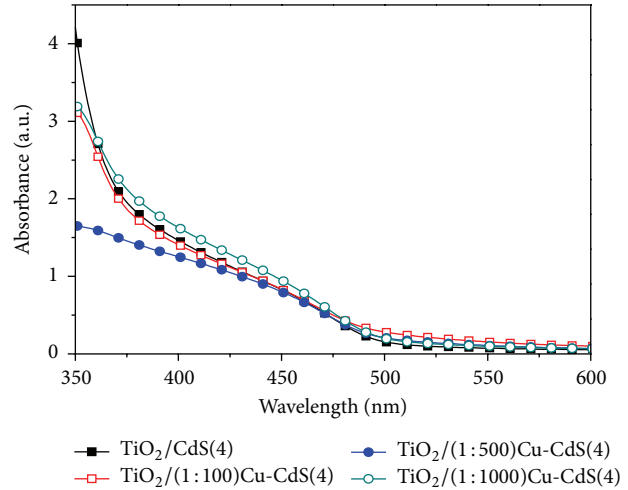


FIGURE 2: The UV-Vis absorption spectra of Cu doped CdS and undoped CdS with different doping ratio of copper.

of Cd and Cu and the molar ratio of Cu in the CdS. As it can be seen from the table, the molar ratio of copper in prepared solution is 0.2%, but the molar ratio of copper deposition after the share rose to 2.788%, and the content of copper in solid sample increases is nearly 14 times higher than the copper content in the precursor solution. This maybe because, relative to the cadmium ion, copper ion easily reacted with sulfide ion and increased the content of copper and cadmium content decreased.

For the performance of the system of Cu doped CdS QDSCs, the effects of doping ratio change CdS properties of QDSCs copper. The UV-V is absorption spectra of Cu doped CdS quantum dots and undoped CdS quantum dots with different doping ratios of copper; they were 1:100, 1:500, and 1:1000, respectively (Figure 2).

As can be seen from the Figure 2, the absorption spectra of 1:500 (Cu: Cd) molar ratio of Cu doped CdS quantum dots little blue-shift comparing with that of undoped CdS quantum dots and the difference among the three absorption spectra of Cu doped CdS quantum dots with different doping ratios is not very significant. The exciton absorption peak is probably around 440 nm. This may be because the three doping ratios are not much different, consistency in their UV-Vis absorption spectrum is relatively high, and the exciton absorption peaks are almost similar to each other. We should use other ways to represent the characteristics of Cu doped CdS quantum dot sensitized solar cell.

The  $J$ - $V$  curves of undoped CdS QDSCs and doped-CdS QDSCs with Cu doping ratio is 1:500 (Figure 3). Table 2 is the performance parameters of the corresponding quantum dot sensitized solar cells.

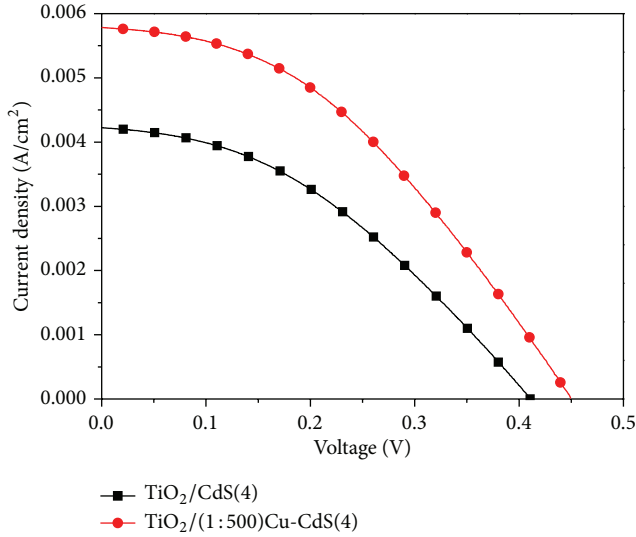


FIGURE 3: The  $J$ - $V$  curves of undoped CdS QDSCs and Cu doped CdS QDSCs.

TABLE 2: The parameters of undoped CdS and Cu doped CdS QDSCs.

Sample	$J_{sc}$ (mA/cm <sup>2</sup> )	$V_{oc}$ (mV)	FF	$\eta$ (%)
TiO <sub>2</sub> /CdS(4)	4.28	412	0.39	0.67
TiO <sub>2</sub> /(1:500)Cu-CdS(4)	5.79	451	0.40	1.04

From Figure 3 and Table 2, it can be seen that, in the same SILAR cycle number, Cu doped CdS quantum dot sensitized solar cell has higher open circuit voltage, short circuit current density, and photoelectric conversion efficiency than undoped CdS quantum dots sensitized solar cell. The reason for this result is that the doping of Cu improves the conduction band of CdS quantum dots [11] and assists the photogenerated electron to transport to TiO<sub>2</sub>. What is more is that the incorporation of Cu can also improve the adsorption spectra of CdS quantum dots on TiO<sub>2</sub> photoanode surface, inhibiting the generation of dark current, finally improving all the parameters of the QDSCs. Figure 4. Energy level diagrams of doped and undoped TiO<sub>2</sub>/CdS QDSCs. From the chart we can intuitively see changes in energy level.

The above contents analyzed  $J$ - $V$  curves of the doped and undoped quantum dot sensitized solar cell, and we will discuss the influence of Cu doping ratio on the quantum dot sensitized solar cell. Figure 5 shows the  $J$ - $V$  curves of different doping ratio of Cu doped CdS QDSCs. Table 3 shows the corresponding parameters of QDSCs.

As can be seen from the charts, when the doping ratio of Cu is 1:10, QDSC's parameters are close to zero. And then with the decrease of the doping ratio, the short circuit current density, the open circuit voltage, and the photoelectric conversion efficiency increase. When the doping ratio is 1:500, all the parameters reach the maximum value. While with further decrease in the proportion of Cu doping, all the parameters of the QDSCs have a decline tendency.

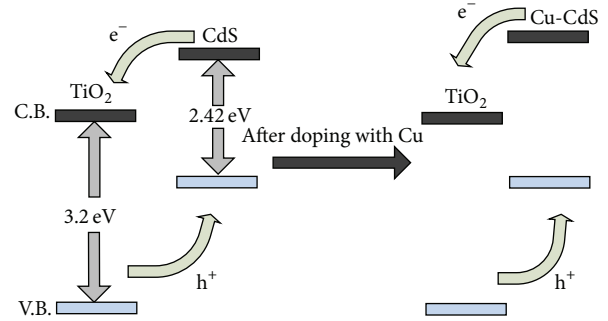


FIGURE 4: Energy level diagrams of doped and undoped TiO<sub>2</sub>/CdS.

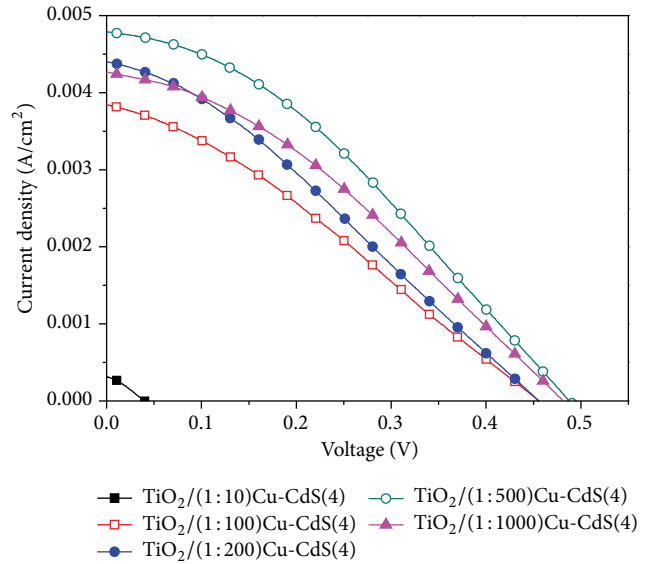


FIGURE 5: The  $J$ - $V$  curves of different doping ratio of Cu doped CdS QDSCs.

TABLE 3: The parameters of different doping ratio of Cu doped CdS QDSCs.

Doping ratio	$J_{sc}$ (mA/cm <sup>2</sup> )	$V_{oc}$ (mV)	FF	$\eta$ (%)
TiO <sub>2</sub> /(1:10)Cu-CdS(4)	0.32	40	0.31	0.004
TiO <sub>2</sub> /(1:100)Cu-CdS(4)	3.85	457	0.29	0.51
TiO <sub>2</sub> /(1:200)Cu-CdS(4)	4.40	455	0.30	0.60
TiO <sub>2</sub> /(1:500)Cu-CdS(4)	4.79	488	0.35	0.81
TiO <sub>2</sub> /(1:1000)Cu-CdS(4)	4.26	482	0.34	0.69

## 4. Conclusion

The doping ratio of Cu is 1:10. And then it decreases the doping ratio, and the short circuit current density, the open circuit voltage, and the photoelectric conversion efficiency increase. When the doping ratio is 1:500, all the parameters reach the maximum value. While with further decrease in the proportion of Cu doping, all the parameters of the QDSCs have a decline tendency. The results show that, in a certain

range, the lower the doping ratio of Cu, the better the performance of quantum dot sensitized solar cell.

### Conflict of Interests

The authors declare that there is no conflict of interests regarding the publication of this paper.

### Acknowledgments

This work was partially supported by Key Project of Beijing Natural Science Foundation (3131001), Key Project of Natural Science Foundation of China (91233201 and 61376057), Key Project of Beijing Education Committee Science & Technology Plan (KZ201211232040), State 863 Plan of MOST of PR China (2011AA050527), Beijing National Laboratory for Molecular Sciences (BNLMS2012-21), State Key Laboratory of Solid State Microstructures of Nanjing University (M27019), State Key Laboratory for New Ceramic and Fine Processing of Tsinghua University (KF1210), Key Laboratory for Renewable Energy and Gas Hydrate of Chinese Academy of Sciences (y207ka1001), Beijing Key Laboratory for Sensors of BISTU (KF20141077207 and KF20141077208), and Beijing Key Laboratory for photoelectrical measurement of BISTU (GDKF2013005).

### References

- [1] B. O'Regan and M. Graetzel, "Low-cost, high-efficiency solar cell based on dye-sensitized colloidal TiO<sub>2</sub> films," *Nature*, vol. 353, no. 6346, pp. 737–740, 1991.
- [2] P. V. Kamat, "Meeting the clean energy demand: nanostructure architectures for solar energy conversion," *Journal of Physical Chemistry C*, vol. 111, no. 7, pp. 2834–2860, 2007.
- [3] J. Y. Kim, K. Lee, N. E. Coates et al., "Efficient tandem polymer solar cells fabricated by all-solution processing," *Science*, vol. 317, no. 5835, pp. 222–225, 2007.
- [4] P. V. Kamat, K. Tvrđy, D. R. Baker, and J. G. Radich, "Beyond photovoltaics: semiconductor nanoarchitectures for liquid-junction solar cells," *Chemical Reviews*, vol. 110, no. 11, pp. 6664–6688, 2010.
- [5] P. V. Kamat, "Quantum dot solar cells. Semiconductor nanocrystals as light harvesters," *The Journal of Physical Chemistry C*, vol. 112, no. 48, pp. 18737–18753, 2008.
- [6] I. Mora-Seró and J. Bisquert, "Breakthroughs in the development of semiconductor-sensitized solar cells," *Journal of Physical Chemistry Letters*, vol. 1, no. 20, pp. 3046–3052, 2010.
- [7] G. Hodes, "Comparison of dye- and semiconductor-sensitized porous nanocrystalline liquid junction solar cells," *Journal of Physical Chemistry C*, vol. 112, no. 46, pp. 17778–17787, 2008.
- [8] I. J. Kramer and E. H. Sargent, "Colloidal quantum dot photovoltaics: a path forward," *ACS Nano*, vol. 5, no. 11, pp. 8506–8514, 2011.
- [9] J. G. Rowley, B. H. Farnum, S. Ardo, and G. J. Meyer, "Iodide chemistry in dye-sensitized solar cells: making and breaking I-I bonds for solar energy conversion," *Journal of Physical Chemistry Letters*, vol. 1, no. 20, pp. 3132–3140, 2010.
- [10] P. K. Santra and P. V. Kamat, "Mn-doped quantum dot sensitized solar cells: a strategy to boost efficiency over 5%," *Journal of the American Chemical Society*, vol. 134, no. 5, pp. 2508–2511, 2012.
- [11] M. Wei and Y. Li, "A method of improving the performance of quantum dot sensitized solar cell," China Patent, 201010608155.5, 2011.

## Research Article

# Characterization of Carbon Nanotube/Graphene on Carbon Cloth as an Electrode for Air-Cathode Microbial Fuel Cells

Hung-Yin Tsai,<sup>1</sup> Wei-Hsuan Hsu,<sup>2</sup> and Ying-Chen Huang<sup>1</sup>

<sup>1</sup>Department of Power Mechanical Engineering, National Tsing Hua University, Hsinchu 30013, Taiwan

<sup>2</sup>Department of Mechanical Engineering, National United University, Miaoli 36003, Taiwan

Correspondence should be addressed to Hung-Yin Tsai; [hytsai@pme.nthu.edu.tw](mailto:hytsai@pme.nthu.edu.tw)

Received 29 August 2014; Revised 26 November 2014; Accepted 24 December 2014

Academic Editor: Jin H. Kim

Copyright © 2015 Hung-Yin Tsai et al. This is an open access article distributed under the Creative Commons Attribution License, which permits unrestricted use, distribution, and reproduction in any medium, provided the original work is properly cited.

Microbial fuel cells (MFCs), which can generate low-pollution power through microbial decomposition, have become a potentially important technology with applications in environmental protection and energy recovery. The electrode materials used in MFCs are crucial determinants of their capacity to generate electricity. In this study, we investigate the performance of using carbon nanotube (CNT) and graphene-modified carbon-cloth electrodes in a single-chamber MFC. We develop a process for fabricating carbon-based modified electrodes and *Escherichia coli* HB101 in an air-cathode MFC. The results show that the power density of MFCs can be improved by applying a coat of either graphene or CNT to a carbon-cloth electrode, and the graphene-modified electrode exhibits superior performance. In addition, the enhanced performance of anodic modification by CNT or graphene was greater than that of cathodic modification. The internal resistance decreased from 377 k $\Omega$  for normal electrodes to 5.6 k $\Omega$  for both electrodes modified by graphene with a cathodic catalyst. Using the modified electrodes in air-cathode MFCs can enhance the performance of power generation and reduce the associated costs.

## 1. Introduction

In the last decade, due to the lack of energy and the rise of environmental awareness, scientists and researchers have been looking for some more alternative energies with renewability and low pollution. Microbial fuel cells (MFCs) are an excellent potential technology that converts the energy, released by breaking chemical bonds of organic compounds, into electrical energy through catalytic reactions of microorganisms under anaerobic conditions. The concept of using microorganisms as catalysts in fuel cells was explored in the 1910s [1, 2]. At that time, fuel cell technology was neither mature nor taken seriously since Potter's MFC could merely produce weak power. Until the energy crisis and the breakthrough in fuel cell technology, the performance of MFC is improved gradually and taken seriously.

A typical MFC system consists of two chambers, anode and cathode, separated by proton exchange membrane (PEM). MFC can convert chemical energy directly into electrical one by the way that the microorganisms oxidize

the substrate to produce electrons ( $e^-$ ) and protons ( $H^+$ ) in the anode chamber. Electrons, collected on the anode, are transported to cathode by external circuit while protons are transferred internally to the cathode chamber through the membrane. Then electrons and protons reacted with oxygen and form water. According to the anodic oxidation and cathodic reduction, this promoted the electrons in the anode and the cathode to move and generate the battery current [3–7]. In order to obtain higher current, the microbes must effectively decompose organisms so that electrons can be transferred easily. The microorganisms attached on the anode surface allow electrons to transfer smoothly to the anode. To better bacteria attachment on the anode, many studies utilized the porous carbon materials as anodic ones, such as carbon mesh, carbon paper, carbon cloth, and graphite brush [8–15].

In the year 2004, Liu et al. investigated the performance of single-chamber MFC in wastewater treatment [16]. The structure consists of both cathode and anode electrodes placed in a single reaction chamber with PEM directly fused

to the surface of the cathode. Later in the same year, Liu and Logan further studied the performances of air-cathode single-chamber MFC in the presence and in the absence of PEM, respectively; their study demonstrated the possibility of using MFC systems without the cost of PEM materials [17]. Furthermore, the air-cathode design allows oxygen to pass through the cathode directly and thus reduces the cost to establish air exposure equipments. This design of single-chamber MFC has several advantages over the traditional double-chamber MFCs.

The performance of a MFC is affected by several factors including the microbial inoculation, electrode materials, ionic concentration, catalyst, internal resistance, and electrode spacing [18–21]. The electrode materials play an important role in the electricity generation. To improve the power generation of MFC, many researchers have focused on material modification and upgrade microbe’s inoculation.

Carbon nanotubes (CNTs) have many excellent properties such as nanometer size, good electronic conductivity, high surface area, and excellent structure and stability. Some studies show that CNT can enhance microbial fuel cell performance [22, 23]. Recently, researchers and scientists were much interested in graphene, whose existence had been objectively verified with abundant potential applications. Graphene is the world’s thinnest and most rigid nanomaterial and has excellent electronic transition [24]. These unique characteristics (high surface area, low resistance, desirable mechanical strength, transparency, etc.) can be compatibly put in use for various fields such as solar cell [25, 26], touchscreens, and supercapacitors [27].

In this study, a set of mediatorless single-chamber MFCs were designed to examine the performance which resulted from different carbon cloth electrodes on which CNTs or graphenes were coated to form a highly conductive electrode with a high specific surface area. In order to evaluate the property and the performance of CNT/graphene modified MFCs, the power density and the internal resistance are compared for different electrodes with or without the presence of Pt catalyst or modified anodes.

## 2. Materials and Methods

**2.1. Preparation of Electrodes.** Commercial MWCNTs (Multi-walled Carbon Nanotubes) or graphenes of 20 mg were added to 95% ethanol of 10 mL, which was sonicated to disperse the CNTs/graphenes for one hour. This resulted in a stable and uniformly dispersed slurry of MWCNTs or graphenes. A carbon cloth was soaked into the MWCNT/graphene solution for one hour, removed, and then baked at 150°C for one hour to eliminate residual water. This resulted in a thick, black coating of MWCNTs/graphene on the carbon cloth’s surface.

For all experiments, the base material of anode was nonwet proofed carbon cloth (W0S1002, CeTech Co., Ltd, Taiwan) while that of cathode was wet proofed carbon cloth (W1S1005, CeTech Co., Ltd, Taiwan). Some of the cathode carbon cloth contained a platinum catalyst ( $0.5 \text{ mg cm}^{-2}$ , 20 wt% Pt).

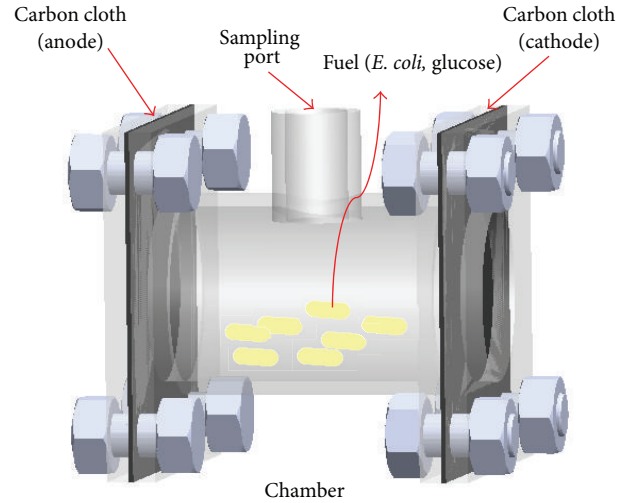


FIGURE 1: The schematic of air-cathode MFC used in the current study. The PMMA chamber was designed as the air-cathode single-chamber MFC. Use different types of carbon cloth (modified or unmodified) as electrode and connect them with external resistance with copper wires. Use glucose as fuel and *Escherichia coli* as anode’s catalyst.

TABLE 1: Electrode conditions of the MFCs in the current study.

Experimental cases	Electrode	
	Anode	Cathode
MFC-NN	Normal	Normal
MFC-GN	Graphene	Normal
MFC-CN	CNT	Normal
MFC-NP	Normal	Pt
MFC-GP	Graphene	Pt
MFC-CP	CNT	Pt
MFC-NGP	Normal	Graphene + Pt
MFC-GGP	Graphene	Graphene + Pt
MFC-NCP	Normal	CNT + Pt
MFC-CCP	CNT	CNT + Pt

**2.2. MFC Design.** Figure 1 shows the air-cathode MFC used in the current study, which is the same as reported earlier [13]. The single-chamber MFC is fabricated from polymethyl methacrylate (PMMA). The shape of the single-chamber MFC is cylinder, whose diameter, length, and wall thickness are 5 cm, 6 cm, and 0.5 cm, respectively. A cathode electrode was fixed to the air-side, and an anode electrode was fixed to the opposite of the chamber. Therefore, reactor volume is approximately 75 mL, and the surface area of cathode and anode is approximately  $12.57 \text{ cm}^2$ . Copper wire was used to connect the circuit ( $1000 \Omega$  resistor except when stated otherwise).

In this study, ten different types of single-chamber MFCs were constructed to compare the performances of the MFCs as shown in Table 1. In order to distinguish different types of reactors, we name these groups with notation. The first letter represents the anodic condition; the second and third

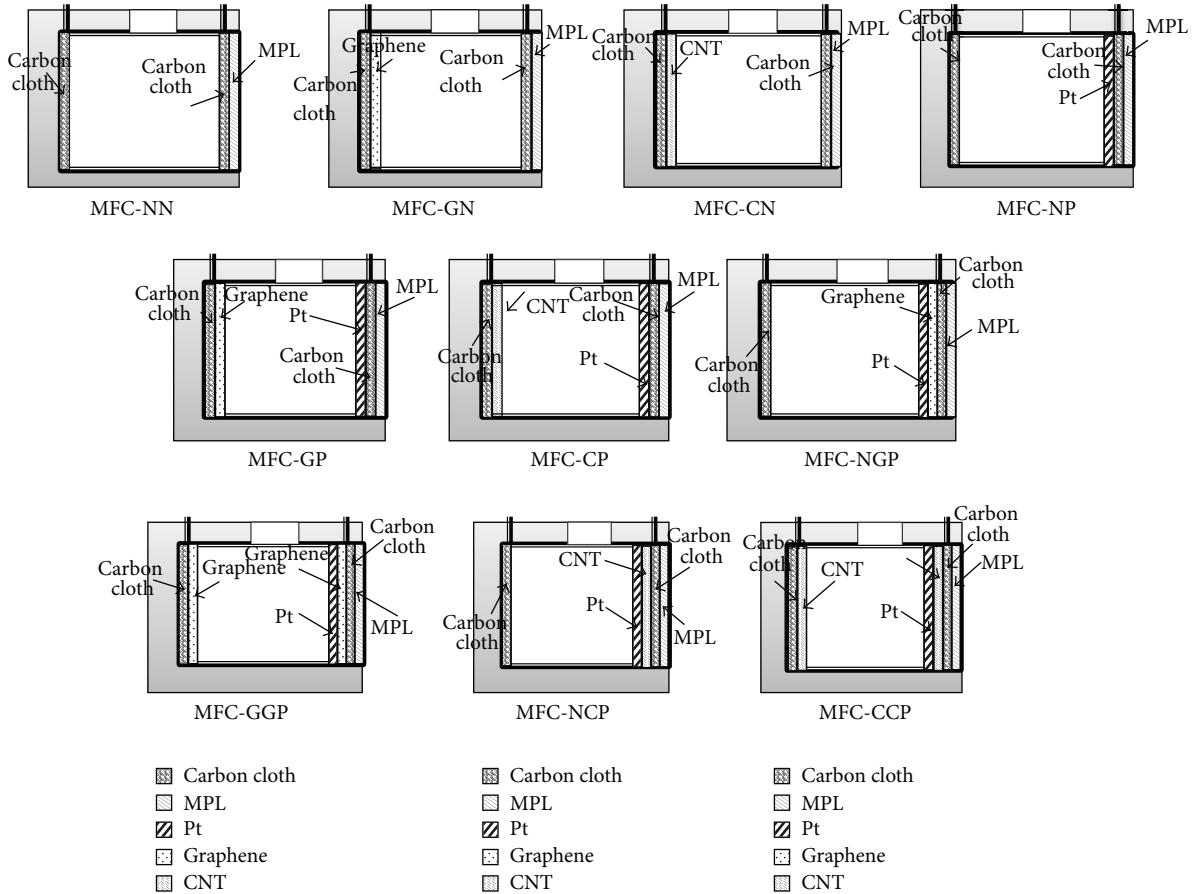


FIGURE 2: Schematic diagrams of electrode conditions for different MFCs.

letters represent the cathodic condition. N represents the normal carbon cloth; G represents the carbon cloth modified by graphene; C represents the carbon cloth modified by CNT; and P represents the cathode with platinum catalyst. Figure 2 illustrated the structures of different types of MFCs used in the experiment.

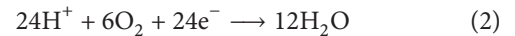
**2.3. Microorganisms and Electrode Reactions.** *Escherichia coli* (*E. coli*) HB101 was grown anaerobically in the atmosphere of  $N_2$  gas for 40 h to the stationary phase in LB medium ( $10\text{ gL}^{-1}$  tryptone,  $5\text{ gL}^{-1}$  yeast extract, and  $10\text{ gL}^{-1}$  NaCl) at  $37^\circ\text{C}$ . The residual cells were obtained at  $4^\circ\text{C}$  by centrifugation at 5,000 rpm and then dissolved in M9 medium ( $6.78\text{ gL}^{-1}$   $\text{Na}_2\text{HPO}_4$ ,  $3\text{ gL}^{-1}$   $\text{KH}_2\text{PO}_4$ ,  $0.5\text{ gL}^{-1}$  NaCl,  $1\text{ gL}^{-1}$   $\text{NH}_4\text{Cl}$ , and  $4\text{ gL}^{-1}$   $\text{C}_6\text{H}_{12}\text{O}_6$ ). The chamber was refilled with *E. coli* solution and inoculated for about two weeks to reach a steady state. MFCs were operated in a temperature controlled room at  $30^\circ\text{C}$ .

In this study, the MFC is based on the biocatalysis of *Escherichia coli* (*E. coli* HB101) and glucose is used as the fuel for MFC. The reaction equations at the anode and cathode are described as follows.

At the anode,



At the cathode,



In the anodic compartment, glucose is oxidized anaerobically by *E. coli*. The glucose loses the electrons and produces hydrogen ions. The electrons can transfer to the cathode via an external circuit and the hydrogen ions can go through the cathode electrode to the air cathode at the same time. After a complete reaction of MFC system, electricity and water can be produced.

**2.4. Measurement and Calculations.** Cell voltage was recorded using a multimeter and a data acquisition system (CHY-48R). Power density  $P$  ( $\text{Wm}^{-2}$ ) in MFC tests was calculated according to the equation  $P = IV/A$ , where  $I$  (A) is the current,  $V$  (V) is the voltage, and  $A$  ( $\text{m}^2$ ) is the projected cross-sectional area of the anode.

In the fuel cell field, the polarization curve is the most commonly used method to evaluate the performance of power generation. The polarization curve is to describe the relationship between the voltage and the current. *E. coli*, as the microbe for further power generation, was placed in the tank culture for two weeks when the voltage became stable and changed the external resistance. When the voltage output became stable, data started to be recorded to determine

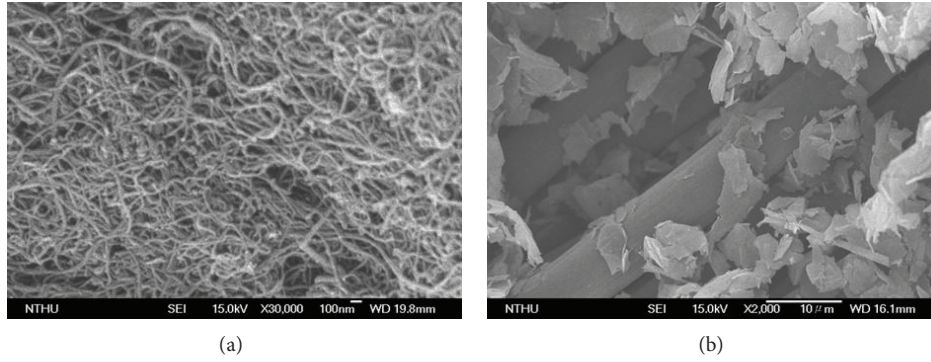


FIGURE 3: SEM images of carbon nanotube (a) and graphene (b) on the carbon cloth.

the voltage and power generation sustained across a range of current densities obtained by varying the resistance between the electrodes. To obtain the polarization curve and power density curve as a function of current, external circuit resistances were varied from 1 to 20 M $\Omega$ . In this study, the polarization slope method was used to calculate the cell's internal resistance. For the Ohm polarization area, the MFCs system has linear relationship between voltage and current. The internal resistance ( $R_{in}$ ,  $\Omega$ ) within the microbial fuel cell was calculated as

$$R_{in} = \frac{\Delta V}{\Delta I}, \quad (3)$$

where  $\Delta V$  and  $\Delta I$  are the voltage difference (mV) and the current difference (mA) between two points, respectively.

### 3. Results and Discussion

The purpose of these experiments was to assess the difference of the MFC power density with different anode structures composed of CNT, graphene, or none on the associated conditions of the cathode.

**3.1. Morphology of CNT and Graphene.** Figures 3(a) and 3(b) show the SEM images of MWCNTs and graphene coated on the carbon cloth, respectively. CNTs were curl and divergence-free in the surface of the carbon cloth. Besides, both CNTs and graphene were uniformly distributed on the carbon cloth based on the current treatment methods to approach the original objective for improving the specific surface area of the electrode. According to the specific surface area of graphene and CNT, the active electrochemical area of graphene-coated electrode is about 2 times more than one of CNT-coated electrode.

**3.2. Polarization and Power Density.** In order to understand the performance effect of the anode with different coating materials, three kinds of anodes with the plain cloth cathodes (the case of MFC-NN, MFC-CN, and MFC-GN) were studied. The power density results of MFCs are shown in Figure 4, in which solid circles represent the power density and hollow circles represent the cell voltage. In addition,

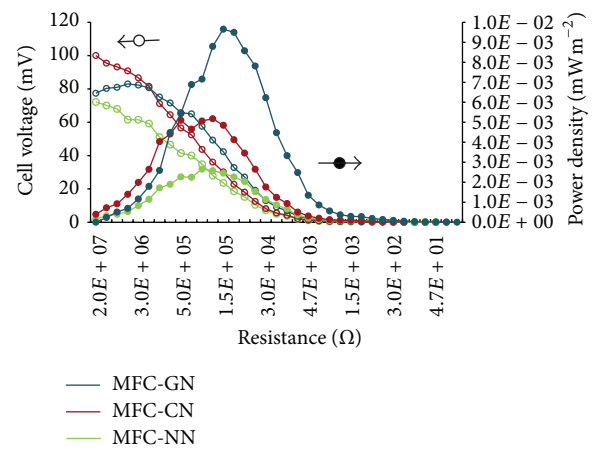


FIGURE 4: Performance diagram for the cases of the anode coated by different materials with the plain cloth cathode only.

the power density of MFC-GN is about 3.5 times more than MFC-NN while MFC-CN is about 1.5 times more than MFC-NN. All the three MFC systems show the same trend that the cell voltage decreases with the decreasing resistance. Typically, a polarization curve can be divided into three regions: activation polarization at high current density, concentration polarization at low current density, and ohmic polarization in the intermediate linear region [28]. The maximum power density of the three cases occurred in ohmic polarization region. In the case of MFC-NN, the maximum power density is  $2.66 \mu\text{W}/\text{m}^2$ . After coating the anodes with CNTs (MFC-CN), the maximum power density is increased to  $5.18 \mu\text{W}/\text{m}^2$ . If CNTs are replaced with a graphene as a coating material, the power density can be further increased to  $9.66 \mu\text{W}/\text{m}^2$  (MFC-GN). From the results, the power density increases greatly with the decreasing of resistance and has the maximum value of  $9.7 \mu\text{W}/\text{m}^2$  for the case of the carbon cloth anode coated with graphenes. Coating nanomaterials as graphenes or MWCNTs onto the anode of MFC can increase the surface area and hence improve the electron transfer route.

From Figure 5, MFC-GGP and MFC-NGP with platinum and graphene on the carbon cloth cathode were different in

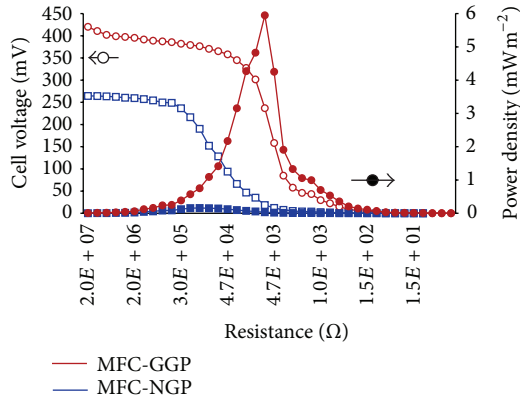


FIGURE 5: Performance diagram for the cases of the anode coated with graphenes or not and with platinum and graphenes coated on the cloth cathode.

the anodic treatment (with graphene or not). The maximum power density of MFC-NGP and MFC-GGP is  $159 \mu\text{W m}^{-2}$  and  $5.9 \text{mW m}^{-2}$ , respectively, with mutual difference about 37 times. These results showed that adding graphenes on the anode can enhance the power generation. The reason could be that the graphene not only increased the surface area that provided bacteria with more space for adhesion but also enhanced the conductivity. The contribution of graphenes coated onto the anode had a similar effect as that shown in Figure 4.

As shown in Figure 6, MFC-CCP and MFC-NCP with platinum and CNT on the carbon cloth cathode were different in the anodic treatment (with CNT or not). The maximum power density of MFC-NCP and MFC-CCP is  $90.5 \mu\text{W m}^{-2}$  and  $378 \mu\text{W m}^{-2}$ , respectively. The power density obtained by MFC-CCP is about 4 times that obtained by MFC-NCP with the anode without CNT. The MFCs with graphene/CNT coated onto the electrode can significantly improve the power density. The anode modified by graphene or CNT was expected to provide *E. coli* with more space to attach and grow. From the results obtained by Zhu et al. [29], surface modifications of anode materials are important for enhancing power generation of microbial fuel cell.

As shown in Figure 7, the polarization curves all had the same trend. The MFC-NP maximum power density was  $51 \mu\text{W m}^{-2}$  while that of MFC-NN was merely  $2.25 \mu\text{W m}^{-2}$ , which showed that the two power densities differed by over 20 times. Furthermore, adding the cathode platinum catalyst can effectively enhance the performance. After coating the cathode with CNT and using a cathodic catalyst, the maximal power density is increased to  $90.5 \mu\text{W m}^{-2}$  (MFC-NCP). If CNTs are replaced with a graphene as a coating material, the power density can be further increased to  $159 \mu\text{W m}^{-2}$  (MFC-NGP). The power density obtained by MFC-NGP is about 3.1 times more than that obtained by MFC-NP and that obtained by MFC-NGP is about 1.8 times more than that obtained by MFC-NP. The experimental results demonstrate that the kinetic rate of the reaction is changed by the catalyst in cathode. Moreover, adding CNTs or graphene on

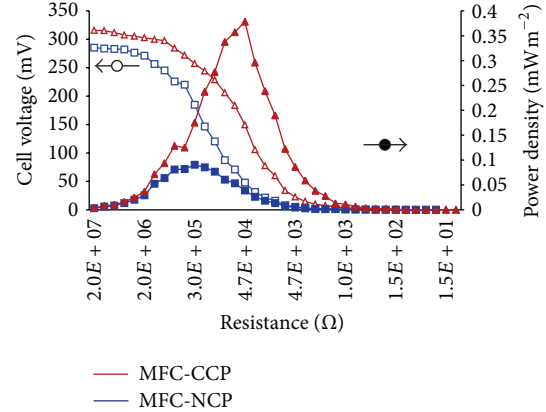


FIGURE 6: Performance diagram for the cases of the anode coated with CNTs or not and with platinum and CNTs coated on the cloth cathode.

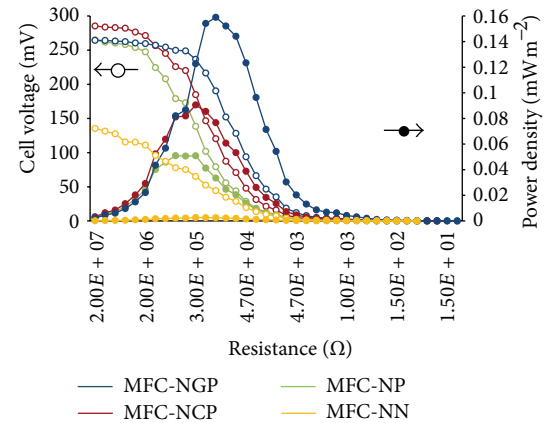


FIGURE 7: Performance diagram for the cases of the cathode coated with different materials and the plain cloth anode only.

the cathode can not only effectively enlarge the surface area but also enhance the reaction rate. The improvement in cathode catalyst performance was realized by coating of CNTs or graphene. Therefore, the improvement in the performance allows the reduction of expenditure on high cost Pt catalyst.

Among all the experimental results, graphene modified electrodes showed better performance on the power generation than CNT modified ones no matter whether graphene is on the anode or on the cathode. The possible reason was because that graphene had better electrical conductivity property and broader surface area than CNT. Since the length of *E. coli* is about  $1 \mu\text{m}$ , the obtained three-dimensional structure stacked by random orientations of graphenes could result in more space for the microbe to adhere than that by CNTs. That is, surface roughness of the accumulated CNTs was relatively smaller than that of the accumulated graphenes for the dimensional level of *E. coli*.

**3.3. Internal Resistance.** Based on the experimental data, the internal resistance can be calculated by polarization slop method as the results shown in Table 2.

TABLE 2: Internal resistances of MFCs for different experiments.

Experimental cases	$R_{in}$ (k $\Omega$ )
MFC-NN	377
MFC-GN	154
MFC-CN	215
MFC-NP	367
MFC-GP	17
MFC-CP	32
MFC-NGP	153
MFC-GGP	5.6
MFC-NCP	326
MFC-CCP	46

For the anodic modification, the internal resistance was reduced from 377 k $\Omega$  for both the normal electrodes (MFC-NN) to 215 k $\Omega$  (MFC-CN) and 154 k $\Omega$  (MFC-GN) when the anode was modified by CNTs and graphene, respectively. Moreover, the internal resistance was significantly reduced from 367 k $\Omega$  for both normal electrodes with cathodic catalyst (MFC-NP) to 32 k $\Omega$  (MFC-CP) and 17 k $\Omega$  (MFC-GP) when the anode was modified by CNTs and graphene with cathodic catalyst, respectively.

For the cathodic modification, the internal resistance was slightly reduced from 367 k $\Omega$  (MFC-NP) to 326 k $\Omega$  for the case of cathode modified by CNTs (MFC-NCP) and largely decreased to 153 k $\Omega$  for the case of cathode modified by graphene (MFC-NGP). For the MFC systems with anode modified by graphene and cathodic catalyst, the internal resistance was reduced from 17 k $\Omega$  (MFC-GP) to about one-third (5.6 k $\Omega$ ) while the cathode was further modified by graphene (MFC-GGP). In addition, MFC systems with the modified electrodes by graphene showed higher power density and lower internal resistance than those by CNTs for the same electrode conditions. Furthermore, the anodic modification by CNTs or graphene showed higher effect on the performance than the cathodic modification did.

Overall, the internal resistance was tremendously reduced from 377 k $\Omega$  (MFC-NN) to 5.6 k $\Omega$  (MFC-GGP). Compared to the similar electrode conditions except the modified carbon-based materials, the internal resistance was tremendously decreased from 367 k $\Omega$  (MFC-NP) to 5.6 k $\Omega$  (MFC-GGP). To sum up, the low internal resistance effect after the electrodes were modified by CNTs or graphene was the proof that CNT and graphene had such excellent electrical conductivity so as to improve the efficiency of electron transmission and hence higher power density.

#### 4. Conclusions

Membrane free air-cathode microbial fuel cells (MFCs) were constructed using different types of composite electrodes, with or without CNT/graphene modified carbon cloth. From the experimental results of the MFC performance, the addition of CNT and graphene enhanced the power density and reduced the internal resistance. The electrodes modified by graphene showed better performance on the power density

and lower internal resistance than those modified by CNTs did. The surface roughness of the accumulated CNTs was relatively smaller than that of the accumulated graphenes at the dimensional level of *E. coli* and the obtained three-dimensional structure stacked by random orientations of graphenes could result in more space for the microbe to attach than that by CNTs since the length of *E. coli* was about 1  $\mu$ m. The internal resistance was significantly reduced from 377 k $\Omega$  for the normal case (MFC-NN) to 5.6 k $\Omega$  for the case of both electrodes modified by graphene with cathodic catalyst (MFC-GGP). This was the proof that the improvement of power density and low internal resistance related to the larger surface area and higher conductivity of graphene or CNT. In addition, the MFC systems with the modified electrodes by graphene showed higher power density and lower internal resistance than those by CNTs for the same electrode conditions. Moreover, the anodic modification by carbon-based materials had higher improvement than the cathodic modification. As the modified electrode of air-cathode MFC can significantly enhance the performance of power generation with tremendous cost saving, MFC has a tremendous potential for more extensive and practical applications in the near future.

#### Conflict of Interests

The authors declare that there is no conflict of interests regarding the publication of this paper.

#### Acknowledgment

The authors gratefully acknowledge discussions with Professor Hwan-You Chang from Department of Medical Science, National Tsing Hua University, and the microbe support.

#### References

- [1] Z. W. Du, H. R. Li, and T. Y. Gu, "A state of the art review on microbial fuel cells: a promising technology for wastewater treatment and bioenergy," *Biotechnology Advances*, vol. 25, no. 5, pp. 464–482, 2007.
- [2] R. A. Bullen, T. C. Arnot, J. B. Lakeman, and F. C. Walsh, "Bio-fuel cells and their development," *Biosensors and Bioelectronics*, vol. 21, no. 11, pp. 2015–2045, 2006.
- [3] B. E. Logan, B. Hamelers, R. Rozendal et al., "Microbial fuel cells: methodology and technology," *Environmental Science and Technology*, vol. 40, no. 17, pp. 5181–5192, 2006.
- [4] D. R. Bond and D. R. Lovley, "Electricity production by *Geobacter sulfurreducens* attached to electrodes," *Applied and Environmental Microbiology*, vol. 69, no. 3, pp. 1548–1555, 2003.
- [5] H. P. Bennetto, J. L. Stirling, K. Tanaka, and C. A. Vega, "Anodic reactions in microbial fuel cells," *Biotechnology and Bioengineering*, vol. 25, no. 2, pp. 559–568, 1983.
- [6] M. H. Osman, A. A. Shah, and F. C. Walsh, "Recent progress and continuing challenges in bio-fuel cells. Part I: enzymatic cells," *Biosensors and Bioelectronics*, vol. 26, no. 7, pp. 3087–3102, 2011.
- [7] M. H. Osman, A. A. Shah, and F. C. Walsh, "Recent progress and continuing challenges in bio-fuel cells. Part II: microbial," *Biosensors and Bioelectronics*, vol. 26, no. 3, pp. 953–963, 2010.

- [8] S. Cheng and B. E. Logan, "Ammonia treatment of carbon cloth anodes to enhance power generation of microbial fuel cells," *Electrochemistry Communications*, vol. 9, no. 3, pp. 492–496, 2007.
- [9] X. Wang, S. Cheng, Y. Feng, M. D. Merrill, T. Saito, and B. E. Logan, "Use of carbon mesh anodes and the effect of different pretreatment methods on power production in microbial fuel cells," *Environmental Science and Technology*, vol. 43, no. 17, pp. 6870–6874, 2009.
- [10] S. Cheng, H. Liu, and B. E. Logan, "Power densities using different cathode catalysts (Pt and CoTMPP) and polymer binders (nafion and PTFE) in single chamber microbial fuel cells," *Environmental Science and Technology*, vol. 40, no. 1, pp. 364–369, 2006.
- [11] B. Logan, S. Cheng, V. Watson, and G. Estadt, "Graphite fiber brush anodes for increased power production in air-cathode microbial fuel cells," *Environmental Science and Technology*, vol. 41, no. 9, pp. 3341–3346, 2007.
- [12] H.-Y. Tsai, C.-C. Wu, C.-Y. Lee, and E. P. Shih, "Microbial fuel cell performance of multiwall carbon nanotubes on carbon cloth as electrodes," *Journal of Power Sources*, vol. 194, no. 1, pp. 199–205, 2009.
- [13] S. Cheng, H. Liu, and B. E. Logan, "Increased performance of single-chamber microbial fuel cells using an improved cathode structure," *Electrochemistry Communications*, vol. 8, no. 3, pp. 489–494, 2006.
- [14] H. Liu, S. Cheng, and B. E. Logan, "Power generation in fed-batch microbial fuel cells as a function of ionic strength, temperature, and reactor configuration," *Environmental Science and Technology*, vol. 39, no. 14, pp. 5488–5493, 2005.
- [15] D. H. Park and J. G. Zeikus, "Improved fuel cell and electrode designs for producing electricity from microbial degradation," *Biotechnology and Bioengineering*, vol. 81, no. 3, pp. 348–355, 2003.
- [16] H. Liu, R. Ramnarayanan, and B. E. Logan, "Production of electricity during wastewater treatment using a single chamber microbial fuel cell," *Environmental Science and Technology*, vol. 38, no. 7, pp. 2281–2285, 2004.
- [17] H. Liu and B. E. Logan, "Electricity generation using an air-cathode single chamber microbial fuel cell in the presence and absence of a proton exchange membrane," *Environmental Science and Technology*, vol. 38, no. 14, pp. 4040–4046, 2004.
- [18] B. Cercado-Quezada, M.-L. Delia, and A. Bergel, "Treatment of dairy wastes with a microbial anode formed from garden compost," *Journal of Applied Electrochemistry*, vol. 40, no. 2, pp. 225–232, 2010.
- [19] J. Menicucci, H. Beyenal, E. Marsili, R. A. Veluchamy, G. Demir, and Z. Lewandowski, "Procedure for determining maximum sustainable power generated by microbial fuel cells," *Environmental Science and Technology*, vol. 40, no. 3, pp. 1062–1068, 2006.
- [20] B. E. Logan, C. Murano, K. Scott, N. D. Gray, and I. M. Head, "Electricity generation from cysteine in a microbial fuel cell," *Water Research*, vol. 39, no. 5, pp. 942–952, 2005.
- [21] S. Cheng, H. Liu, and B. E. Logan, "Increased power generation in a continuous flow MFC with advective flow through the porous anode and reduced electrode spacing," *Environmental Science and Technology*, vol. 40, no. 7, pp. 2426–2432, 2006.
- [22] T. Sharma, A. L. M. Reddy, T. S. Chandra, and S. Ramaprabhu, "Development of carbon nanotubes and nanofluids based microbial fuel cell," *International Journal of Hydrogen Energy*, vol. 33, no. 22, pp. 6749–6754, 2008.
- [23] C.-T. Wang, Y.-M. Chen, Z.-Q. Qi, and Y.-C. Yang, "Carbon nanotube planted on Ni-based alloy in microbial fuel cell," *Journal of Nanomaterials*, vol. 2013, Article ID 435960, 5 pages, 2013.
- [24] C. Lee, X. Wei, J. W. Kysar, and J. Hone, "Measurement of the elastic properties and intrinsic strength of monolayer graphene," *Science*, vol. 321, no. 5887, pp. 385–388, 2008.
- [25] H. Choi, H. Kim, S. Hwang, W. Choi, and M. Jeon, "Dye-sensitized solar cells using graphene-based carbon nano composite as counter electrode," *Solar Energy Materials and Solar Cells*, vol. 95, no. 1, pp. 296–300, 2011.
- [26] C.-H. Hsu, C.-C. Lai, L.-C. Chen, and P.-S. Chan, "Enhanced performance of dye-sensitized solar cells with graphene/ZnO nanoparticles bilayer structure," *Journal of Nanomaterials*, vol. 2014, Article ID 748319, 6 pages, 2014.
- [27] J. R. Miller, R. A. Outlaw, and B. C. Holloway, "Graphene electric double layer capacitor with ultra-high-power performance," *Electrochimica Acta*, vol. 56, no. 28, pp. 10443–10449, 2011.
- [28] A. J. Bard and L. R. Faulkner, *Electrochemical Methods: Fundamentals and Applications*, John Wiley & Sons, Hoboken, NJ, USA, 2nd edition, 2001.
- [29] N. Zhu, X. Chen, T. Zhang, P. Wu, P. Li, and J. Wu, "Improved performance of membrane free single-chamber air-cathode microbial fuel cells with nitric acid and ethylenediamine surface modified activated carbon fiber felt anodes," *Bioresource Technology*, vol. 102, no. 1, pp. 422–426, 2011.

## Research Article

# Effects of Niobium-Loading on Sulfur Dioxide Gas-Sensing Characteristics of Hydrothermally Prepared Tungsten Oxide Thick Film

Viruntachar Kruefu,<sup>1</sup> Anurat Wisitsoraat,<sup>2</sup> and Sukon Phanichphant<sup>3</sup>

<sup>1</sup>Program in Materials Science, Faculty of Science, Maejo University, Chiang Mai 50290, Thailand

<sup>2</sup>National Electronics and Computer Technology Center, National Science and Technology Development Agency, Pathum Thani 12120, Thailand

<sup>3</sup>Materials Science Research Center, Faculty of Science, Chiang Mai University, Chiang Mai 50200, Thailand

Correspondence should be addressed to Viruntachar Kruefu; [v\\_viruntachar@hotmail.com](mailto:v_viruntachar@hotmail.com)

Received 7 August 2014; Revised 4 November 2014; Accepted 11 November 2014

Academic Editor: Rupesh S. Devan

Copyright © 2015 Viruntachar Kruefu et al. This is an open access article distributed under the Creative Commons Attribution License, which permits unrestricted use, distribution, and reproduction in any medium, provided the original work is properly cited.

Nb-loaded hexagonal WO<sub>3</sub> nanorods with 0–1.0 wt% loading levels were successfully synthesized by a simple hydrothermal and impregnation process and characterized for SO<sub>2</sub> sensing. Nb-loaded WO<sub>3</sub> sensing films were produced by spin coating on alumina substrate with interdigitated gold electrodes and annealed at 450°C for 3 h in air. Structural characterization by X-ray diffraction, high-resolution transmission electron microscopy, and Brunauer-Emmett-Teller analysis showed that spherical, oval, and rod-like Nb nanoparticles with 5–15 nm mean diameter were uniformly dispersed on hexagonal WO<sub>3</sub> nanorods with 50–250 nm diameter and 100 nm–5 μm length. It was found that the optimal Nb loading level of 0.5 wt% provides substantial enhancement of SO<sub>2</sub> response but the response became deteriorated at lower and higher loading levels. The 0.50 wt% Nb-loaded WO<sub>3</sub> nanorod sensing film exhibits the best SO<sub>2</sub> sensing performances with a high sensor response of ~10 and a short response time of ~6 seconds to 500 ppm of SO<sub>2</sub> at a relatively low optimal operating temperature of 250°C. Therefore, Nb loading is an effective mean to improve the SO<sub>2</sub> gas-sensing performances of hydrothermally prepared WO<sub>3</sub> nanorods.

## 1. Introduction

Sulfur dioxide (SO<sub>2</sub>) is a colorless toxic gas with burning smell that causes various respiratory and cardiovascular diseases as well as environmentally hazardous acid rain [1]. There has been increasing demand for on-site monitoring of SO<sub>2</sub> due to rising level of SO<sub>2</sub> pollutant produced by various industrial processes. Presently, the concentration of SO<sub>2</sub> is still primarily determined by conventional techniques including gas chromatography or electrochemical detections, which are expensive, cumbersome, and impractical for on-site applications. Metal oxide semiconductor gas sensors are potential candidates for portable gas-sensing devices due to high sensitivity, good stability, low cost, small size, and simple electronic interface [1–10]. However, only few metal oxide materials including WO<sub>3</sub>, SnO, and ZnO give significant

response to SO<sub>2</sub> and the reported response values are still limited [1]. Among these, WO<sub>3</sub> exhibits relatively stable and good response to SO<sub>2</sub> [1, 9–13]. The gas-sensing properties towards SO<sub>2</sub> of WO<sub>3</sub>-based gas sensors prepared by various methods are summarized in Table 1.

Firstly, WO<sub>3</sub> thick film fabricated by pyrolysis/paste casting gave an optimal response of ~12 to 800 ppm SO<sub>2</sub> at 400°C [9]. In addition, WO<sub>3</sub> sensor produced by drop casting exhibited a response of ~1.3 to 25 ppm SO<sub>2</sub> at a lower optimal working temperature of 200°C [10]. Similarly, WO<sub>3</sub> thick film sensor deposited by electrostatic spray method displayed a response of ~3 to 20 ppm SO<sub>2</sub> at 350°C [12]. Moreover, WO<sub>3</sub> sensors made by hydrothermal and screen-printing processes showed a fair response of <2 to low SO<sub>2</sub> concentrations of 1–10 ppm at 260°C [13]. It can be seen that undoped WO<sub>3</sub> sensors tend to suffer from limited SO<sub>2</sub> response or

TABLE I: A summary of the gas-sensing properties of WO<sub>3</sub>-based gas sensors towards SO<sub>2</sub>.

Authors/reference	Method	Materials	Gas concentration	SO <sub>2</sub> sensing performances
Shimizu et al., 2001 [9]	Pyrolysis/paste casting	Unloaded WO <sub>3</sub>	800 ppm	Response: ~12 to 800 ppm at 400°C
	Pyrolysis/impregnation/paste casting	1.0 wt% Ag/WO <sub>3</sub>	800 ppm	Response: ~20 to 800 ppm at 450°C
Tomchenko et al., 2003 [10]	Drop casting	WO <sub>3</sub>	25 ppm	Response: ~1.3 to 25 ppm at 200°C
Stankova et al., 2004 [11]	RF magnetron sputtering	Pt/WO <sub>3</sub>	1 ppm	Response: ~6 to 1 ppm at 200°C, 50 μm of electrode gap
Matei Ghimbeu et al., 2010 [12]	Electrostatic spray deposition	Unloaded WO <sub>3</sub>	20 ppm	Response: ~3 to 20 ppm at 350°C
Boudiba et al., 2012 [13]	Hydrothermal/screen-printing	WO <sub>3</sub> thick films	1–10 ppm	Response: <2 to 10 ppm at 260°C
This work	Hydrothermal/spin coating	0.5 wt% Nb-WO <sub>3</sub>	25–500 ppm	Response: ~10 to 500 ppm at 250°C

high optimal working temperature. Thus, incorporations of various metallic additives including Au, Ag, Cu, Pt, Pd, and Rh have been studied to improve the SO<sub>2</sub> gas-sensing properties of WO<sub>3</sub> sensors [9, 11]. For instance, the addition of 1.00 wt% Ag to pyrolyzed WO<sub>3</sub> thick film sensors led to the highest response of ~20 to 800 ppm SO<sub>2</sub> at 450°C [9]. In another study, Pt-loaded rf-sputtered WO<sub>3</sub> thin film showed a good response of ~6 to 1 ppm SO<sub>2</sub> diluted in CO<sub>2</sub> at 200°C with the absence of oxygen while the response to H<sub>2</sub>S was very low (<1), dictating good SO<sub>2</sub> selectivity [11]. Thus, studies of additive incorporation in WO<sub>3</sub> for SO<sub>2</sub> sensing are still limited and more effective metal additives should be explored to achieve better SO<sub>2</sub> gas-sensing performances.

Niobium is a noble metal catalyst that is found to be useful for gas sensing towards particular gases such as NO<sub>2</sub> and CO [14, 15]. However, there is no report of its addition to WO<sub>3</sub> support for SO<sub>2</sub> gas sensing. In this work, Nb nanoparticles are impregnated on WO<sub>3</sub> nanorods synthesized by hydrothermal synthesis and the effect of Nb loading concentration on SO<sub>2</sub> gas-sensing performances is studied as a function of the operating temperature and gas concentration.

## 2. Experimental Methods

**2.1. Synthesis of Material.** Unloaded and Nb-loaded WO<sub>3</sub> nanorods were synthesized by hydrothermal and impregnation methods using sodium tungstate dihydrate (Na<sub>2</sub>WO<sub>4</sub>·2H<sub>2</sub>O) and sodium chloride (NaCl) as initial precursors and niobium (V) ethoxide (Nb(OCH<sub>2</sub>CH<sub>3</sub>)<sub>5</sub>) as Nb-impregnation precursor. To synthesize unloaded WO<sub>3</sub> nanorods, 2.215 g of Na<sub>2</sub>WO<sub>4</sub>·H<sub>2</sub>O and 0.7747 g of NaCl were dissolved in 100 mL of deionized (DI) water under constant stirring. Subsequently, 3 M HCl was slowly dropped into the solution until the pH value of 2 was reached. The solution was then transferred into a Teflon-lined autoclave and the hydrothermal reaction was carried out in an oven at 100°C for

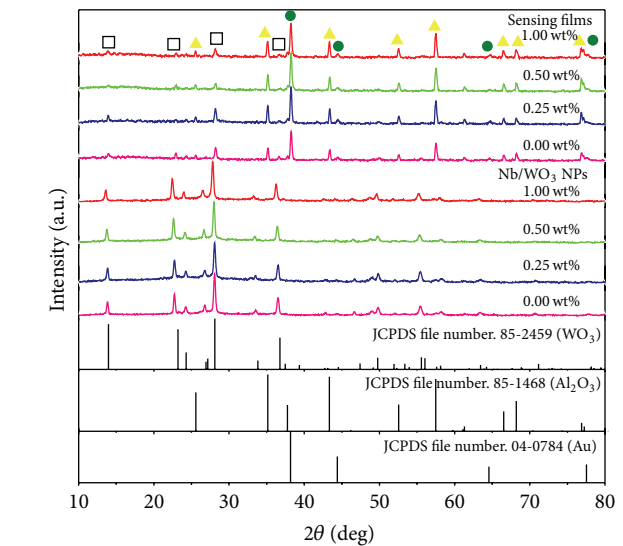


FIGURE 1: XRD diffraction patterns of unloaded and 0.25–1.00 wt% Nb-loaded WO<sub>3</sub> sensing films and powders. JCPDS files number 85-2549, 04-0784, and 82-1468 refer to (□) WO<sub>3</sub>, (●) Au, and (△) Al<sub>2</sub>O<sub>3</sub>, respectively.

6 h. After cooling the autoclave down to room temperature, the final products were washed with DI water and ethanol several times with centrifugation. The obtained powder was subsequently dried at 60°C for 24 h in air. To impregnate Nb nanoparticles onto WO<sub>3</sub> nanorods, 0.0398 g of niobium (V) ethoxide was dissolved in 6 mL of methanol solution under vigorous stirring. The solution was then added to 1 g of WO<sub>3</sub> nanorods with Nb concentrations of 0.25, 0.50, and 1.00 wt%, respectively. The mixture was stirred until they formed smooth slurry and dried in an oven at 80°C for 2 h. Finally, the final powders were calcined at 300°C for 2 h.

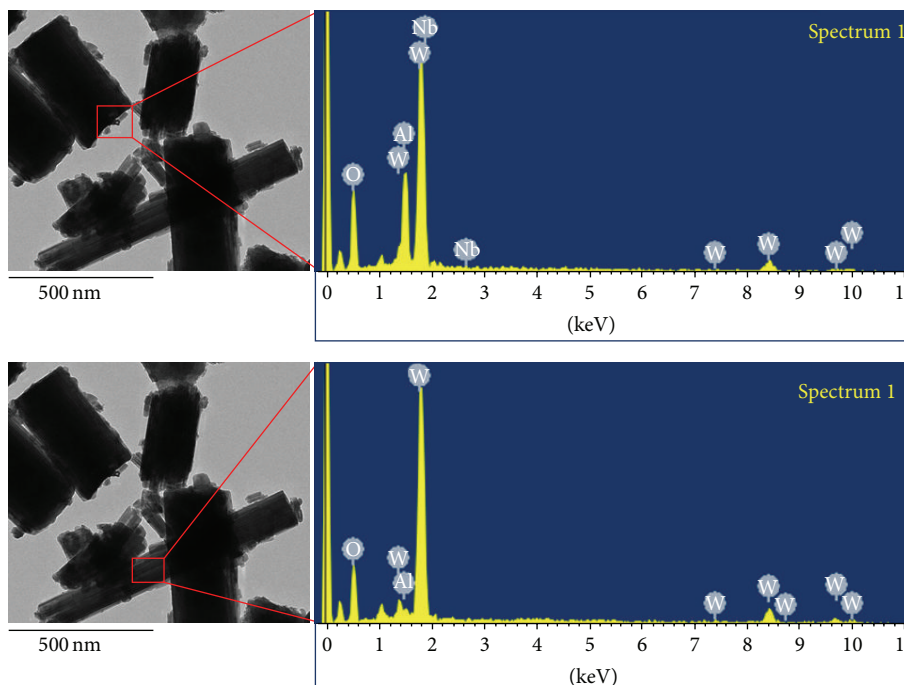


FIGURE 2: HRTEM bright-field images and EDX spectra of 0.5 wt% Nb-loaded  $\text{WO}_3$  nanorods.

**2.2. Material Characterization.** The phase structure of unloaded  $\text{WO}_3$  and Nb-loaded  $\text{WO}_3$  nanorods was studied by means of X-ray diffraction (XRD; TTRAX III diffractometer, Rigaku). The morphology of nanorods was examined by high-resolution transmission electron microscopy (HRTEM; JEM-2010, JEOL). The presence of Nb element was confirmed by an energy dispersive X-ray spectroscopy (EDX). The specific surface areas ( $\text{SSA}_{\text{BET}}$ ) and pore sizes of nanorods were determined from Brunauer-Emmett-Teller (BET) and Barrett-Joyner-Halenda (BJH) analyses of nitrogen adsorption measurements.

**2.3. Sensing Film Fabrication and Characterization.** To form paste for spin coating of sensing films, 60 mg of unloaded  $\text{WO}_3$  or 0.25–1.00 wt% Nb-loaded  $\text{WO}_3$  nanopowder was thoroughly mixed with an organic paste composed of ethyl cellulose and terpineol (0.25 mL), which acted as a vehicle binder and solvent, respectively. The resulting paste was spin-coated on alumina substrates equipped with interdigitated gold electrodes and then annealed at 450°C for 2 h with a heating rate of 2°C/min for binder removal. After annealing and sensing test at 350°C in dry air, the morphologies, cross section, and elemental compositions of sensing films were analyzed by glancing-incident XRD (GIXRD; TTRAX III diffractometer, Rigaku), scanning electron microscopy (SEM; JEOL JSM-6335F), and EDX spectroscopy.

**2.4. Gas-Sensing Measurement.** For gas-sensing measurements, unloaded and Nb-loaded  $\text{WO}_3$  sensors were heated by the external NiCr heater to the operating temperatures ranging from 200 to 350°C in dry air before exposure to target gases in a stainless steel chamber (the setup is reported in

our previous work [14]). The target gas source (1000 ppm  $\text{SO}_2$  balanced in dry air) was flowed to mix with dry air at different flow rates to attain desired concentrations using multichannel mass flow controllers (Brook Instrument). The resistances of various sensors were continuously monitored with a computer-controlled system by voltage-amperometric technique with 10 V dc bias and current measurement through a 6487 Keithley picoammeter. The gas-sensing properties of unloaded and Nb-loaded  $\text{WO}_3$  sensors are characterized in terms of response and response time as a function of gas concentration and operating temperature. The gas-sensing response ( $S$ ) is given by  $S = R_a/R_g$ , where  $R_a$  and  $R_g$  are the electrical resistances of the sensor measured in the presence of pure dry air and reducing gas, respectively. The response time ( $T_{\text{res}}$ ) is the time required to reach 90% of the response signal while the recovery time ( $T_{\text{rec}}$ ) is the time needed to recover 90% of the baseline signal.

### 3. Results and Discussion

**3.1. Particle and Sensing Film Characterization.** The crystal structures of unloaded and 0.25–1.00 wt% Nb-loaded  $\text{WO}_3$  nanorods and sensing films after annealing and sensing test were studied by XRD using  $\text{CuK}_\alpha$  radiation at  $2\theta = 10\text{--}80^\circ$  with a step size of  $0.06^\circ$  and a scanning speed of  $0.72^\circ/\text{min}$  as presented in Figure 1. It is seen that unloaded and Nb-loaded  $\text{WO}_3$  nanorods prepared by hydrothermal and impregnation methods exhibit sharp XRD peaks whose locations are well matched to JCPDS 85-2459 [13], indicating polycrystalline structure of hexagonal  $\text{WO}_3$  phase with high crystallinity. In addition, Nb diffraction peaks cannot be observed in all samples since the amount and size of Nb nanoparticles

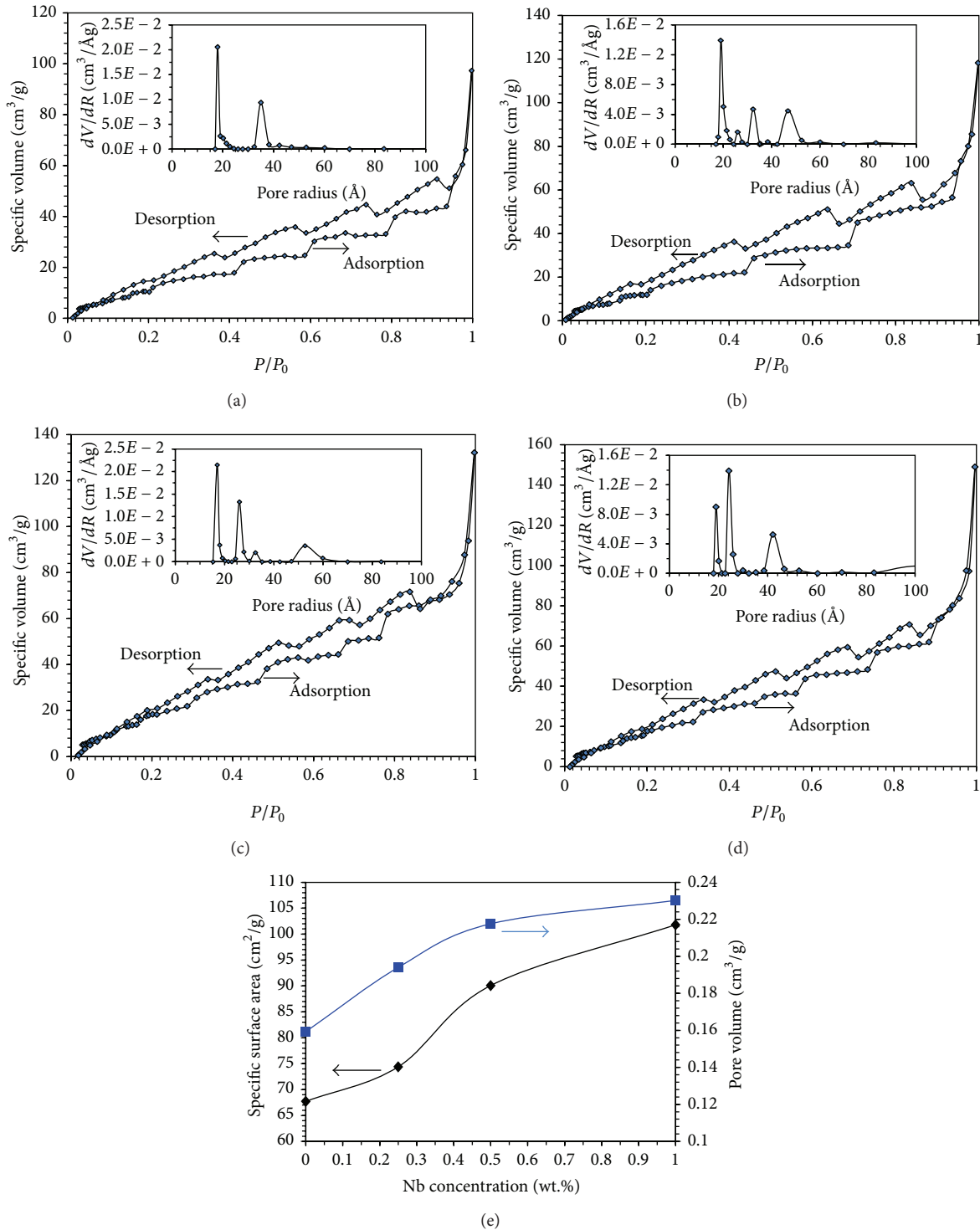


FIGURE 3: Nitrogen adsorption isotherm and BJH pore size distribution (inset) of (a) unloaded  $\text{WO}_3$  nanorods, (b) 0.25 wt% Nb-loaded  $\text{WO}_3$  nanorods, (c) 0.5 wt% Nb-loaded  $\text{WO}_3$  nanorods, (d) 1.0 wt% Nb-loaded  $\text{WO}_3$  nanorods, and (e) pore volume and specific surface area ( $\text{SSA}_{\text{BET}}$ ) of unloaded and 0.25–1.0 wt% Nb-loaded  $\text{WO}_3$  nanorods.

are below the detection limit of XRD instrument. Thus, the presence of Nb nanoparticles in the composite will be confirmed by HRTEM and EDS analysis. For sensing films coated on  $\text{Au}/\text{Al}_2\text{O}_3$  substrates, the XRD patterns affirm

the presence of hexagonal  $\text{WO}_3$  phase whose diffraction peaks are weaker than those of (●) Au (JCPDS file number 04-0784 [16]) and (△)  $\text{Al}_2\text{O}_3$  (JCPDS file number 82-1468 [17]) from the substrate.

HRTEM bright-field images and EDX spectra of 0.50 wt% Nb-loaded  $\text{WO}_3$  nanorods synthesized by hydrothermal/impregnation are shown in Figure 2. The images show longitudinal sides of solid nanorods displaying rectangular shapes with length varying from 100 nm to  $5\ \mu\text{m}$  and width (the diameter of nanorod) ranging from 50 to 250 nm. In addition, the bigger nanorod surfaces are uniformly decorated with smaller spherical, oval, and rod-like nanoparticles. The mean diameter of particles is estimated to be in the range of 5–15 nm for 0.50 wt% Nb-loaded  $\text{WO}_3$  nanorods. The EDX spectra at the two regions (Figure 2) confirm that the nanorods and nanoparticles are made of  $\text{WO}_3$  and Nb, respectively.

The nitrogen adsorption isotherm and BJH adsorption pore size distribution (inset) of  $\text{WO}_3$  nanorods with 0–1 wt% Nb loading levels are shown in Figures 3(a)–3(d), respectively. It can be seen that all the isotherms exhibit the IUPAC type VI pattern, indicating the existence of stepwise multilayer adsorption on nonuniform surface of nonporous adsorbent or micropores filled with multilayer adsorbates [18, 19]. In addition, adsorbed volume tends to increase with increasing Nb loading level. The pore size distributions are in multimodal forms with 2–4 maxima depending on Nb loading. The distributions of unloaded  $\text{WO}_3$  nanorods display two maxima at  $\sim 19$  and  $\sim 36$  Å while those of Nb-loaded ones exhibit three significant maxima at 18–20, 26–36, and  $\sim 44$ –52 Å, respectively. The results indicate the surfaces are porous and contain micropores as well as mesopores structures. In addition, the contribution of larger pores tends to increase with increasing Nb loading levels. The minor maxima and minima are expected to be artifacts induced by the modeling technique. Figure 3(e) displays the corresponding pore volume and BET specific surface areas ( $\text{SSA}_{\text{BET}}$ ) of  $\text{WO}_3$  nanorods. As the Nb concentration increases from 0 to 1.00 wt%, pore volume and  $\text{SSA}_{\text{BET}}$  monotonically increase from 0.16 to  $0.23\ \text{cm}^3/\text{g}$  and from 67.72 to  $101.8\ \text{m}^2/\text{g}$ , respectively. The increased pore volume and specific surface area may be attributed to wider pore distribution due to interaction between Nb nanoparticles and  $\text{WO}_3$  nanorods as well as increasing contribution of smaller Nb nanoparticles with increasing Nb loading level.

The typical cross-sectional SEM micrograph of 0.50 wt% Nb-loaded  $\text{WO}_3$  film layer on an  $\text{Al}_2\text{O}_3$  substrate equipped with interdigitated Au electrodes after the sensing test is shown in Figure 4. It is seen that the sensing film with an average thickness of  $\sim 10\ \mu\text{m}$  contains loosely agglomerated nanorods. The detailed top surface morphology of nanorods is also shown in the inset. It shows that nanorods up to several microns long are slackedly entangled with each other leaving many large and small pores in the film. The observed morphology indicates that the final sensing film has a large specific surface area, which should be highly beneficial for gas-sensing applications.

**3.2. Gas-Sensing Properties.** The changes of resistance of  $\text{WO}_3$  nanorods with different Nb loading concentrations exposed to  $\text{SO}_2$  pulses at various concentrations (500–20 ppm) are shown in Figure 5. It is evident that the resistance of all  $\text{WO}_3$  sensors rapidly increases upon exposure to

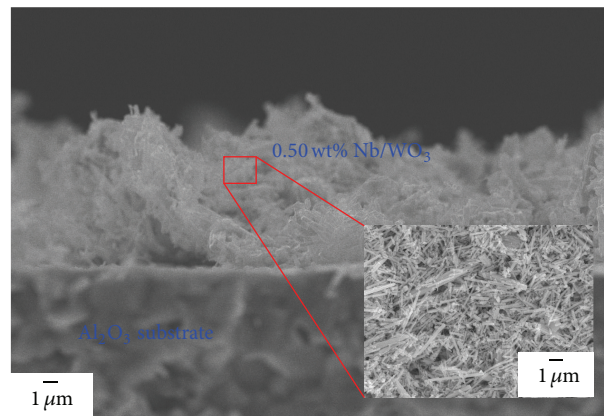


FIGURE 4: Cross-sectional SEM image of 0.5 wt% Nb-loaded  $\text{WO}_3$  film on Au/ $\text{Al}_2\text{O}_3$  substrate. Inset top-view surface morphology.

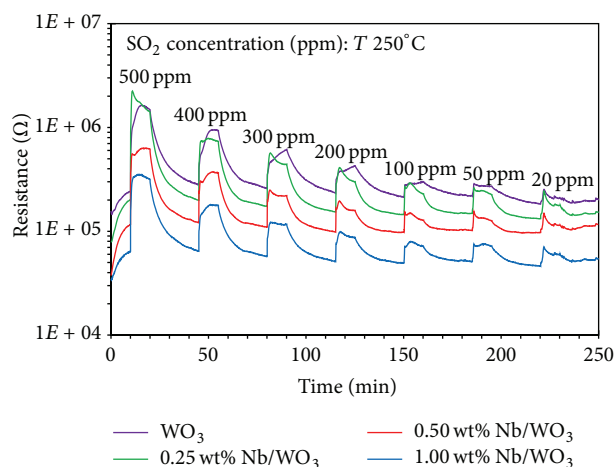
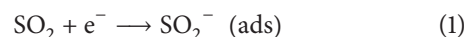


FIGURE 5: Change in resistance of unloaded and 0.25–1.0 wt% Nb-loaded  $\text{WO}_3$  gas sensors to  $\text{SO}_2$  pulses with concentration ranging from 20 to 500 ppm at  $250^\circ\text{C}$ .

$\text{SO}_2$ , indicating n-type semiconducting behavior towards oxidizing gas. The result is in agreement with previous reports on  $\text{SO}_2$  gas-sensing studies of  $\text{WO}_3$  sensors [9, 10]. When the  $\text{WO}_3$  nanorods are exposed to  $\text{SO}_2$  gas,  $\text{SO}_2$  gas will adsorb on  $\text{WO}_3$  surface at different sites from the existing chemisorbed  $\text{O}_2^-$ ,  $\text{O}^-$ , and  $\text{O}^{2-}$  ions and extract additional electrons from conduction band of  $\text{WO}_3$  to become  $\text{SO}_2^-$  according to (1) [10]. As a result, the concentration of electrons on the surface of  $\text{WO}_3$  nanorods decreases and the resistance of  $\text{WO}_3$  layer increases. Consider



Figures 6(a) and 6(b) show the response and response time of  $\text{WO}_3$  nanorods with different Nb loading levels versus  $\text{SO}_2$  concentration in the range of 20–500 ppm at the operating temperature of  $250^\circ\text{C}$ . It can be seen that the gas-sensing behaviors of  $\text{WO}_3$  nanorods considerably depend on Nb loading level. As the Nb loading level increases from 0 to 0.25 wt%, the  $\text{SO}_2$  response slightly decreases but then

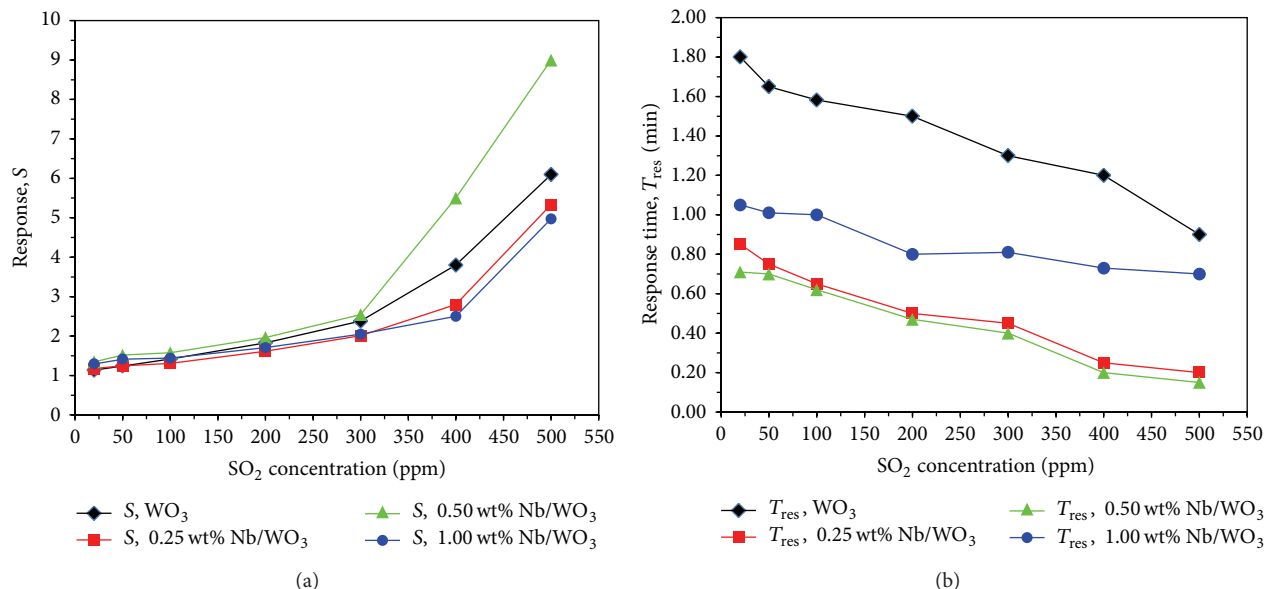


FIGURE 6: Variation of (a) response and (b) response times of unloaded and 0.25–1.0 wt% Nb-loaded WO<sub>3</sub> sensors versus SO<sub>2</sub> concentration at 250°C.

becomes significantly higher as the loading concentration increases further to 0.5 wt%. Conversely, the response time monotonically reduces as the Nb loading concentration increases from 0 to 0.5 wt%. The sensing film with 0.50 wt% Nb-loaded WO<sub>3</sub> nanorods exhibits the best SO<sub>2</sub> sensing performances with a high sensor response of ~10 and a short response time of ~6 seconds to 500 ppm of SO<sub>2</sub> at 250°C. Thus, the moderate Nb loading level of 0.5 wt% could substantially improve the response towards SO<sub>2</sub>. However, the response and response time are considerably degraded when the Nb loading concentration further increases to 1.0 wt%. Regarding the baseline recovery, unloaded and Nb-loaded WO<sub>3</sub> nanorods have similarly long recovery times on the order of several minutes, which are not practical for gas-sensing applications. The recovery time is dictated by the sensor's inherent oxygen re-adsorption rate as well as gas flow dynamic. In this case, the slow gas flow dynamic due to large volume of gas-testing chamber (~3 liters) was found to be the main cause of slow recovery and the problem may be solved by miniaturization of sensors and test system.

From the results, the optimum Nb loading concentration of WO<sub>3</sub> nanorods for SO<sub>2</sub> sensing is 0.5 wt%. A possible explanation for the enhanced SO<sub>2</sub> response due to moderate Nb doping is that Nb nanoparticles may provide catalytic effect to enhance SO<sub>2</sub><sup>-</sup> adsorption on WO<sub>3</sub> surface and this mechanism will be effective when there is a sufficient amount of Nb nanoparticles well dispersed on WO<sub>3</sub> nanorods so that electron transfer due to SO<sub>2</sub> adsorption can dominate the resistance control at most contacts. Moreover, Nb loading results in increased pore volume and specific surface area for gas adsorption. When the Nb loading level (i.e., 0.25 wt%) is too low, the enhancement effect is very low and the observed small response decrease may be due to the slight reduction in porosity and thickness of the final sensing film. At too high Nb loading concentration, Nb nanoparticles may become

agglomerated into larger particles so that the catalytic mechanism is less effective, leading to deteriorated SO<sub>2</sub> response. In addition, the proposed catalytic effect may be supported by the observed significant decrease of response time with Nb loading since this effect should result in higher adsorption rate and more rapid change in resistance upon SO<sub>2</sub> exposure.

Figure 7 shows the effect of operating temperature on response to 500 ppm SO<sub>2</sub> of WO<sub>3</sub> nanorods with different Nb loading concentrations. It is clear that all sensors exhibit similar temperature dependence of response with optimal operating temperature of 250°C and much lower response at lower (200°C) and higher (300–350°C) temperatures. At low temperature, SO<sub>2</sub><sup>-</sup> adsorption rate and SO<sub>2</sub> response are low due to low thermal energy. In the case of high temperature, the SO<sub>2</sub><sup>-</sup> adsorption rate and response become low despite the increase of thermal energy because there is less available site for SO<sub>2</sub><sup>-</sup> adsorption due to the increased concentration of preadsorbed oxygen species. The attained optimal SO<sub>2</sub> response (~10 to 500 ppm SO<sub>2</sub>) and operating temperature (250°C) are relatively advantageous compared with some previously reported WO<sub>3</sub> sensors as listed in Table 1 that showed lower response at similar operating temperature or exhibited higher response at low concentration but required higher optimal operating temperature of 350–450°C [8–12]. However, the performances of Nb-loaded WO<sub>3</sub> sensor are inferior to those of Pt/WO<sub>3</sub> sensor that can achieve both high response and low operating temperature but the sensor requires much more expensive Pt catalyst [11]. Therefore, Nb-loaded WO<sub>3</sub> nanorods are a promising alternative for SO<sub>2</sub> sensing.

#### 4. Conclusions

Unloaded and 0.25–1.0 wt% Nb-loaded WO<sub>3</sub> nanorods were successfully synthesized by hydrothermal and impregnation

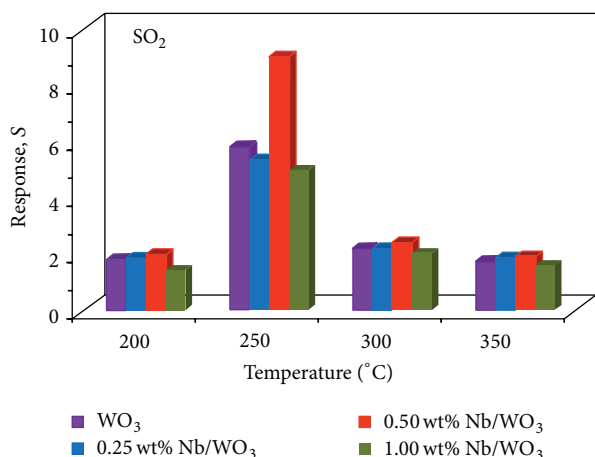


FIGURE 7: The response of 0.50 wt% Nb-loaded WO<sub>3</sub>-based gas sensor towards 500 ppm SO<sub>2</sub> versus operating temperature.

methods. From structural characterizations, spherical, oval, and rod-like Nb nanoparticles with 5–15 nm mean diameter were uniformly dispersed on hexagonal WO<sub>3</sub> nanorods with 50–250 nm diameter and 100 nm–5 μm length. From gas-sensing measurement, Nb loading with the moderate level of 0.5 wt% led to substantial enhancement of SO<sub>2</sub> response but the response became deteriorated at lower and higher loading levels. The 0.50 wt% Nb-loaded WO<sub>3</sub> nanorod sensing film exhibited the best SO<sub>2</sub> sensing performances with a high sensor response of ~10 and a short response time of ~6 seconds to 500 ppm of SO<sub>2</sub> at a relatively low optimal operating temperature of 250°C. The enhanced SO<sub>2</sub> sensing performances may be attributed to catalytic effect of well dispersed Nb nanoparticles on WO<sub>3</sub> nanorods. Therefore, Nb loading is an effective method to enhance the SO<sub>2</sub> gas-sensing performances of hydrothermally prepared WO<sub>3</sub> nanorods.

## Conflict of Interests

The authors declare that there is no conflict of interests regarding the publication of this paper.

## Acknowledgments

The authors gratefully acknowledge the financial support from the National Research Council of Thailand (NRCT); Program in Materials Science, Faculty of Science, Maejo University, Thailand; the National Research University Project under Thailand's Office of the Higher Education Commission; the Graduate School and Department of Chemistry, Faculty of Science, Chiang Mai University, Thailand, and National Electronics and Computer Technology Center, Pathumthani, Thailand, are gratefully acknowledged.

## References

- [1] K. Wetchakun, T. Samerjai, N. Tamaekong et al., "Semiconducting metal oxides as sensors for environmentally hazardous

gases," *Sensors and Actuators B: Chemical*, vol. 160, no. 1, pp. 580–591, 2011.

- [2] R. S. Devan, R. A. Patil, J.-H. Lin, and Y.-R. Ma, "One-dimensional metal-oxide nanostructures: recent developments in synthesis, characterization, and applications," *Advanced Functional Materials*, vol. 22, no. 16, pp. 3326–3370, 2012.
- [3] H. Zhang, S. Wang, Y. Wang, J. Yang, X. Gao, and L. Wang, "TiO<sub>2</sub>(B) nanoparticle-functionalized WO<sub>3</sub> nanorods with enhanced gas sensing properties," *Physical Chemistry Chemical Physics*, vol. 16, no. 22, pp. 10830–10836, 2014.
- [4] W. Zeng, C. Dong, B. Miao et al., "Preparation, characterization and gas sensing properties of sub-micron porous WO<sub>3</sub> spheres," *Materials Letters*, vol. 117, pp. 41–44, 2014.
- [5] J. S. Lee, O. S. Kwon, D. H. Shin, and J. Jang, "WO<sub>3</sub> nanonodule-decorated hybrid carbon nanofibers for NO<sub>2</sub> gas sensor application," *Journal of Materials Chemistry A*, vol. 1, no. 32, pp. 9099–9106, 2013.
- [6] S. Bai, K. Zhang, R. Luo, D. Li, A. Chen, and C. C. Liu, "Low-temperature hydrothermal synthesis of WO<sub>3</sub> nanorods and their sensing properties for NO<sub>2</sub>," *Journal of Materials Chemistry*, vol. 22, no. 25, pp. 12643–12650, 2012.
- [7] F. Chávez, G. F. Pérez-Sánchez, O. Goiz et al., "Sensing performance of palladium-functionalized WO<sub>3</sub> nanowires by a drop-casting method," *Applied Surface Science*, vol. 275, pp. 28–35, 2013.
- [8] X. Su, Y. Li, J. Jian, and J. Wang, "In situ etching WO<sub>3</sub> nanoplates: hydrothermal synthesis, photoluminescence and gas sensor properties," *Materials Research Bulletin*, vol. 45, no. 12, pp. 1960–1963, 2010.
- [9] Y. Shimizu, N. Matsunaga, T. Hyodo, and M. Egashira, "Improvement of SO<sub>2</sub> sensing properties of WO<sub>3</sub> by noble metal loading," *Sensors and Actuators, B: Chemical*, vol. 77, no. 1-2, pp. 35–40, 2001.
- [10] A. A. Tomchenko, G. P. Harmer, B. T. Marquis, and J. W. Allen, "Semiconducting metal oxide sensor array for the selective detection of combustion gases," *Sensors and Actuators, B: Chemical*, vol. 93, no. 1-3, pp. 126–134, 2003.
- [11] M. Stankova, X. Vilanova, J. Calderer et al., "Detection of SO<sub>2</sub> and H<sub>2</sub>S in CO<sub>2</sub> stream by means of WO<sub>3</sub>-based micro-hotplate sensors," *Sensors and Actuators B: Chemical*, vol. 102, no. 2, pp. 219–225, 2004.
- [12] C. Matei Ghimbeu, M. Lumbreras, M. Siadat, and J. Schoonman, "Detection of H<sub>2</sub>S, SO<sub>2</sub>, and NO<sub>2</sub> using electrostatic sprayed tungsten oxide films," *Materials Science in Semiconductor Processing*, vol. 13, no. 1, pp. 1–8, 2010.
- [13] A. Boudiba, C. Zhang, C. Bittencourt et al., "SO<sub>2</sub> gas sensors based on WO<sub>3</sub> nanostructures with different morphologies," *Procedia Engineering*, vol. 47, pp. 1033–1036, 2012.
- [14] V. Kruefu, C. Liewhiran, A. Wisitsoraat, and S. Phanichphant, "Selectivity of flame-spray-made Nb/ZnO thick films towards NO<sub>2</sub> gas," *Sensors and Actuators, B: Chemical*, vol. 156, no. 1, pp. 360–367, 2011.
- [15] A. Teleki, N. Bjelobrk, and S. E. Pratsinis, "Flame-made Nb- and Cu-doped TiO<sub>2</sub> sensors for CO and ethanol," *Sensors and Actuators, B: Chemical*, vol. 130, no. 1, pp. 449–457, 2008.
- [16] W. Wong-Ng, H. F. McMurdie, C. R. Hubbard, and A. D. Mighell, "JCPDS-ICDD research associate ship (Cooperative program with NBS/NIST)," *Journal of Research of the National Institute of Standards and Technology*, vol. 106, no. 6, pp. 1013–1028, 2001.

- [17] H. Sawada, "Residual electron density study of  $\alpha$ -aluminum oxide through refinement of experimental atomic scattering factors," *Materials Research Bulletin*, vol. 29, no. 2, pp. 127–133, 1994.
- [18] J. H. de Boer, B. C. Lippens, B. G. Linsen, J. C. P. Broekhoff, A. van den Heuvel, and T. J. Osinga, "The t-curve of multimolecular  $N_2$ -adsorption," *Journal of Colloid And Interface Science*, vol. 21, no. 4, pp. 405–414, 1966.
- [19] K. S. W. Sing, D. H. Everett, R. A. W. Haul et al., "Reporting physisorption data for gas/solid systems with special reference to the determination of surface area and porosity (Recommendations 1984)," *Pure and Applied Chemistry*, vol. 57, pp. 603–619, 1985.